On radio-frequency implant safety in parallel transmission MRI

Thesis

for the degree of

doctor rerum naturalium
(Dr. rer. nat.)

approved by the Faculty of Natural Sciences
of Otto von Guericke University Magdeburg

by M.Sc. Johannes Petzold
born on 1995-06-02 in Leipzig, Germany

Examiners: Prof. Dr. rer. nat. habil. Oliver Speck
Prof. Dr. rer. nat. habil. Harald Möller

submitted on: 2023-08-28
defended on: 2024-02-08

Supervisors:

Dr. rer. nat. Frank Seifert	Physikalisch-Technische Bundesanstalt (PTB), Braunschweig and Berlin
Dr. rer. nat. habil. Bernd Ittermann	Physikalisch-Technische Bundesanstalt (PTB), Braunschweig and Berlin
Prof. Dr. rer. nat. habil. Oliver Speck	Otto von Guericke University, Magdeburg

Contents

Kurzfassung

Der steigenden Anzahl an Patienten mit aktiven implantierbaren medizinischen Geräten (AIMD) wird im Allgemeinen der Zugang zur Magnetresonanztomographie (MRT) erschwert. „MR unsafe“ Implantate können beispielsweise nur außerhalb ihrer Zulassung gescannt werden, während bei „MR conditional“ Implantaten Grenzwerte aus mehrstufigen hersteller- und implantatspezifischen Anleitungen verwendet werden müssen. Dies sorgt für die Gefährdung der Patienten und zu schlechterer Bildgebungsleistung durch entsprechend konservativ angesetzte Grenzwerte. Es ist bekannt, dass optimierte parallel gesendete (pTx) Hochfrequenz (HF)-B_1^+-Felder die volle MRT Leistung ausreizen.

Diese Doktorarbeit widmet sich der Verbesserung der HF-Sicherheit von Implantaten in der pTx MRT. Dies geschieht durch die Einführung eines Sicherheitskonzepts für Implantate welches native Patientensicherheit (ohne Implantat) und die durch einen Sensor gemessene Implantatsicherheit separat betrachtet.

Die MRT HF-Sicherheit im nativen Fall als Grundlage dieses Konzeptes wird zuerst simulativ am Beispiel einer pTx Körperspule mit 1 - 16 Kanälen bei 0.5 T, 1.5 T und 3 T untersucht. Die durchschnittliche B_1^+-Feldstärke ($\mathrm{mean}(B_1^+)$) ist dabei für pTx bis zu 30 % größer als bei dem zirkularpolarisierten (CP) Einkanalmodus wenn die Unsicherheit durch unbekannte Patientenmodelle mit einem Sicherheitsfaktor kompensiert und für beide Fälle die gleichen Grenzwerte für die spezifische Absorptionsrate (SAR) der International Electrotechnical Commission (IEC) genutzt werden. Die Positionsunsicherheit des Patienten kann gleicherweise mit einem Sicherheitsfaktor betrachtet werden. Es wurde desweiteren herausgefunden, dass die Vernachlässigung der Phaseninformation bei der Grenzwertbestimmung nur zu einem geringen $\mathrm{mean}(B_1^+)$ Abfall von 3 – 20 % je nach B_0 Feldstärke führt, die nötige Hardwarekomplexität jedoch stark verringert.

Die theoretische Anwendbarkeit des vorgeschlagenen Sicherheitskonzepts wird anhand eines idealisierten Rückenmarkstimulators im zweiten Teil aufgezeigt. Die Fähigkeit, verschiedene Sensortypen gegenüber den etablierten Sicherheitsmetriken SAR und Temperatur zu kalibrierten, wird demonstriert. Das Potential von pTx zur Mitigation der Implantaterwärmung steigt mit der Anzahl der verfügbaren Kanäle. Es wurde für den untersuchten Fall mit maximaler implantatbedingter Temperaturerhöhung von 2 K für 1.5 T und 3 T ein 3-fach höheres $\mathrm{mean}(B_1^+)$ bei 16 Kanälen gegenüber der CP-Anregung gefunden.

Ein möglicher Prozess für Implantathersteller zur Kalibration eines Implantatsensors gegen die durch das Implantat verursachte Erwärmung wird schließlich angerissen.

Abstract

The rising count of patients bearing an active implantable medical device (AIMD) are often hindered from having magnetic resonance (MR) exams because MR-unsafe implants can only be scanned outside of their regulatory approval, while MR conditional implants require the use of thresholds from complex manufacturer- and implant-specific guidelines. This degrades the MR performance because of over-conservative limits or could even endanger patients if the limit is not strict enough. It is known that parallel transmission (pTx)-systems can generate safe optimised radiofrequency (RF)-shims that exploit the full MR performance.

This thesis contributes to implant RF safety in pTx MR by describing an implant safety concept that separates native pTx safety of the patient without implant from implant safety that is assessed with an implant-integrated sensor.

The concept's prerequisite – the RF safety of pTx for the native case – is first demonstrated in silico at the example of a pTx body coil that is driven in different configurations at 1 - 16 channels with 0.5 T, 1.5 T and 3 T. The average B_1^+-field ($\mathrm{mean}(B_1^+)$) of pTx is up to 30 % higher than for the single channel circular polarised (CP) mode when accommodating model uncertainty with a safety factor and the same International Electrotechnical Commission (IEC) specific absorption rate (SAR) limits are applied. Position uncertainty can similarly be addressed with a safety factor. Furthermore, it was found that neglecting phase information leads to minor $\mathrm{mean}(B_1^+)$ drops of 3 – 20 %, depending on the number of channels and B_0 compared to the common SAR-controlled mode, in exchange for a reduced complexity.

The theoretic applicability of the proposed safety concept is shown by simulating a spinal cord stimulator dummy implant in a second step. The ability to calibrate feasible sensor types against the established hazard measures SAR and temperature is demonstrated. The potential of pTx in mitigating implant hazards rises with channel count with up to 3 times the $\mathrm{mean}(B_1^+)$ of the CP mode for an implant-caused temperature rise limit of 2 K at 16 channels for 1.5 T and 3 T.

This thesis finishes with the description of a process for implant manufacturers on how to calibrate a sensor signal against an implant hazard.

Abbreviations, operators and symbols

Abbreviations

ADC analog-to-digital converter

AI artificial intelligence

AIMD active implantable medical device

ASTM American Society for Testing and Materials

BMI body mass index

CC BY 4.0 creative commons attribution 4.0 international lincense that can be found under https://creativecommons.org/licenses/by/4.0/

CEM43°C cumulative equivalent minutes at 43 °C

CP circular polarised

EPT electric properties tomography

FDTD finite-difference time-domain

FPO fixed parameter option

GPU graphics processing unit

IEC International Electrotechnical Commission

IEEE Institute of Electrical and Electronics Engineers

IPG implantable pulse generator

ISO International Organization for Standardization

MIMAS Procedures allowing medical-implant manufacturers to demonstrate compliance with MRI safety regulations (European Metrology Programme for Innovation and Research (EMPIR) project 17IND01)

MR magnetic resonance

MRI magnetic resonance imaging

MROC MR equipment output conditioning

PASCM phase agnostic SAR-controlled mode

PCM power-controlled mode

PEC perfect electric conductor

pTx parallel transmission

PVP polyvinylpyrrolidone

RF radiofrequency

RMS root mean square

ROI region of interest

SAR specific absorption rate

SCM SAR-controlled mode

SNR signal-to-noise ratio

STASIS Standardisation for Safe Implant Scanning in MRI (European Partnership of Metrology project 21NRM05)

UHF ultra high field

VAR volumetric absorption rate

VOP virtual observation point

Operators

operator	**description**
$.^{\dagger}$	complex conjugate transposition
$\hat{.}$	normalised value
$.^{\top}$	transposition

Symbols

symbol[1]	unit	description
i	1	imaginary unit, $\mathrm{i}^2 = -1$
$H, \mathcal{H}$	A m^{-1}	magnetic field (here: H-field)
$B, \mathcal{B}$	T	magnetic flux density (here: B-field)
$E, \mathcal{E}$	V m^{-1}	electric field (here: E-field)
$F, \mathcal{F}$		surrogate for E-field respective H-field
ε_r	1	relative permittivity
ε_0	F m^{-1}	vacuum permittivity, $\varepsilon_0 \approx 8.85 \times 10^{-12}\,\mathrm{F\,m^{-1}}$ [1]
μ_r	1	relative permeability
μ_0	H m^{-1}	vacuum permeability, $\mu_0 \approx 1.26 \times 10^{-6}\,\mathrm{H\,m^{-1}}$ [1]
Φ	T m^2	magnetic flux
d	1	direction of field, values of x, y and z are possible
I	A	current
U	V	voltage
C	F	capacitance
γ	MHz T^{-1}	gyromagnetic ratio, hydrogen: $\gamma/(2\pi) \approx 42.58\,\mathrm{MHz\,T^{-1}}$ [1]
λ	m	wave length
f	Hz	frequency
ω	Hz	angular frequency
t	s	time
j	A m^{-2}	current density
m	kg	mass
ϱ	kg m^{-3}	mass density
σ	S m^{-1}	electrical conductivity
$\mathbf{r} = (x, y, z)$	(m,m,m)	spatial position
N_c	1	channel count
c	1	current channel ID
$\boldsymbol{u}$	1	normalised shim vector
SAR	W kg^{-1}	specific absorption rate
l	W kg^{-1}	SAR limit
$\boldsymbol{Q}$	W kg^{-1}	Q-matrix used to calculate $\mathrm{SAR} = \boldsymbol{u}^\dagger \boldsymbol{Q} \boldsymbol{u}$

[1] Small latin letters also occur as indices and count variables.

1 Introduction

Magnetic resonance imaging (MRI) [2] is a widely used clinical imaging technique notable for its absence of ionising radiation and a good soft tissue contrast. Advancements in medicine led to an increased life expectancy and therefore a higher number of elderly people [3] which benefit from a growing number of MRI scanners [4, 5]. The ageing population also leads to an increasing number of active implantable medical device (AIMD) carriers [6]. Some AIMD can only be scanned conditional or off-label [7].

As small changes in the implant configuration, like the tip position [8–10], can cause large differences in tissue heating, a high safety factor needs to be applied. AIMDs with magnetic resonance (MR) conditional label [11, 12] were introduced in recent years. The process of scanning such implants introduces a single point of failure: the human error of the MR operator, who is responsible for (i) extracting the appropriate limits from complex documents with multiple side-conditions [13–16] and (ii) for limiting the MR scanner accordingly. Another problem lies in the human error of patients that do not remember their specific implant or being addressed on implant-presence at all [17]. Burns caused by MR conditional devices are still reported in 2022 [18]. All this indicates that the presently established workflows still have some issues and that a conceptionally different approach may be needed to overcome these.

The European Society of Cardiology developed procedures to scan even MR unsafe cardiac devices [19], because of the high clinical benefit of available MR images for implant carriers and comparable low heating risk due to the cooling bloodstream through the heart. Appropriate caution and safety margins are recommended by the literature for such scans [20–24]. AIMDs with lead tips located at more susceptible neural tissue with lower perfusion, like deep brain stimulators or spinal cord stimulators, face a higher risk and are therefore harder to justify in an MR exam. A possibility to avoid safety-estimations is the proposed direct measurement of the implant-hazard with integrated physical sensors [25–27].

A parallel transmission (pTx) [28–32] coil with multiple independently controllable channels can shape its transmitted radiofrequency (RF) field, that is used to manipulate the magnetisation, such that the tissue-heating around implants is minimised [9, 10, 33–43]. PTx with more than 2 channels is not commonly available for $B_0 \leq 3\,\mathrm{T}$ scanners [4, 44]. Two reasons for this are (i) the regulatory difference in the IEC SAR limits [45] between single channel and pTx body coils, where local SAR limits are mandated for

pTx coils only despite being commonly violated for one-channel circular polarised (CP) mode coils [46–48], and (ii) little perceived need to improve the B_1^+ homogeneity of single channel body coils compared to ultra high field (UHF) MR with $B_0 \geq 7\,\mathrm{T}$ [49, 50].

The native problem, i.e. ensuring safety for patients without implant, must, however, be solved to use pTx for implant hazard mitigation in a clinical environment. It is possible to deduct the patient's whole body SAR in situ from the measured difference of forward power and reflected power with the body mass [51].

Local SAR is instead commonly estimated by simulation of digital human models within the digital RF coil model [9, 46]. The coil model is known at the design stage of an MR system. The patient, however, is different in each exam and there is in general no exact digital patient model available. Methods to measure such patient model in the MR scanner have been developed.

Conductivity maps and electric permittivity maps of the patient can be measured with electric properties tomography (EPT) [52–56], but there are limitations at tissue borders. A different strategy is the generation of a patient-specific tissue voxel model [57–59] based on Dixon fat/water separated images [60, 61]. The dielectric properties are subsequently assigned to each voxel based on its tissue [62]. Local SAR is then calculated by means of simulation, a process that requires time in the order of hours [63, 64].

A drawback of using patient-specific models for local SAR assessment is the additionally required time for model generation and SAR simulation. Artificial intelligence (AI) techniques were developed in the recent time to speed up the whole process, where the generation of a body model by MR images [65–67], the calculation of local SAR maps from B_1^+ maps [68] or even the direct calculation of local SAR maps from MR images [69, 70] was demonstrated. However, a high amount of diverse and detailed digital human models is required to train the AI models for patient-specific local SAR assessment. Also, remaining uncertainties, that are among other things caused by combining MR scans at multiple positions due to the limited field of view, or breathing [71], still need to be addressed with a safety margin.

A common strategy in studies on pTx RF-safety is therefore the knowledge of the exact digital model of the patient in the exact right position [72–75]. The next step is to infer the consequences for real patients from these results. Deviations in patient model [76–78], position [76, 79] or even breathing state [71] can result in SAR overshoots that need to be addressed with a safety factor or combining the limits of multiple simulations of multiple models, positions and configurations [80].

There is a rapid growth in available digital human models [81] with estimations of around 1000 developed models in 2022 [82]. The number of avail-

able models is, however, still small, and not all these models are commonly accessible because of vendor-locks, licenses and different file formats. A further problem is the development of different digital human models on the basis of the same real world data [83] with the visible human project of 1994 as one prominent example [84] where the male model resulted in models 'VIP-man' [85],'Hugo' [86], 'XCAT' [87], 'visible man' [88, pp. 141–155], and 'Eddie' [89] with the last one being released just in 2022. Native safety must therefore be ensured with a limited number of virtual models.

This work demonstrates the feasibility of an implant safety concept that combines native patient safety, i.e. safety for patients without implant, with a safety limit that can be derived directly from calibrated sensor measurements of an AIMD-integrated hazard sensor, see Fig. 1.1.

This concept requires AIMDs with the following properties:

1. An integrated sensor that outputs a signal which can be calibrated against the implant hazard. The calibration must be independent of the RF coil's field and be valid for all positions of the patient in the scanner. The calibration must also account for the variability of the tissue types that can be found at the implant's hot spots in different patients.

2. It is ensured that the single integrated sensor is sufficient to assess implant safety. Otherwise more sensors need to be added.

3. The AIMD is able to communicate the current implant hazard to the MRI scanner.

This concept unfolds its full potential in a pTx enabled MR scanner, where RF-shims can be optimised based on the implant-sensor measurement and the pre-calculated native safety limit.

Benefits of this concept are the elimination of human errors by the automatic communication of the appropriate implant limits between implant and MR scanner, and in consequence safer MRI exams with higher imaging performance. The higher imaging performance is possible, because implant-caused safety margins can be chosen to be smaller through direct measurement of the safety hazard and optimised pTx RF-shims that result in a low implant hazard and allow for higher RF transmit power.

This thesis is structured into two parts. The first part's aim is the development of a workflow to derive native case limits that ensure RF safety if the patient's digital model and exact position are not known. The workflow is demonstrated by simulation for a body coil that is driven at all combination of 0.5 T, 1.5 T and 3 T and 1-16 channels. Different pTx limits and the single channel CP mode are be compared in respect to their B_1^+ performance.

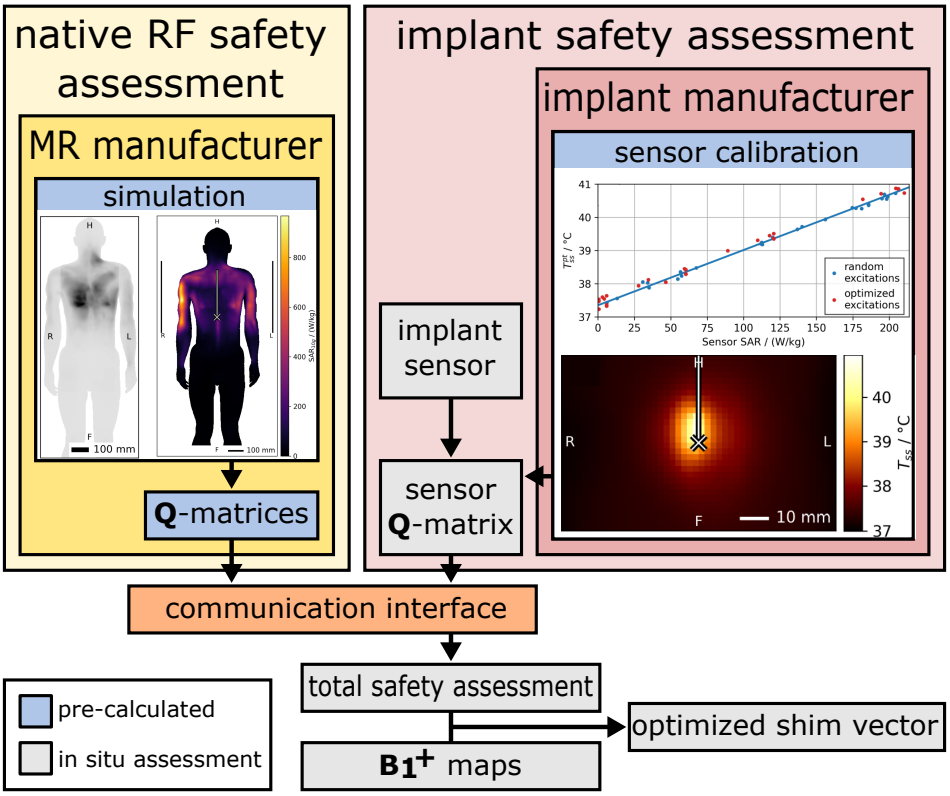

Fig. 1.1: Diagram of the proposed safety concept for AIMDs. The MR system manufacturer is responsible to provide pTx safety limits for patients without implant (native case, left). The implant manufacturer is responsible to provide calibrated sensor information about the implant hazard. With this prior information, a patient and situation specific sensor Q-matrix can be acquired from a short sequence of low-power measurements with the patient in the scanner. Optimised RF-shim vectors can be obtained by combining native and implant Q-matrices with the channel-wise B_1^+ maps. This figure by Petzold et al. [35] is licenced under a creative commons attribution 4.0 international license that can be found under https://creativecommons.org/licenses/by/4.0/ (CC BY 4.0).

The second part's goal is the theoretical proof of the implant safety concept consisting of sensor-placement analysis, finding suitable sensor types and demonstrating that the combination of the sensor signal and the native safety limits, which were derived in the first part, is sufficient to ensure safe MR scans. A further goal is the experimental investigation of a test implant's sensor calibration stability against changes in implant lead position and against the field changes caused by different RF-shim vectors.

This work was performed as part of the projects MIMAS[1] and STASIS[2]. It focusses on the theoretical demonstration and the experimental validation of the core concept (measureability with a sensor) and must be seen in conjunction with the work by Dr. Lukas Winter [90] and Berk Silemek within the same projects [10, 27] on the technical feasibility of the presented safety concept.

Parts of this thesis were the basis of two journal publication [35, 91] and five conference abstracts [76, 78, 92–94].

[1] Procedures allowing medical-implant manufacturers to demonstrate compliance with MRI safety regulations (European Metrology Programme for Innovation and Research (EMPIR) project 17IND01)

[2] Standardisation for Safe Implant Scanning in MRI (European Partnership of Metrology project 21NRM05)

2 Background and underlying concepts

2.1 The radio-frequency field

The MRI principle [95] is based on the macroscopic alignment of spins along an external B-field B_0. Clinical scanners usually use $B_0 \gtrsim 0.5\,\mathrm{T}$ [4] because of a larger signal to noise ratio [96]. The aligned nuclear magnetisation is flipped by a radiofrequency (RF) B_1-field with Larmor frequency ω [97] linked to B_0 by the nucleus-specific gyromagnetic ratio via

$$\omega = 2\pi f = \gamma B_0. \tag{2.1}$$

This work focuses on MR with hydrogen nuclei, where the gyromagnetic ratio is $\gamma_\mathrm{H}/(2\pi) \approx 42.6\,\mathrm{MHz\,T^{-1}}$ [1]. Any processing transversal magnetisation induces a measurable voltage in the receiver coils that can be used in conjunction with switched magnetic gradient fields to acquire the data necessary for image reconstruction [2].

An RF E-field is linked to the B_1-field with Maxwell's equations [98]. This E-field causes energy deposition in the imaged patient due to the electrical conductivity of the tissue and subsequent potentially hazardous tissue heating [99].

The wavelength of the RF field in a medium with permittivity $\varepsilon = \varepsilon_0\varepsilon_\mathrm{r}$, permeability $\mu = \mu_0\mu_\mathrm{r}$, conductivity σ and frequency f is given by

$$\lambda = \frac{1}{f\sqrt{\varepsilon\mu}\sqrt{\frac{1}{2} + \frac{1}{2}\sqrt{1 + \frac{\sigma^2}{(2\pi f)^2\varepsilon^2}}}}. \tag{2.2}$$

The wavelengths λ for 0.5 – 7 T for blood, fat, muscle and nerves at body temperature are shown in Tab. 2.1. Of note is the around four times larger wavelength in fat that leads to a more homogeneous energy deposition compared to the other tissues at the same field strength.

All analysed RF fields between 20 MHz and 300 MHz can cause energy deposition in the surface tissues close to the RF coil. The risk of additional energy deposition in the body core rises with higher B_0 as the corresponding RF wavelength shrinks [103]. Energy deposition in the body core is more dangerous compared to the patient's surface because of the lack of temper-

Tab. 2.1: Frequencies f and wavelengths λ in blood, fat, muscle and nerves corresponding to the used B_0-field strengths in this work. The material parameters conductivity σ and relative permittivity ε_r at body temperature were taken from the IT'IS database [62], that is based on the literature research of C. Gabriel et al. [100] and the measurements of S. Gabriel et al. [101]. The wavelength in water (ε_r at 37 °C taken from [102]) and in air are shown as reference.

		blood			**fat**		
B_0/T	f/MHz	$\sigma/(\mathrm{S\,m^{-1}})$	ε_r	λ/m	$\sigma/(\mathrm{S\,m^{-1}})$	ε_r	λ/m
0.5	21.29	1.14	148	0.30	0.0321	9.43	2.27
1.5	63.87	1.21	86.5	0.20	0.0353	6.51	1.30
3	127.74	1.25	73.2	0.15	0.0369	5.92	0.83
7	298.06	1.32	65.7	0.10	0.0395	5.64	0.41
		muscle			**nerve**		
B_0/T	f/MHz	$\sigma/(\mathrm{S\,m^{-1}})$	ε_r	λ/m	$\sigma/(\mathrm{S\,m^{-1}})$	ε_r	λ/m
0.5	21.29	0.645	107	0.44	0.257	94.0	0.83
1.5	63.87	0.688	72.3	0.29	0.312	55.1	0.44
3	127.74	0.719	63.5	0.20	0.354	44.1	0.28
7	298.06	0.770	58.2	0.12	0.418	37.0	0.15
		air			**water**		
B_0/T	f/MHz	$\sigma/(\mathrm{S\,m^{-1}})$	ε_r	λ/m	$\sigma/(\mathrm{S\,m^{-1}})$	ε_r	λ/m
0.5	21.29	0	1	14.07	0	74	1.64
1.5	63.87	0	1	4.69	0	74	0.55
3	127.74	0	1	2.34	0	74	0.27
7	298.06	0	1	1.00	0	74	0.12

ature perception in the inner body, the presence of more vulnerable tissue and the lack of surface cooling [48].

2.2 Parallel transmission in MR imaging

The typical MRI workflow consists of a single channel body transmit coil that excites the nuclear $^1\mathrm{H}$ spins in the patient [104]. The resulting MR signal is subsequently measured by an array of receive coils. Only transmit coils are considered in the scope of this thesis.

Multiple transmit coils can be combined in phased arrays [105] with independent amplitude and phase of the signal or utilizing full parallel transmission (pTx) [28–32, 106–108] where each channel can be controlled inde-

pendently. The voltage U_c applied to each channel c is thereby, in the most general case, only time t dependent without further restrictions:

$$U_c = U_c(t) \tag{2.3}$$

PTx is a commonly used technique for improving B_1^+ homogeneity for UHF MRI with $B_0 \geq 7\,\mathrm{T}$ [50]. The available degrees of freedom of pTx can also be exploited to shape the RF field so that the SAR at implant hot spots is minimised [9, 36–39, 41, 43]. Current clinical systems with $B_0 = 3\,\mathrm{T}$ commonly have 2 channels [26, 33, 42, 109] that are the orthogonal linear polarisations. Dedicated research scanners with more available channels exist [36–39, 110]. The availability of pTx systems for $B_0 \leq 1.5\,\mathrm{T}$ is currently restricted to custom research scanners [34, 41].

A static pTx RF-shim[1] in the steady state[2] with angular frequency ω is an RF-shim where all channel voltages $U_c(t)$ of the MR coil follow

$$U_c(t) = A\exp(\mathrm{i}\omega t + \mathrm{i}\varphi), \quad \text{with } \mathrm{i}^2 = -1. \tag{2.4}$$

Only signals around the Larmor frequency $\omega = 2\pi\gamma B_0$, see Eq. (2.1), are in the scope of this work. All voltages, currents and spatial field components therefore follow the same time evolution $\exp(\mathrm{i}\omega t)$ in the steady state and can hence be expressed as complex phasor $A\exp(\mathrm{i}\varphi)$ with amplitude A and phase φ.

Static RF-shimming is the most simple type of pTx optimisation that is able to demonstrate the effects of the presented safety limits on imaging performance. More sophisticated optimisation methods like Transmit SENSE [28, 29], Spokes [92, 111, 112] or kT-points [113] exist. They, however, require more optimisation parameters and introduce higher complexity as specially designed sequences are required, while static RF-shimming is compatible with any existent sequence. This work focuses therefore on static RF shimming only, as this allows for a simpler process and thus minimises optimisation artefacts that could arise from the more advanced pTx excitation strategies.

A static RF-shim of a pTx system with N_c channels is, in this work, defined by the N_c complex voltage phasors applied to all channels. Such shim is formalised as unit-less voltage vector $\boldsymbol{u}$ [114] where $U_c = 1\,\mathrm{V} \times u_c$ is the complex

[1] An RF-shim is able to the improve the B_1-field. B_1-shim, B_1^+-shim and RF-shim therefore occur synonymously in the literature. The nomenclature 'RF-shim' is used within this work.

[2] MR pulses have typical bandwidths below 100 kHz which is much smaller than the 20 MHz Larmor frequency of the lowest field strength $B_0 = 0.5\,\mathrm{T}$ used in this work. All signals in this work can therefore be considered quasi-stationary.

voltage of channel c.

The fields[3] $\mathcal{F}$ originating from a single channel with unit voltage excitation $u = 1$ (all other channels: $u = 0$) are named 'single channel fields' within this work. These fields $\mathcal{F} = \mathcal{F}(\boldsymbol{r}, d, c)$ are dependent on the spatial location $\boldsymbol{r} = (x, y, z)$ and are in the general case a set of three complex numbers describing the field components in each spatial direction $d \in \{\mathrm{x}, \mathrm{y}, \mathrm{z}\}$.

The 'mixed fields' F obtained by applying shim vector $\boldsymbol{u}$ to the pTx coil are the result of the weighted superposition of the single channel fields $\boldsymbol{\mathcal{F}}(c)$ due to the linearity of Maxwell's equations [98]:

$$\boldsymbol{F}(\boldsymbol{u}) = \sum_{c=1}^{N_\mathrm{c}} u(c)\boldsymbol{\mathcal{F}}(c). \tag{2.5}$$

Relevant for image quality is the circular-polarized RF B_1^+-field perpendicular to B_0 following the precession of the nuclear spin. This field, applied for pulse duration t_rf, tips the magnetisation out of its initial z-orientation parallel to the external magnetic field B_0. It is defined in this work as

$$B_1^+ = \frac{B_\mathrm{x} + \mathrm{i}B_\mathrm{y}}{2}, \quad \boldsymbol{B} = \mu_r\mu_0\boldsymbol{H}. \tag{2.6}$$

The relative permeability μ_r was set to 1 for the purpose of this work. Both B_0 and the rotation axis of B_1^+ are parallel to the z-axis following the axis convention in the MRI environment. The orientation of B_0 in this framework in $+z$- respective $-z$-direction depends on the sign of the gyromagnetic ratio as consequence of the definition in Eq. (2.6). The direction of B_0 for closed-bore scanners is not standardised and can either point in head direction or in feet direction. The fields in the body, and therefore the energy deposition, depend on the orientation of the patient, which needs to be considered for a comprehensive safety analysis as it is done in available patient exposure databases [115, 116]. Such analysis was not performed within this work due to the higher computational burden and storage requirements compared to the minor scientific gain but is required for MRI manufacturers to test the safety of their native pTx systems if patients shall be allowed to enter the bore head-first and feet-first. Implant manufacturers would need to use appropriate exposure databases depending on the allowed MRI scanners, as well for the verification of their implant calibration.

Relevant for safety is the power deposition P per mass m into the patient.

[3] Symbols $\mathcal{F}$ and F are used as surrogate for all fields used in this work: E,H,B,B_1^+

This quantity, termed specific absorption rate (SAR), is calculated by

$$\mathrm{SAR} = \frac{P}{m} = \frac{1}{2\varrho}\boldsymbol{j}^{\dagger}\boldsymbol{E} = \frac{\sigma}{2\varrho}|\mathbf{E}|^2. \tag{2.7}$$

with current density $\boldsymbol{j} = \sigma\boldsymbol{E}$, mass density ϱ and electrical conductivity σ. Superscript † denotes the complex conjugate transposition. The factor $1/2$ is a result of averaging over a sine period with amplitudes $|\boldsymbol{E}|$ respective $|\boldsymbol{j}|$.

2.3 Hazards caused by devices in MR examinations

Care has to be taken if external or internal medical devices like pulse oximeters or implants are present [117, 118]. Implant bearing patients may suffer severe damage in an MRI exam due to their implant [119, 120] and thus are usually excluded from imaging. Both the number of implant bearers [121] as well as the availability of MRI scanners [4] are increasing over time which raises the pressure to safely scan patients with an implant.

Implant-caused hazards in MRI can be categorised into 5 groups [9, 117, 118, 122]:

1. **Forces and torques on ferromagnetic parts due to B_0**
   Ferromagnetic objects can get attracted by the strong B_0-field of the MRI scanner resulting in the dislocation of implants and subsequent device malfunctioning or damage to the surrounding tissue.

2. **Forces on conductive parts due to movement trough B_0**
   Eddy currents are induced into conductive parts by a changing B-field. These currents create a second B-field that counteracts the initial B-field due to Lenz's law resulting in a force acting on the conductive object.

3. **Device malfunctioning of AIMDs**
   Magnetic switches are used in some AIMDs to trigger certain tasks like forced stimulation in pacemakers. These switches can also be unintentionally activated by the B_0-field [123] and result in unwanted behaviour if no MRI-safe mode exists.

   Another source of malfunctioning is the destruction of the AIMD's electronic components by voltages caused by the RF-fields or B-field gradients of the MRI scanner.

4. **Excessive tissue heating due to the gradients**
   Currents induced into implants by the gradients can lead to implant heating. This heat is conducted to the tissues next to the implant and results in high temperatures and accompanying tissue damage.

5. **Excessive tissue heating due to the RF fields**
   RF currents induced in the patient's tissue close to the implant result in energy deposition and subsequent tissue heating. This effect is most prominent at the tip of leads.

One part of this work focuses on mitigating RF heating for elongated AIMDs leads that can be found in implants like pace makers, deep brain stimulators or spinal cord stimulators.

2.4 Relevant MR safety standards

This section gives a short overview of the established MR RF safety standards [7] by the standardisation bodies International Electrotechnical Commission (IEC), Institute of Electrical and Electronics Engineers (IEEE), International Organization for Standardization (ISO) and American Society for Testing and Materials (ASTM) that are relevant for this work.

Native safety is covered by IEC 60601-2-33 [45] specifying SAR limits for MR exams and IEC/IEEE 62704-1 [124] describing an averaging method to obtain 10 g averaged SAR.

Medical equipment is covered by ASTM F2503-20 [125] for marking devices by their MR compatibility and ISO/TS 10974 [11] that describes test procedures ensuring AIMD safety.

2.4.1 IEC 60601-2-33

IEC standard 60601-2-33 [45] defines three operating modes, namely

normal mode, where the biophysical effect of the energy deposition into the patient results in negligible risk

first level controlled mode, where the biophysical risks are mitigated by appropriate monitoring of the patient and

second level controlled mode, where acceptable limits are defined by a responsible organisation.

Three types of SAR limits with different averaging regions exist. These are

global limits, where SAR averaging either happens for the whole body or the head,

the partial body limit, where averaging happens over the effective volume, that is defined as volume where no more than 95 % of all RF power is deposited in a homogeneous phantom that fills the space that is reachable for a patient and

local limits, where averaging happens for each position $\boldsymbol{r}$ over the closest 10 g mass following the algorithm described in IEC/IEEE 62704-1 [124], see Section 2.4.2. The peak spatial SAR psSAR as maximum SAR over all position $\boldsymbol{r}$ is a commonly used measure for local SAR assessment.

The whole body SAR limits aim to limit physiological stress caused by a systemic temperature rise while the local SAR limits' purpose is to avoid local tissue damage.

The SAR limits l corresponding to these operating modes and limit types for an averaging time of 6 min are shown in Tab. 2.2. The SAR over any 10 s of examination is additionally not allowed to exceed twice the limit specified in Tab. 2.2 to avoid temporal energy deposition peaks.

Tab. 2.2: SAR limits l / (W kg^{-1}) for averaging time 6 min according to [45].

operating mode	global whole body	head	partial body*	local 10 g averaged head/trunk	extremities
normal	2	3.2	2-10	10	20
first level controlled	4	3.2	4-10	20	40
second level controlled	>4	>3.2	>4-10	>20	>40

* The partial body SAR limits l_{pb} depend on the ratio of patient mass in the effective volume of the coil m and total patient mass M with

$$l_{\mathrm{pbn}} = 10\,\mathrm{W\,kg^{-1}} - 8\,\mathrm{W\,kg^{-1}}\frac{m}{M} \quad \text{for normal mode and} \tag{2.8}$$

$$l_{\mathrm{pb1}} = 10\,\mathrm{W\,kg^{-1}} - 6\,\mathrm{W\,kg^{-1}}\frac{m}{M} \quad \text{for first level controlled mode.} \tag{2.9}$$

The partial body SAR limit is expected to be stricter than the whole body SAR limit for mass fractions in the effective volume of $m/M < 0.23$ for normal mode and $m/M < 0.59$ for first level controlled mode, see appendix A.1.

The applicability of the different limits depends on the type of coil. Volume body coils and pTx coils in the single channel CP mode only need to follow the whole body and partial body limit. The local SAR limits do not have to be fulfilled in this case and are commonly violated [46–48]. Local coils and pTx coils must, on the other hand, adhere to the local SAR limits.

Additional limits for the RF field and gradient output at 1.5 T were specified in the 2015 version of the standard [126] as fixed parameter option (FPO) to be available for MR conditional devices. Relevant for this work is the B_1^+ root mean square (RMS) limit of 3.2 µT.

FPO was superseded by MR equipment output conditioning (MROC) for 1.5 T and 3 T in the current standard iteration of the year 2022 [45]. The main difference in terms of B_1^+ RMS is that implant manufacturers can specify a limit instead of only having the pre-specified value at their disposal.

Within this work it is assumed that all SAR limits l of this standard adequately ensure patient safety. The ongoing scientific debate whether SAR is the right quantity to be supervised [127, 128] or certain limit values should be adjusted [47], is not subject of the present work.

2.4.2 IEC/IEEE 62704-1

SAR is commonly calculated with electromagnetic simulations that return the E-field values at each discretised position $\boldsymbol{r}$. These E-fields can be used to calculate for all locations the point SAR, that is the SAR without spatial averaging. The corresponding tissue mass to these locations is usually smaller than 10 g, where the local SAR limits are specified. It is therefore necessary to average the point SAR over multiple positions to obtain the 10 g averaged local SAR.

An algorithm for this purpose is described in IEC/IEEE 62704-1 [124]. Cubes at each position $\boldsymbol{r}$ are expanded until their included mass reaches 10 g and the included SAR values are subsequently averaged. A special case exists for the boundary region between patient and air where the highest averaged SAR value in the vicinity of the current location is used instead. This complex process results in higher SAR values at the boundary compared to volumetric averaging. These high SAR values do not correlate well with temperature due to the heat diffusion from the skin into the air [48].

The volumetric averaging approach was implemented in this work instead of the standardised algorithm as the differences between 10 g- and 10 cm^3-averaging are slim [129]. A sphere as natural shape of heat conduction in isotropic materials was adopted at the same time instead of a cube for a more physics-motivated averaging.

2.4.3 ASTM F2503-20

All devices intended for use in an MR environment can be grouped into three categories depending on their MR safety by marking standard ASTM F2503-20 [125]:

MR unsafe: Devices shall not be used in an MRI environment.

MR conditional: Conditions are specified that must be fulfilled to safely use MR conditional devices in an MRI environment. These conditions could apply, for example, to B_0, B_1, gradient strength or SAR.

MR safe: No restrictions apply in an MRI environment.

This work focuses on MR conditional AIMDs. A procedure to ensure patient safety is described that is based on sensor measurements of the implant that are transferred to the MRI scanner and used for safe excitations. The implant is therefore only safe if the conditions dictated by sensor measurement and calibration are fulfilled.

2.4.4 ISO/TS 10974

Procedures ensuring AIMD safety in MRI are described in ISO/TS 10974 [11]. Tiered measures exist for each hazard type, see Section 2.3. Lower tiers are easier to perform, but require a higher safety factor to compensate for their error margin.

Relevant for this work are the four tiers for assessing the RF induced power deposition:

Tier 1 is restricted to electrically short implants with lengths much shorter than the wavelength of the RF field. The RF-induced power deposition is approximated with predetermined electric field values.

Tier 2 requires the simulation of a digital human model without implant. The RF-induced power deposition is determined with the electric field values in the region intended for the AIMD.

Tier 3 is based on the simulation of an implant-free digital human model. The *in vivo* power deposition is determined with the transfer function formalism [130]. The implant is characterised by the transfer function, which is determined by measurement or simulation, and the incident electromagnetic field distributions along possible implant paths are integrated.

Tier 4 requires a complete electromagnetic simulation of the digital human model including the tested implant.

This work uses a Tier 4 simulation with a simplified implant to achieve insights into the interaction of implant and patient.

2.5 Q-matrices and virtual observation points

Q-matrices [29, 131, 132] are an established concept in RF safety assessment. They are used in this work to simplify the complexity in SAR calculation by unifying all possible SAR limits via normalisation and to reduce the computational burden by calculating a smaller number of dominating Q-matrices that always result in a more conservative SAR [80].

2.5.1 Definition of Q-matrices

The point SAR for static RF-shimming with vector $\boldsymbol{u}$ at location $\boldsymbol{r}$ is given as

$$\mathrm{SAR}_{\mathrm{pt}}(\boldsymbol{u},\boldsymbol{r}) = \frac{\sigma(\boldsymbol{r})}{2\varrho(\boldsymbol{r})}|\boldsymbol{E}(\boldsymbol{u},\boldsymbol{r})|^2. \tag{2.10}$$

It depends on the material parameters at $\boldsymbol{r}$ as well as on the mixed field $\boldsymbol{E}(\boldsymbol{u},\boldsymbol{r})$ (left hand side of Eq. (2.5)) which in turn depends on the RF-shim vector $\boldsymbol{u}$. Calculating point SAR with Eq. (2.10) results in a high complexity and computational load for often required quantities like the 10 g averaged SAR of different RF-shim vectors.

Eq. (2.10) can also be expressed with Q-matrices [29, 131, 132] where the elements are defined as

$$(\boldsymbol{Q}(\boldsymbol{r}))_{m,n} = \frac{\sigma(\boldsymbol{r})}{2\varrho(\boldsymbol{r})}\left(\boldsymbol{\mathcal{E}}(\boldsymbol{r}, c=m)\right)^{\dagger}\boldsymbol{\mathcal{E}}(\boldsymbol{r}, c=n). \tag{2.11}$$

with channel count indices $1 \leq m,n \leq N_{\mathrm{c}}$ as

$$\mathrm{SAR}_{\mathrm{pt}}(\boldsymbol{u},\boldsymbol{r}) = \boldsymbol{u}^{\dagger}\boldsymbol{Q}_{\mathrm{pt}}(\boldsymbol{r})\boldsymbol{u}. \tag{2.12}$$

These Q-matrices depending on the channel basis fields $\mathcal{E}(\boldsymbol{r})$ (right hand side of Eq. (2.5)) with size $(N_{\mathrm{c}} \times N_{\mathrm{c}})$ are hermitian, positive semidefinite and independent of shim vector by definition. SAR calculation with Eq. (2.12) has the advantage that RF-shim independent averaged Q-matrices can be constructed by element-wise averaging of multiple basis Q-matrices resulting in reduced computational load.

2.5.2 Measuring a Q-matrix with an RMS sensor

The Q-matrix concept is not limited to SAR alone and can be used for all quantities x that can be expressed as

$$x = \boldsymbol{u}^{\dagger}\boldsymbol{Q}\boldsymbol{u}. \tag{2.13}$$

A Q-matrix describing the hazard at the critical region of an implant is required for the proposed safety concept. Such Q-matrix can be constructed with a root mean square (RMS) sensor like a diode or a thermistor that measures the amplitude x of a quantity that is correlated to the safety hazard at the relevant location [10]. RMS sensors are suitable for this purpose as they are smaller, simpler and cheaper compared to time-domain sensors because no phase reference is required. On the downside, an increased number of ${N_\mathrm{c}}^2$ measurements are required to determine the sensor Q-matrix Q_s for an N_c-channel system with an RMS sensor instead of N_c measurements with a time-domain sensor. Using a sufficiently fast RMS sensor like a diode results, however, in an adequately small total Q-matrix measurement time of less than 30 ms for an 8-channel system [10].

A possible selection of RF-shim vectors to calculate the sensor Q-matrix is [10]

$$\boldsymbol{Q}_{m,n} = \begin{cases} x_m & \text{for } m = n \\ \frac{1}{2}(x_{m;n=1} - x_m - x_n) + \frac{\mathrm{i}}{2}(x_{m;n=\mathrm{i}} - x_m - x_n) & \text{for } m < n \\ \frac{1}{2}(x_{m;n=1} - x_m - x_n) - \frac{\mathrm{i}}{2}(x_{m;n=\mathrm{i}} - x_m - x_n) & \text{for } m > n \end{cases} \tag{2.14}$$

where x_m is the sensor's amplitude for RF-shim vector $\boldsymbol{u}(m)$ being zero in each component except for one in the m-th component, that is

$$\boldsymbol{u}(m)_l = \begin{cases} 1 & \text{for } l = m \\ 0 & \text{for } l \neq m \end{cases} \tag{2.15}$$

and where $x_{m;n=v}$ is the sensor's amplitude for RF-shim vector $\boldsymbol{u}(m,n,v)$ with

$$\boldsymbol{u}(m,n,v)_l = \begin{cases} 1 & \text{for } l = m \\ v & \text{for } l = n \\ 0 & \text{for } l \neq m \text{ or } l \neq m \end{cases}. \tag{2.16}$$

2.5.3 Normalised Q-matrices

Handling different types of Q-matrices (e.g. local SAR, partial body SAR, diode-measurement) with different limits introduces unnecessary complexity and is error-prone. All N_i Q-matrices $Q^{(i)}$ can be normalised with their respective limit $l^{(i)}$, see Tab. 2.2, to dimensionless matrices $\hat{Q}^{(i)}$ by

$$\hat{Q}^{(i)} = \frac{Q^{(i)}}{l^{(i)}}. \tag{2.17}$$

where carets indicate normalised measures to circumvent this intricacy. The condition for safety is thus simplified to

$$\max_i \boldsymbol{u}^\dagger \hat{\boldsymbol{Q}}^{(i)} \boldsymbol{u} \leq 1. \tag{2.18}$$

2.5.4 Virtual observation points

Local 10 g averaged normalised Q-matrices $\hat{\boldsymbol{Q}}(\boldsymbol{r})$ are similar in close spatial vicinity ('$\boldsymbol{Q}(\boldsymbol{r}) \approx \boldsymbol{Q}(\boldsymbol{r}+\varepsilon)$ for small $|\varepsilon|$'). This redundancy can be removed by calculating a set of N_j Q-matrices $\hat{\boldsymbol{Q}}_{\mathrm{VOP}}^{(j)}$ called virtual observation points (VOPs) [80], which dominate the initial Q-matrices. This means that they result in a more conservative normalised peak spatial SAR $\mathrm{ps}\widehat{\mathrm{SAR}}_{\mathrm{VOP}}$

$$\mathrm{ps}\widehat{\mathrm{SAR}}_{\mathrm{VOP}} = \max_j \boldsymbol{u}^\dagger \hat{\boldsymbol{Q}}_{\mathrm{VOP}}^{(j)} \boldsymbol{u} \geq \max_{\boldsymbol{r}} \boldsymbol{u}^\dagger \hat{\boldsymbol{Q}}(\boldsymbol{r}) \boldsymbol{u} = \mathrm{ps}\widehat{\mathrm{SAR}} \tag{2.19}$$

for all possible $\boldsymbol{u}$ than the $\mathrm{ps}\widehat{\mathrm{SAR}}$ calculated directly with all original Q-matrices $\hat{\boldsymbol{Q}}(\boldsymbol{r})$.

This compression can be used for a combination of all types of Q-matrices. It is especially useful for the native safety assessment with the IEC 60601-2-33 limits, see Section 2.4.1 where the number i of relevant Q-matrices $\boldsymbol{Q}^{(i)}$ lies in the order of magnitude of 10^7 for a typical simulation of a human subject in this work with a 2 mm voxel resolution. Reductions of $N_i \approx 10^7$ to $N_j \approx 100$ are possible in exchange for a few percent of SAR overestimation [133]. It is important to note that the SAR overestimation is calculated for the worst case normalised shim vectors $\hat{\boldsymbol{u}}$ with unit length that is the eigenvector with the highest eigenvalue of all initial Q-matrices. The maximum VOP overestimation of an arbitrary unit length RF-shim vector is hence not relative to its concrete SAR but an absolute difference derived from the worst case [80]. The relative VOP SAR overestimation for RF-shim vectors with low SAR in all initial Q-matrices can therefore reach values

higher than the relative overestimation of the worst case. This is no problem, because the absolute difference matters in safety assessment, and not the relative difference.

The calculated normalised VOPs $\hat{\boldsymbol{Q}}_{\mathrm{VOP}}^{(j)}$ are used in the following instead of all Q-matrices to assess the IEC compliance of a RF-shim. The subscript 'VOP' is omitted for better clarity.

2.6 Ensuring IEC compliance for static RF-shim vectors

The compliance of an RF shim vector $\boldsymbol{u}$ with the IEC SAR limits [45] is in this work assessed with the following three modes that are based on the N_j normalised Q-matrices $\hat{\boldsymbol{Q}}^{(j)}$:

SAR-controlled mode (SCM), where the maximum normalised SAR of a given RF-shim vector $\boldsymbol{u}$ is assessed directly for all $\hat{\boldsymbol{Q}}^{(j)}$:

$$\max_j \boldsymbol{u}^\dagger \hat{\boldsymbol{Q}}^{(j)} \boldsymbol{u} \leq 1. \tag{2.20}$$

This mode is most frequently used in the literature for local SAR [49, 114, 134, 135] as it offers the highest possible $\mathrm{mean}(B_1^+)$ because no information is neglected.

phase agnostic SAR-controlled mode (PASCM), where an upper limit of the normalised maximum SAR based on neglected phase information is used instead:

$$\max_j |\boldsymbol{u}|^\dagger \left|\hat{\boldsymbol{Q}}\right|^{(j)} |\boldsymbol{u}| \leq 1 \quad \text{with } |\boldsymbol{u}|_m = |\boldsymbol{u}_m|, \left|\hat{\boldsymbol{Q}}\right|_{m,n} = \left|\hat{\boldsymbol{Q}}_{m,n}\right| \text{ for } 1 \leq m,n \leq N_\mathrm{c}. \tag{2.21}$$

This mode is examined because the measurement of phase information requires complex hardware and is error-prone as a reference phase is necessary [136]. PASCM is more conservative than SCM because $\boldsymbol{u}^\dagger \hat{\boldsymbol{Q}} \boldsymbol{u} \leq |\boldsymbol{u}|^\dagger \left|\hat{\boldsymbol{Q}}\right| |\boldsymbol{u}|$ follows as consequence of the triangle inequality.

power-controlled mode (PCM) [137], where a single channel amplitude

limit α is defined by

$$\alpha \equiv \min_j \frac{1}{\sqrt{\sum_{i,k=1}^{N_c} \left| \hat{\boldsymbol{Q}}_{i,k}^{(j)} \right|}} \tag{2.22}$$

and IEC compliance can subsequently be assessed by

$$\max_c |u_c| \leq \alpha. \tag{2.23}$$

Eq. (2.23) follows from Hölder's inequality [138], see derivation in appendix A.2. This mode is the most conservative, because the scalar maximum single channel amplitude of an RF-shim vector is used as the only safety measure. PCM is examined because it allows for a direct hierarchy of configurations based on α. It furthermore is possible to calculate a mathematical upper limit normalised SAR $\widehat{\mathrm{SAR}}_{\mathrm{max}}$ for a configuration with maximum single channel amplitude α_{t} for all RF-shim vectors with α_{a} as

$$\widehat{\mathrm{SAR}}_{\mathrm{max}} = \left(\frac{\alpha_{\mathrm{a}}}{\alpha_{\mathrm{t}}} \right)^2, \tag{2.24}$$

see appendix A.2.

2.7 RF-shim vector optimisation

It is necessary to assess the performance of an RF-shim vector quantitatively in order to compare the described safety limits. The following three measures are used in this thesis for this purpose:

'safety' assessed by one of the safety limits as described in Section 2.6,

'average B_1^+ field strength' assessed by the arithmetic mean of B_1^+ in the region of interest (ROI) that is the torso in the image plane that is the z-slice trough the centre of the coil as

$$\operatorname*{mean}_{\boldsymbol{r}\in\mathrm{ROI}}(B_1^+(\boldsymbol{r})) = \frac{1}{N_{\boldsymbol{r}}} \sum_{\boldsymbol{r}\in\mathrm{ROI}} |B_1^+(\boldsymbol{r})| \equiv \mu, \text{ and} \tag{2.25}$$

'B_1^+ homogeneity' assessed by the coefficient of variation (CV) of B_1^+ in

the same ROI as coefficient of standard deviation σ and mean μ as

$$\underset{\boldsymbol{r}\in\mathrm{ROI}}{\mathrm{CV}}(B_1^+(\boldsymbol{r})) = \frac{\sigma}{\mu} = \frac{1}{\mu}\sqrt{\frac{1}{N_{\boldsymbol{r}}}\sum_{\boldsymbol{r}\in\mathrm{ROI}}(|B_1^+(\boldsymbol{r})| - \mu)^2}. \tag{2.26}$$

These three measures are the most simple selection that is sufficient to judge the performance of safe MRI for this work. Different ROI for special imaging needs or non-imaging methods like proton nuclear magnetic resonance spectroscopy are beyond the scope of this thesis.

All three measures must be considered at once. A safe RF-shim vector is necessary but not sufficient for safe and performant MRI. The most extreme example would be the safest possible RF-shim vector $\boldsymbol{u} = 0$ with zero amplitude in all components resulting in zero SAR, but also no B_1^+-field rendering imaging impossible. Likewise unacceptable would be a situation with very high $\mathrm{mean}(B_1^+)$ and $\mathrm{CV}(B_1^+) = 0$ if the safety limits are violated.

Observing three measures, however, results in unnecessary complexity and complicates comparisons between multiple RF-shim vectors. It is hence desired to reduce the number of measures as much as possible. One measure can be eliminated by exploiting the link between SAR and $\mathrm{mean}(B_1^+)$: Scaling an arbitrary static RF-shim vector $\boldsymbol{u}$ with a complex factor a in all components results in a linear increased $\mathrm{mean}(B_1^+(a\boldsymbol{u}))$ and a quadratic increase of $\mathrm{SAR}(a\boldsymbol{u})$ while $\mathrm{CV}(B_1^+(a\boldsymbol{u}))$ is not affected:

$$\mathrm{mean}(B_1^+(a\boldsymbol{u})) \propto \sqrt{\mathrm{SAR}(a\boldsymbol{u})}, \quad \mathrm{CV}(B_1^+(a\boldsymbol{u})) = \mathrm{CV}(B_1^+(\boldsymbol{u})) \text{ for } a \in \mathbb{C}. \tag{2.27}$$

The safety of a RF-shim vector in respect to the described limits is a binary condition and either safe or unsafe. All shim vectors $\boldsymbol{u}$ are hence scaled to hit the respective limit in Eq. (2.20), Eq. (2.21) or Eq. (2.23) to eliminate the safety parameter and reduce the necessary parameters to compare different shim vectors to $\mathrm{mean}(B_1^+)$ and $\mathrm{CV}(B_1^+)$.

The trade-off between $\mathrm{mean}(B_1^+)$ and $\mathrm{CV}(B_1^+)$ of an RF-shim vector $\boldsymbol{u}$ scaled to hit a specific SAR limit can be assessed with cost function

$$C = C(\mathrm{mean}(B_1^+), \mathrm{CV}(B_1^+)) = C(\boldsymbol{u}). \tag{2.28}$$

The number of parameters to assess a RF-shim vector can therefore be reduced to one for a given C. It is worth noting that all RF-shim $a\boldsymbol{u}$ for an arbitrary complex a will have the same cost assigned due to the scaling.

A linear combination of $\mathrm{mean}(B_1^+)$ and $\mathrm{CV}(B_1^+)$ was chosen in this work

as cost function

$$C(\boldsymbol{u}_\mathrm{s}) = -\operatorname*{mean}_{\boldsymbol{r}\in\mathrm{ROI}}(B_1^+(\boldsymbol{r},\boldsymbol{u}_\mathrm{s})) + \lambda \operatorname*{CV}_{\boldsymbol{r}\in\mathrm{ROI}}(B_1^+(\boldsymbol{r},\boldsymbol{u}_\mathrm{s})) \tag{2.29}$$

with regularisation parameter $\lambda \in \{0, 0.2, 0.5, 1, 1.8, 3, 5, 10, 30, \infty\}$ as this represents the simplest combination of both measures that allows to specify weighting. λ = '∞' symbolizes that only the second term assessing B_1^+ homogeneity in Eq. (2.29) is regarded analogously to $\lambda = 0$ for B_1^+ field strength.

The shim vectors with the lowest cost C (the 'best' shim vectors) for at least one $\lambda \in [0, \infty)$ form the L-curve[4] that describes the best possible trade-offs between $\mathrm{mean}(B_1^+)$ and $\mathrm{CV}(B_1^+)$.

Scaling an RF-shim vector to hit the safety limit results for N_c-channels in $2N_c - 2$ degrees of freedom: $N_c - 1$ relative amplitudes and phase differences to the first channel. Rasterising the whole manifold of possible scaled RF-shim vectors results in an exponential increase of the necessary RF-shim vector count N_u with channel count N_c: $N_\mathrm{u} = b^{N_\mathrm{c}-1}$ where b is the product of the desired number of tested phases and the desired number of tested amplitudes per channel. It is as consequence not feasible to test a sufficient count of possible RF-shim vectors for channel counts $N_c \geq 8$ with current computational resources. Two strategies are hence used in this thesis to explore the RF-shim vector manifold, namely a

Monte Carlo approach, where 10^6 random RF-shim vectors, half with random phases and identical amplitude and half with both random phases and amplitudes, are scaled to hit the safety limit and $\mathrm{mean}(B_1^+)$ and $\mathrm{CV}(B_1^+)$ are subsequently evaluated and a

cost function optimisation approach, minimising the cost function C (Eq. (2.29)) for the RF-shim vectors that hit the safety limit and the specified regularisation parameter λ.

Minimising C in Eq. (2.29) is a non-convex optimisation problem as it shows local minima. Optimisation with a single initial shim vector will therefore not guarantee the global minimum and multiple initial shim vectors are used to mitigate this problem. Here, the Nelder-Mead algorithm [139] is used for optimisation as no derivatives of the cost function are necessary, which simplifies the implementation.

The required time of one optimisation run for one initial RF-shim vector is much higher than the calculation of C for a single RF-shim vector

[4] The more common name 'L-curve' was adapted throughout this work instead of 'Ⅎ-curve' that better describes the plots of this work.

with observations of up to 10^5 times longer time for the optimisation runs in this work. It was therefore decided to use the 100 shim vectors with lowest cost C for any λ from the Monte Carlo approach as the initial RF-shim vectors for optimisation to reduce the computational burden.

It is, in conclusion, possible to assess the performance of a RF-shim vector with a single scalar – the value of the cost function for a given regularisation parameter λ – enabling straightforward comparisons between different RF-shim vectors.

3 Simulations and data analysis

This chapter describes the applied methods to derive the necessary data for the further analysis, that contains B_1^+-maps, SAR maps, SAR VOPs, and temperature maps for given RF-shim vectors.

3.1 Electromagnetic FDTD simulation background

The inability to analytically solve complex electrodynamic problems, like the resulting fields in a patient for a given RF-shim in an MRI coil, sparked the development of numerical procedures to approximate Maxwell's equations [98]

$$\operatorname{div} \boldsymbol{E} = \frac{\rho}{\varepsilon_0} \qquad \text{Gauß's law,} \tag{3.1}$$

$$\operatorname{div} \boldsymbol{B} = 0 \qquad \text{Gauß's law for magnetism,} \tag{3.2}$$

$$\operatorname{rot} \boldsymbol{E} = -\frac{\partial \boldsymbol{B}}{\partial t} \qquad \text{Faraday's law and} \tag{3.3}$$

$$\operatorname{rot} \boldsymbol{B} = \mu_0 \boldsymbol{j} + \mu_0 \varepsilon_0 \frac{\partial \boldsymbol{E}}{\partial t} \qquad \text{Ampère's law.} \tag{3.4}$$

The finite-difference time-domain (FDTD) method, introduced by Yee [140] in 1966, is used in this thesis. Only a course outline can be given within this section. Details can be found in dedicated literature [141] and lectures [142].

The FDTD calculation happens, as suggested by its name, in the time domain where an initial configuration of E- and B-field is updated. The method is voxel-based like MRI with the slight difference that the E- and B-fields are located on two rectangular meshes that are shifted by half of their edge length in all three dimensions: the so-called Yee-cell, see Fig. 3.1. This setup leads to the automatic fulfilment of Eqs. (3.1) and (3.2).

E- and B-field are updated with a leap-frog algorithm by the second-order approximation of Eqs. (3.3) and (3.4) in space and time: The change of the E-field is calculated by the rotation of the B-fields surrounding the E-field grid point. In a next step, all B-fields are updated likewise. The leap-frog algorithm can be heavily parallelised, leading to smaller simulation computation times when appropriate hardware is available.

The main advantage of the FDTD approach is the linear correlation be-

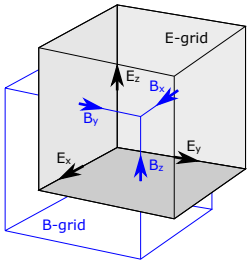

Fig. 3.1: Schematic of a Yee-cell with the location of the E-field- and B-field-components. E- and B-grid are shifted by half of the grid length.

tween number of voxels and required memory enabling this method for large geometries like human voxel models with typical dimensions of $2\,\mathrm{m} \times 0.8\,\mathrm{m} \times 0.8\,\mathrm{m}$ that result in a mesh of size $1000 \times 400 \times 400$ with 160 million cells for a grid length of 2 mm. The typical computation time until steady-state was reached with a NVIDIA Quattro GV100 graphics processing unit (GPU) for all 48 ports was around 8 h for the analysed models in this work at 128 MHz.

Resonant systems like MR-coils with a high quality factor Q require a long time to reach the steady-state. Numerical instability might happen for a system with too high Q and not enough energy loss at the simulation boundaries. High Q-factors can be avoided by employing electromagnetic co-simulation, see Section 3.3.2.

The total calculation time of a single simulation t_c scales with grid length g and simulation frequency f roughly by

$$t_\mathrm{c} \propto \frac{1}{g^4 f}. \tag{3.5}$$

The spatial resolution results in g^{-3} due to the higher count of cells and the required smaller time update step Δt_u with $t_\mathrm{c} \propto 1/\Delta t_\mathrm{u}$ for a fixed total simulated time results in another g^{-1} as it is linked to the grid length g by the speed of light c with $\Delta t \propto g/c$. Higher resolution $r = 1/g$ therefore leads to a significantly longer total simulation calculation time $t_\mathrm{c} \propto r^4$. The factor f^{-1} is a result of assuming a similar number of necessary periods of the RF field to reach steady state.

The FDTD simulation method is, in conclusion, a suitable approach to obtain the necessary field distributions in human models for the further analysis. It should be noted, however, that the required computational resources rise rapidly with decreasing grid length g. It is hence not possible to simulate fine structures like implants within a large model in detail when using a Tier 4 approach, see Section 3.4.

3.2 Electromagnetic FDTD simulation setup

3.2.1 Workflow

All simulations were carried out with the software Sim4Life (ZMT, Zürich, Switzerland) version 5.0 - 7.0. The simulation workflow was structured in 3 steps:

modeling: The simulation geometry was determined.

simulation: Mass density ϱ, relative permittivity ε_r and electrical conductivity σ were assigned to each tissue type of the virtual human models according to the IT'IS Foundation's tissue properties database version 4.0 [62]. The measured values were used for phantom liquids. Spatial discretisation (meshing) of all objects was performed with 2 mm grid length in all 3 dimensions if not stated otherwise. The outermost border of the mesh was determined by a rectangular cuboid to ensure the right grid location and minimise meshing artefacts, especially for ports. The default uniaxial perfectly matched layers (UPML) absorbing boundary condition (ABC) was used. Multiport simulations were carried out to speed up total simulation time, see Section 3.3.2. Thereby all ports were terminated by a 50 Ω load and simulations were carried out where one port each acted as sinusoidal voltage source with frequency $f = \gamma B_0$, see Eq. (2.1) and Tab. 2.1. The simulation run of one port was finished when the steady state was reached, that is assumed when the convergence level based on the difference of the last two periods reached −50 dB. The simulation results consist of the complex phasors of E-field and H-field at each voxel location, as well as the phasors of voltage and current of each port in the steady state, and are stored by Sim4Life with the material parameters of each voxel in `*.h5` hierarchical data format files.

analysis: The results of Sim4Life were analysed with Python scripts.

3.2.2 Coil and phantoms

Birdcage coils [143–145] like the one simulated in this thesis are considered state of the art for body coils with $B_0 \leq 3\,\mathrm{T}$ and are represented in generic exposure data bases [115, 116].

The simulated coil was modelled after the coil of a 3 T Siemens Verio (Siemens Healthineers, Erlangen, Germany) wide-bore system (70 cm), see

Fig. 3.2. The purpose of this coil is to simulate human voxel models to assess safety and performance of optimised RF-shim vectors.

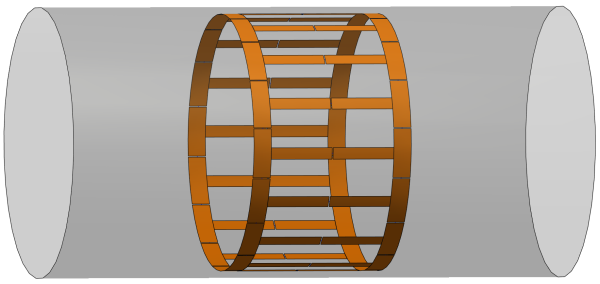

Fig. 3.2: Body coil model with 48 ports. Gray: shield, orange: coil, gaps in coil: location of ports.

field strength: 0.5 T, 1.5 T and 3 T

channel count: 1 ch, 2 ch, 4 ch, 8 ch and 16 ch

coil: radius 356 mm, leg length: 352 mm, leg width: 32 mm, endring thickness: 50 mm, material: perfect electric conductor (PEC)

ports: 48 ports in total: 16 ports in the centre of each leg, 16 ports each between the legs in both endrings

shield: length: 1500 mm, radius: 376 mm, material: PEC

phantoms: It is assumed that there are over 1000 digital human models [82]. Their accessibility is however lowered by licences, fees, vendor locks limiting models to specific software and technical difficulties like various proprietary file formats [81]. Only 11 models based on 10 different humans are analysed in this work due to these constraints. More models would certainly be desirable, but the presented principle is not expected to change. These 11 analysed models consist of 10 of the virtual population [146] (Dizzy, Eartha, Louis, Yoon-sun, Ella, Glenn, Jeduk, Duke, Eddie and Fats) and the original XCAT model [87]. All phantoms were positioned like in cardiac imaging with their heart in the central z-plane of the coil and back touching the $y = -170\,\mathrm{mm}$ plane to explore model dependency. Model Duke was additionally used in various other positions to explore position dependency.

3.3 Data processing

3.3.1 Field data extraction

Simulation results of E-fields and H-fields are saved by Sim4Life at shifted positions in the Yee-Grid as one complex number per spatial direction, see Fig. 3.1. A linear interpolation like in Sim4Life is integrated in the developed analysis scripts to get the fields at the same positions for verification purposes. The interpolation is dependent on the spatial direction d. With grid length a follows:

$$\mathcal{E}_{\mathrm{x}}(x,y,z) = \frac{1}{4}\sum_{\pm}\mathcal{E}_{\mathrm{x}}\left(x, y \pm \frac{a}{2}, z \pm \frac{a}{2}\right) \tag{3.6}$$

$$\mathcal{H}_{\mathrm{x}}(x,y,z) = \frac{1}{2}\sum_{\pm}\mathcal{H}_{\mathrm{x}}\left(x \pm \frac{a}{2}, y, z\right) \tag{3.7}$$

$$\mathcal{E}_{\mathrm{y}}(x,y,z) = \frac{1}{4}\sum_{\pm}\mathcal{E}_{\mathrm{y}}\left(x \pm \frac{a}{2}, y, z \pm \frac{a}{2}\right) \tag{3.8}$$

$$\mathcal{H}_{\mathrm{y}}(x,y,z) = \frac{1}{2}\sum_{\pm}\mathcal{H}_{\mathrm{y}}\left(x, y \pm \frac{a}{2}, z\right) \tag{3.9}$$

$$\mathcal{E}_{\mathrm{z}}(x,y,z) = \frac{1}{4}\sum_{\pm}\mathcal{E}_{\mathrm{z}}\left(x \pm \frac{a}{2}, y \pm \frac{a}{2}, z\right) \tag{3.10}$$

$$\mathcal{H}_{\mathrm{z}}(x,y,z) = \frac{1}{2}\sum_{\pm}\mathcal{H}_{\mathrm{z}}\left(x, y, z \pm \frac{a}{2}\right) \tag{3.11}$$

This interpolation has negligible effects on 10 g averaged local SAR.

3.3.2 Co-Simulation

The linearity of Maxwell's equations, see Eqs. (3.1) to (3.4), can be exploited by a technique called co-simulation [147]. Electrical elements like capacitors are replaced with ports in the simulation step. These ports are terminated by a load and simulations happen consecutively where one port each acts as voltage source and the resulting fields of this configuration are calculated. The desired fields of the original system are subsequently obtained by superposition of the calculated fields with weighting factors corresponding to the equivalent circuits at all ports. Software packages implementing this process are available open-source [148].

This approach is especially attractive for simulating highly resonant systems like MR coils with a high Q-factor that would require a long simulation time to converge or even fail to converge at all due to numerical instability.

Replacement of the capacitors with loads results in lower Q that can lead to a lower total computational load even though more simulations are required. Another use case is coil design, where the specific capacities are not known beforehand. The time-consuming simulation needs to be carried out just once in this case and the sub-simulation fields can nearly instantly be linearly combined, depending on the desired electric circuits.

This work employs a simplified co-simulation approach where the voltage in each port is set directly for each coil configuration. This approach eliminates uncertainties between feeding lines and current flowing in the coil caused by the tuning and matching circuits as well as decoupling, see Fig. 3.3, and enables the rapid generation of different coil configurations with different channel counts and RF frequency.

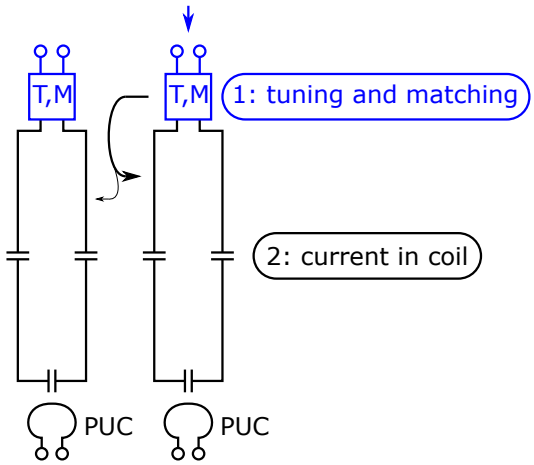

Fig. 3.3: The uncertainty of the current flowing in the coil can be minimised by measuring the current in the coil directly with pick up coils (PUCs) instead of measuring the current at the feeding lines and considering all intermediate steps.

The employed simplified approach assuming the knowledge of the actual current in each channel of the coil is not limiting, as the current can be measured with time-domain pickup coils [136] that, additionally, can act as safety watch-dog. It is assumed that these pickup coils could be implemented with RMS sensors in conjunction with the algorithm described in Section 2.5.2 to generate a matrix linking the current applied before the tuning and matching circuits with the current flowing in each coil element. This would result in lower complexity and cost as no phase-information is needed.

The simplified co-simulation results, in conclusion, in no loss of generality, while error sources are eliminated.

Body coil

Superpositioning the raw single channel fields $\boldsymbol{\mathcal{F}}(48, p)$ $(1 \leq p \leq 48)$ of the 48 port simulation with port-to-channel-conversion-matrices $u(N_\mathrm{c}, c, p)$ for all locations r, directions d and channel counts $N_\mathrm{c} \in \{1, 2, 4, 8, 16\}$ with $1 \leq c \leq N_\mathrm{c}$ results in the body coil single channel fields $\boldsymbol{\mathcal{F}}(N_\mathrm{c}, c)$ of the desired configuration by

$$\boldsymbol{\mathcal{F}}(N_\mathrm{c}, c) = \sum_{p=1}^{48} \boldsymbol{u}(N_\mathrm{c}, c, p)\boldsymbol{\mathcal{F}}(48, p). \tag{3.12}$$

The port-to-channel-conversion matrices $\boldsymbol{u}(N_\mathrm{c}, c, p)$ with size $(N_\mathrm{c} \times 48)$ were derived by a simplified idealised electromagnetic co-simulation as described in the following.

The voltages $\boldsymbol{U}_\mathrm{a}(c, p)$ incorporating the $Z_0 = 50\,\Omega$ loads in the FDTD simulation are calculated with the (48×48) Z-matrix $\boldsymbol{Z}(p, k)$, current $\boldsymbol{I}(c, p)$ and voltage before the resistor $\boldsymbol{U}_\mathrm{w}(c, p)$ by

$$\boldsymbol{U}_\mathrm{a}(c, p) = \boldsymbol{U}_\mathrm{w}(c, p) + Z_0\boldsymbol{I}(c, p) \tag{3.13}$$

$$\boldsymbol{U}_\mathrm{w}(c, p) = \sum_{k=1}^{48} \boldsymbol{Z}(p, k)\boldsymbol{I}(c, k). \tag{3.14}$$

Equation (3.14) is solved for $\boldsymbol{I}(c, p)$ with physically feasible values for $\boldsymbol{U}_c(c, p)$, see Fig. 3.4.

Inserting $\boldsymbol{U}_\mathrm{w}(c, p)$ and $\boldsymbol{I}(c, p)$ into Eq. (3.13) results in $\boldsymbol{U}_\mathrm{a}(c, p)$ that can be normalised with 1 V to obtain the wanted conversion matrices $\boldsymbol{u}(c, p)$ by

$$\boldsymbol{u}(c, p) = \frac{\boldsymbol{U}_\mathrm{a}(c, p)}{1\,\mathrm{V}}. \tag{3.15}$$

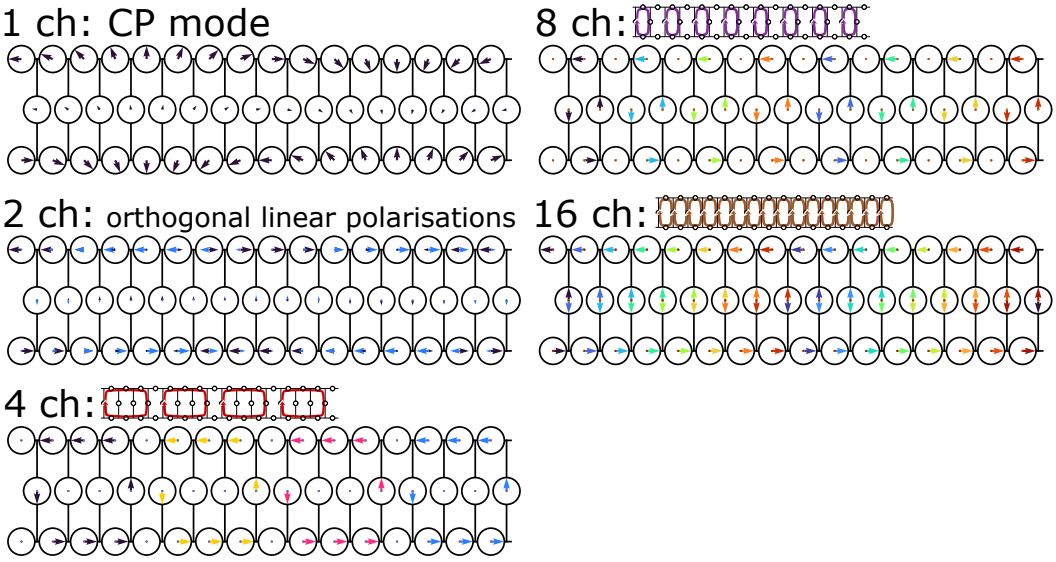

Fig. 3.4: The channel configurations of the body coil displayed on the unwound wiring schematic with the wanted voltages of each channel displayed as phasors at the appropriate port. The 8 channel configuration is a proper subset of the 16 channel configuration. This figure by Petzold et al. [91] is licenced under CC BY 4.0.

3.3.3 Relevant SAR values

This section describes the derivation of the necessary Q-matrices for the safety assessment following IEC 60601-2-33 [126], see Section 2.4.1. The calculation is based on the point Q-matrices $\boldsymbol{Q}_{\mathrm{pt}}(\boldsymbol{r})$ at each location $\boldsymbol{r}$ in the model.

The analysed human voxel models [87, 146] were segmented into torso, head and extremities, see Fig. 3.5. A simple approach with manually set border-planes was adapted as this is sufficient for the purpose of this work. It is not expected that a more sophisticated anatomical orientated segmentation leads to different results. The arms of model Jeduk were spread by 3° in order to avoid body-loop related RF-induced heating [149–151], see Figs. A.1 and A.2. A body-loop caused hotspot for model Glenn at 0.5 T was masked.

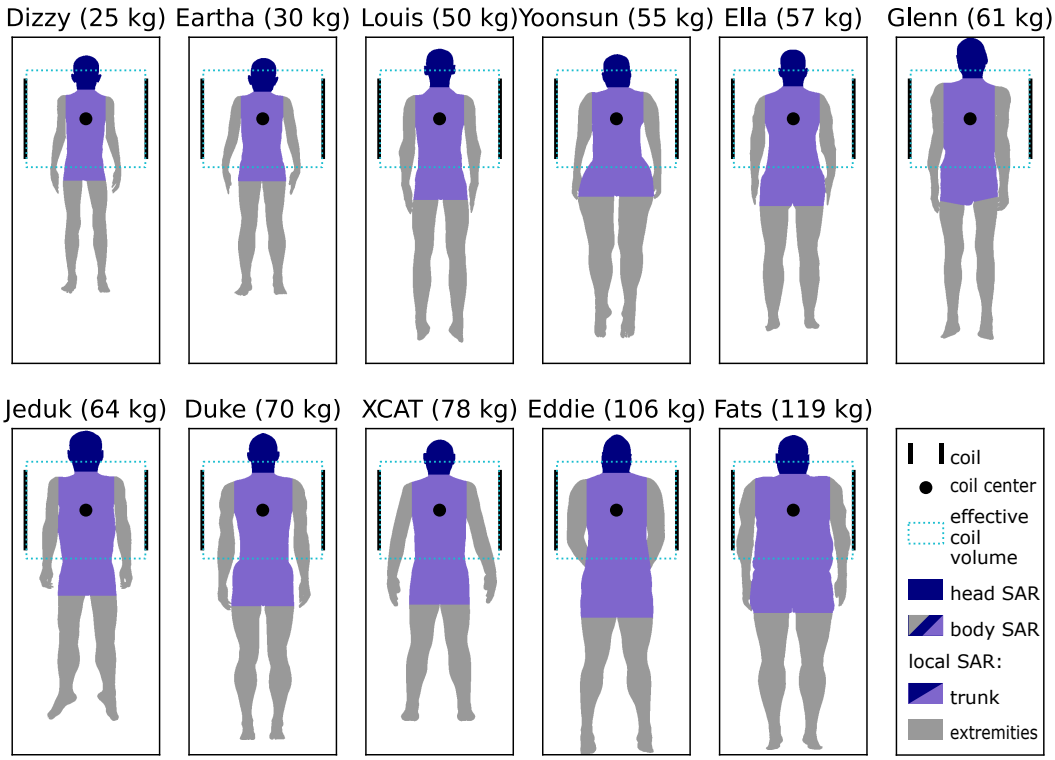

Fig. 3.5: The 11 in this work simulated human models [87, 146] placed so that their heart is in the image plane that is the axial slice trough the centre of the coil. The coloured regions specify which SAR limit applies. The effective coil volume absorbs 95 % of all energy when a homogeneous phantom is used. This figure by Petzold et al. [91] is licenced under CC BY 4.0.

Whole body and head SAR

The whole body Q-matrix $\boldsymbol{Q}_{\mathrm{wb}}$ and the head Q-matrix $\boldsymbol{Q}_{\mathrm{hd}}$ were calculated as element-wise mean value of the point Q-matrices in the respective volumes:

$$(\boldsymbol{Q}_{\mathrm{wb/hd}})_{m,n} = \operatorname*{mean}_{\boldsymbol{r}\in\mathrm{wb/hd}} \left[(\boldsymbol{Q}_{\mathrm{pt}}(\boldsymbol{r}))_{m,n} \right]. \tag{3.16}$$

Partial body SAR

The effective volume required for partial body SAR averaging is defined in IEC 60601-2-33 [45] as

> ‘[…] that volume in which no more than 95 % of the total absorbed RF power is deposited inside a homogeneous material which fills the volume normally accessible by the PATIENT.’ [45]

The simplest conservative approach was chosen in this work to determine the effective volume fulfilling this definition where there is room for interpretation. A homogeneous cylinder phantom (length: 2000 mm, radius: 330 mm, $\sigma = 0.35\,\mathrm{S\,m^{-1}}$, $\varepsilon_r = 43.8$) was simulated in the body coil as natural shape of the closed bore scanner, see Fig. 3.6A. An efficient RF-shim vector optimisation requires a single partial body Q-matrix per configuration which, in turn, demands an effective volume independent of shim vector. It was therefore decided to use the CP mode as representative for all other shim vectors to calculate the effective volume extension to reduce complexity. The effective volume geometry was, in this work, set as a cylinder ranging in z-direction from $-z_{\mathrm{eff}}$ to z_{eff}, following the coil symmetry and the rising conservativeness of the partial body SAR limit for smaller effective volumes, see appendix A.1. The normalised absorbed RF power in each z-slice of the phantom as function of z-position is shown in Fig. 3.6B so that the integral over the curve is equal for all curves.

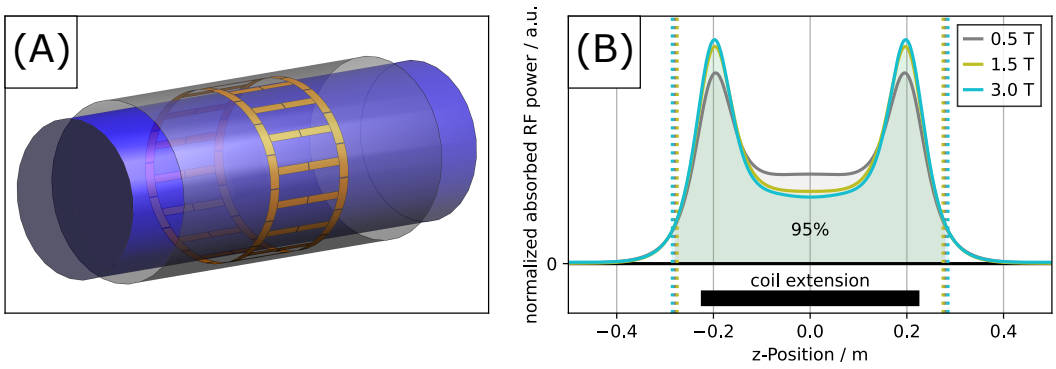

Fig. 3.6: Setup to determine the effective volume where 95 % of the energy of the used RF birdcage body coil is deposited. (**A**) Simulation setup with homogeneous cylinder phantom (blue). (**B**) Absorbed RF power per z-slice as a function of z-position normalised so that the integral over all curves is identical. The respective effective volumes are filled under the curves. This figure by Petzold et al. [91] is licenced under CC BY 4.0.

The lengths of the effective volume in z-direction $L_{\mathrm{eff}} = 2z_{\mathrm{eff}}$ do not show a high B_0 dependency and lie with approximately 560 mm around 25 % over the coil lengths of 452 mm, see Tab. 3.1.

The point SAR Q-matrices $\boldsymbol{Q}_{\mathrm{pt}}$ in the effective volume were element-wise averaged analogously to Eq. (3.16) to obtain the partial body Q-matrix $\boldsymbol{Q}_{\mathrm{pb}}$.

It is worth noting that the whole body SAR limit is expected to be more conservative for normal mode when the patient's mass fraction in the effective volume is above 23 %, see appendix A.1. It is hence expected for the analysed cases of body imaging that the partial body SAR limit is not

Tab. 3.1: The lengths of the effective volume in z-direction L_{eff} of the birdcage body coil as function of B_0-field strength.

B_0/T	$L_{\text{eff}}/\mathrm{mm}$
0.5	558
1.5	550
3	570

restricting. This would not be the case for first level controlled mode where the cut-off mass fraction is at 59 %.

Local SAR

This work adapted a volumetric absorption rate SAR averaging approach instead of the standardised method [124] because of a hugely reduced complexity and similar results [129], see Section 2.4.2.

The local SAR Q-matrices $\boldsymbol{Q}_{10\,\mathrm{g}}(\boldsymbol{r}) \approx \boldsymbol{Q}_{10\,\mathrm{cm}^3}(\boldsymbol{r})$ are the result of element-wise convolution of the $\boldsymbol{Q}_{\text{pt}}(\boldsymbol{r})$ with a 10 cm^3 spherical kernel that was discretised on the 2 mm simulation grid assuming a uniform mass density of 1000 $\mathrm{kg\,m^{-3}}$ like water. The SAR limits $l(\boldsymbol{r})$ according to the matrix location $\boldsymbol{r}$ were applied after convolution.

Inconsistency between IEC SAR-limits for 1-channel coils and pTx coils

The IEC standard's local SAR limits are not required for single channel body coils [45] and are commonly violated when scaling an RF-shim vector to hit the whole body SAR limit [46–48, 91].

For the tested human voxel models of this work, the local SAR limit is violated by up to factor 4 when the CP mode RF-shim is scaled to hit the normal mode whole body SAR limit while partial body SAR and head SAR are below their respective limits, see Fig. 3.7.

For the rest of this work, the local SAR limits were enforced for all coil configurations and especially the single channel CP mode. This has the advantage of a more physics-based safety assessment which avoids performance differences caused by different limits. The achievable $\mathrm{mean}(B_1^+)$ of the CP mode is on the other hand reduced.

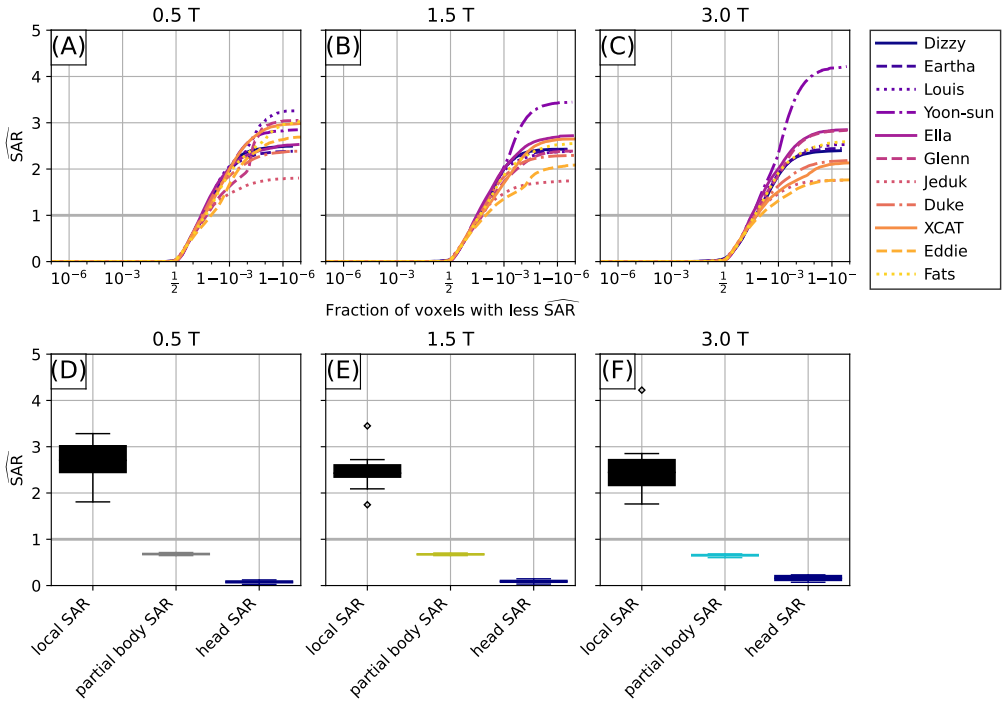

Fig. 3.7: Inconsistency between whole body and local SAR limits. The CP mode was scaled to hit the whole body SAR limit. Normalised SAR values for the 11 human voxel models of this work. (**A-C**) Distribution of normalised local SAR. The local SAR limits l are position dependent, see Tab. 2.2. Please note the logit x-scale. (**D-F**) Distribution of the maximum normalised local SAR, normalised partial body SAR and normalised head SAR. This figure by Petzold et al. [91] is licenced under CC BY 4.0.

3.3.4 VOP calculation

VOP compression of all normalised Q-matrices of each configuration was performed in this work with Lee's algorithm [152] in the implementation of Orzada et al. [133]. The published Matlab script was interfaced with a Python script, because it was was around ten times more time efficient than a reimplementation in Python even though this resulted in a higher complexity and more points of failure.

The VOPs of the native configurations were calculated with 2 % final overestimation (initial overestimation: 16 %, divider steps: 0.5, iterations: 4) of the SAR of the eigenvector with highest eigenvalue of all original Q-matrices [133] for the native case without implant if not stated otherwise.

The eigenvector with the highest eigenvalue of the implant configurations is much larger than for the native case, see for example Fig. 3.8 where a factor of 5 can be found.

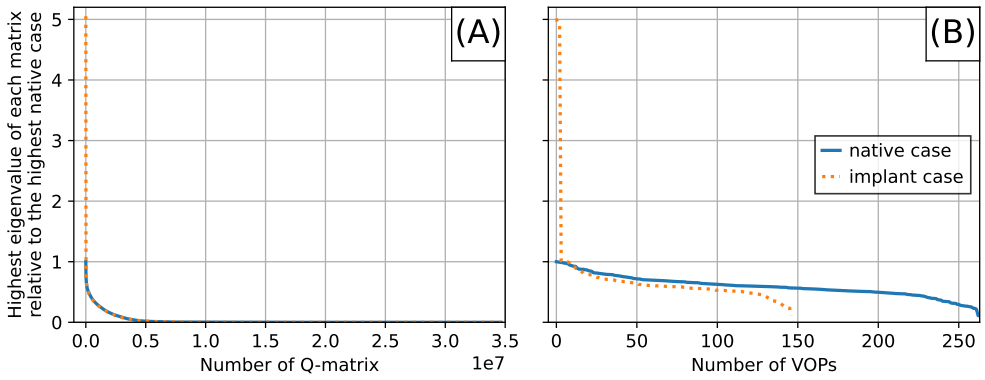

Fig. 3.8: The highest eigenvalues of each Q-matrix sorted from high to low for implant case and native case relative to the highest eigenvalue of the native case. Human voxel model Duke at 3 T and 8 channels in cardiac imaging position. (**A**) All Q-matrices. (**B**) All derived VOPs.

A final overestimation of 0.25 % was therefore used for the implant case VOP compression to compensate for the higher worst case SAR and to avoid a high level of VOP compression noise. Such a low overestimation for all native simulations resulted in a high VOP calculation time due to the exponential growing computation load [133, 153], while there was no benefit, as the introduced error for 2 % overestimation of the native case is small against numerical simulation differences caused by varying phantom-meshing and small phantom-position shifts below 2 mm, see Section 4.4. The 2 % overestimation VOP for the native case was therefore not changed.

3.4 Implant simplifications

The total simulation calculation time t_c rises rapidly with decreasing grid length g, see Eq. (3.5). Full Tier 4 simulations of a human voxel model with a detailed implant in high resolution are hence not feasible due to the high computational load required by an appropriate large grid with fine resolution. The computational load can be significantly reduced by replacing the implant with an appropriate effective model. Such an effective model can be constructed for a straight wire implant on the centre of the E-field nodes [35], see Fig. 3.9.

An ideal skin-effect with a field-free wire is assumed. This limits the current-flow to the conductor's surface. There is no current in the axial layer due to insulation. The displacement current is neglected, as the wire's diameter is much lower than the wavelength, see Tab. 2.1.

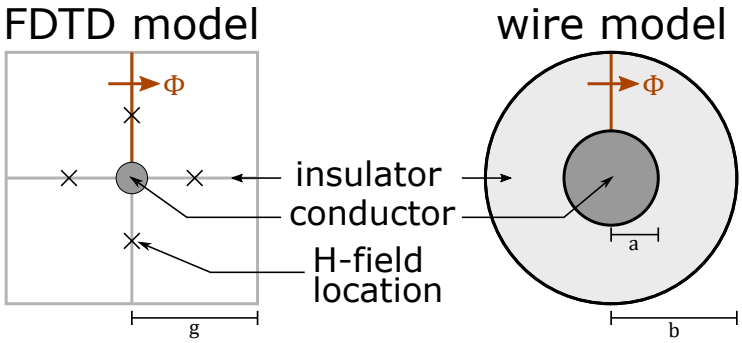

Fig. 3.9: Insulated implant as thin wire in a FDTD grid and in the wire model. This figure by Petzold et al. [35] is licenced under CC BY 4.0 and was adapted by separating FDTD model and wire model.

The effective diameter of a one-dimensional wire on the FDTD grid is calculated first with the magnetic flux per unit length $\Phi/l = \int B\mathrm{d}r$ of current I. For the FDTD model follows

$$\frac{\Phi}{l\mu_0} = \int_0^g H\mathrm{d}r = \int_0^g \frac{I}{4g}\mathrm{d}r = \frac{I}{4}. \tag{3.17}$$

In the wire model follows

$$\frac{\Phi}{l\mu_0} = \int_a^b H\mathrm{d}r = \int_a^b \frac{I}{2\pi r}\mathrm{d}r = \frac{I}{2\pi}\ln\left(\frac{b}{a}\right). \tag{3.18}$$

Combining Eqs. (3.17) and (3.18) results in the effective conductor diameter of the FDTD thin wire in the wire model of

$$a = b\exp\left(-\frac{\pi}{2}\right). \tag{3.19}$$

A thin wire on the FDTD grid with grid length $b = g = 2\,\mathrm{mm}$ corresponds therefore to a conductor radius of $a \approx 0.42\,\mathrm{mm}$.

The radius b of the insulation in the wire model given by the implant under test usually does not match the grid length g in the FDTD model that is determined by the radius of the inner conductor. It is, however, possible to adjust the relative permittivity of the simulated insulation $\varepsilon_{r,\mathrm{sim}}$ so that the capacity per unit length C/l is equal for both models. For the FDTD model with assumed parallel plate capacitor with plate size gl and distance between the 4 plates in each direction follows

$$\frac{C}{l} = 4\varepsilon_0\varepsilon_{\mathrm{r,sim}}\frac{g}{g}. \tag{3.20}$$

For the wire model that is assumed to be a cylindrical capacitor with relative permittivity $\varepsilon_{r,\mathrm{cyl}}$ of the insulation follows

$$\frac{C}{l} = 2\pi\varepsilon_0\varepsilon_{\mathrm{r,cyl}}\frac{1}{\ln\left(\frac{b}{a}\right)}. \tag{3.21}$$

Combining Eqs. (3.20) and (3.21) results in

$$\varepsilon_{r,\mathrm{sim}} = \frac{\pi}{2}\frac{\varepsilon_{r,\mathrm{cyl}}}{\ln\left(\frac{b}{a}\right)}. \tag{3.22}$$

An implant lead with insulation radius $b = 1\,\mathrm{mm}$, conductor radius $a = 0.42\,\mathrm{mm}$ and insulation permittivity $\varepsilon_{r,\mathrm{cyl}} = 3$ could therefore be approximated in the FDTD model with a simulated insulation permittivity of $\varepsilon_{\mathrm{r,sim}} \approx 5.4$ and grid length $g = 2\,\mathrm{mm}$.

Simulation-based verification of straight implant simplification

The above mentioned implant lead simplification was compared to a high resolution simulation for verification purposes. The respective simulation setups consist of an insulated cable (inner conductor: PEC, 300 mm length, 10 mm uninsulated tip) that was put into a polyvinylpyrrolidone (PVP)/water phantom (size: $400\,\mathrm{mm} \times 60\,\mathrm{mm} \times 60\,\mathrm{mm}$, $\sigma = 0.6\,\mathrm{S\,m^{-1}}$, $\varepsilon_\mathrm{r} = 50$), see Fig. 3.10. A PEC wire parallel to the implant in 54 mm distance with source in the centre is responsible for excitation. A $400\,\mathrm{mm} \times 60\,\mathrm{mm}$ PEC shield was added in 6 mm distance to the source on the opposite side of the phantom.

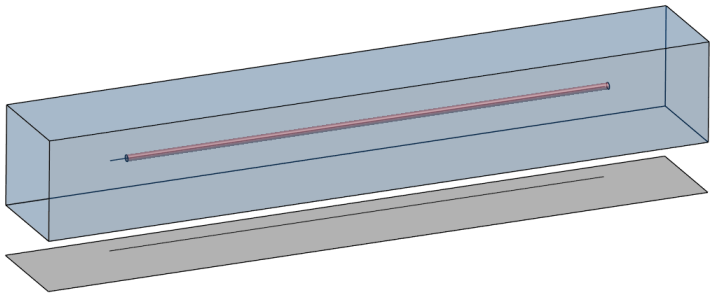

Fig. 3.10: Simulation setup with the simplified implant model. The implant lead with uninsulated tip (orange) is in a phantom (blue). A PEC wire with its source in the centre (black) is used with a shield (gray) for excitation.

Two types of electromagnetic FDTD simulations were carried out:

1. **full implant lead simulation**: A lead with $b = 1\,\mathrm{mm}$ insulation radius, $\varepsilon_\mathrm{r} = 3$ and $a = 0.42\,\mathrm{mm}$ inner conductor radius was used.

a) **high resolution**: The model was meshed using an adaptive grid with smallest grid length of 0.1 mm resulting in $86 \times 91 \times 351 \approx 2.7 \times 10^6$ voxels and a total simulation calculation time of $t_c \approx 18\,\mathrm{min}$.

b) **higher resolution**: The model was meshed using an adaptive grid with smallest grid length of 0.01 mm resulting in $290 \times 295 \times 659 \approx 56.4 \times 10^6$ voxels and a total simulation calculation time of $t_c \approx 13\,\mathrm{h}$.

2. **simplified implant lead model**: A lead with $b = 2\,\mathrm{mm}$ insulation thickness, $\varepsilon_r = 5.4$ (simulation 2a) respective $\varepsilon_r = 6$ (simulation 2b) and one-dimensional inner conductor was used. The model was meshed with a 2 mm isotrop grid resulting in $50 \times 65 \times 220 = 0.7 \times 10^6$ voxels and a total simulation calculation time of $t_c \approx 1\,\mathrm{min}$ each.

The electromagnetic total input power to the system was normalised to 1 W for all cases.

The SAR of the higher resolution simulation (1b) in the implant plane is presented in Fig. 3.11 as positional reference with marked SAR profiles that are shown in Fig. 3.12 for all 4 simulations. The reference SAR map shows the expected features with high SAR in vicinity of the uninsulated tip and lower SAR elsewhere.

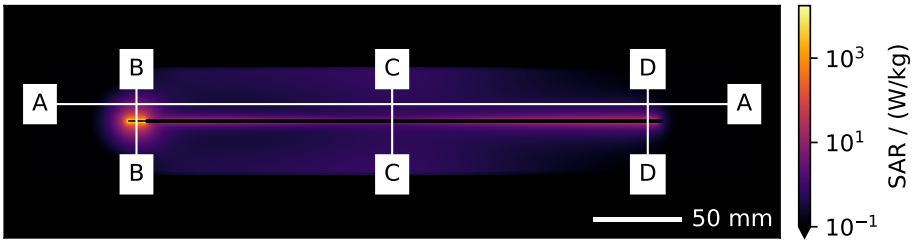

Fig. 3.11: SAR map of the higher resolution SAR simulation through the implant plane. The positions of the lineplots in Figs. 3.12 and 3.13 are marked in white. Please not the logarithmic scale.

The SAR profiles of the higher resolution simulation and the simplified model with the analytically derived $\varepsilon_r = 5.4$ using Eq. (3.22) agree well, see Fig. 3.12.

Major differences occur only in close vicinity to the implant, where the simplified model's grid length of 2 mm is not small enough to resolve the differences, see Fig. 3.13.

Small differences between the high resolution and the higher resolution simulation exist, see, for example, the SAR at position 0 in Fig. 3.12. These are caused by the 'coarse' smallest high resolution grid length of 0.1 mm

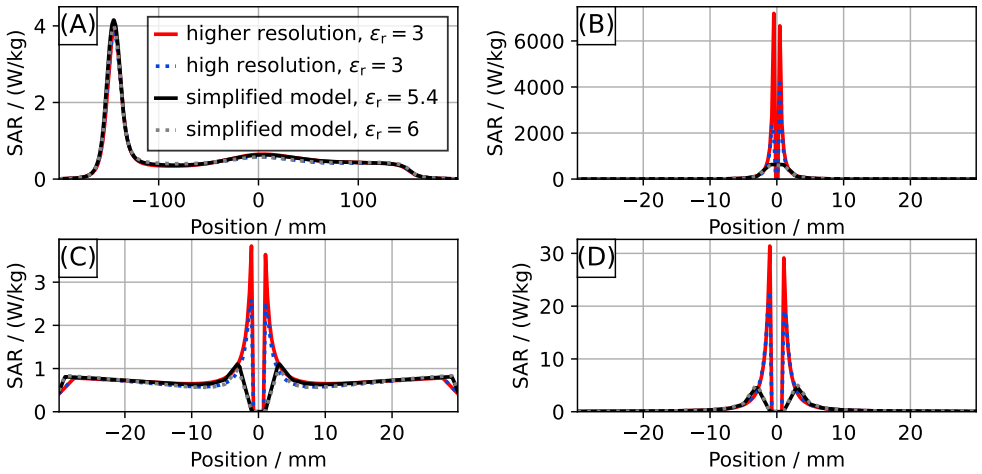

Fig. 3.12: Comparison of 2 full implant lead simulations (high resolution: 0.1 mm minimum grid length, higher resolution: 0.01 mm) and 2 simplified implant lead simulations with 2 mm grid length and adjusted ε_r. SAR as function of position of the profiles marked in Fig. 3.11.

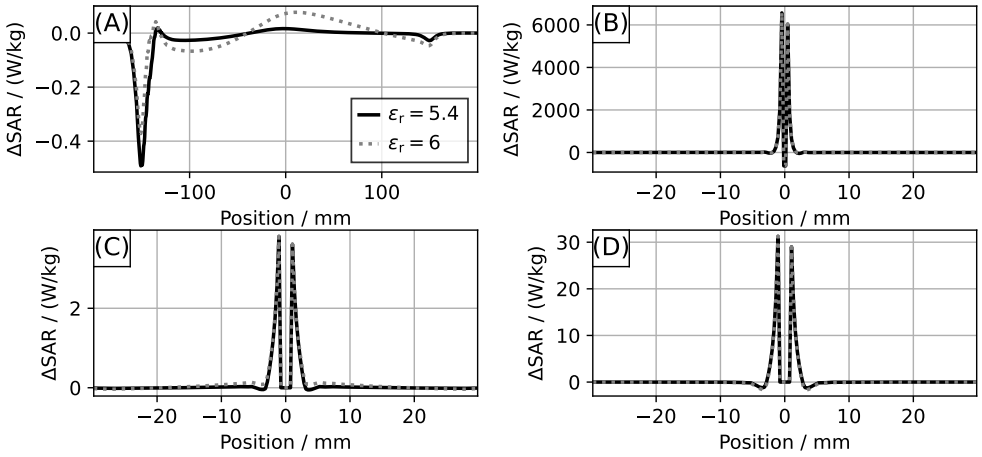

Fig. 3.13: Difference of SAR between higher resolution simulation and the simplified implant lead model simulations with $\varepsilon_r = 5.4$ and $\varepsilon_r = 6$ respectively at the profiles marked in Fig. 3.11.

that is not able to resolve the wire structure sufficiently. The high resolution SAR curves are approximated with the simplified implant lead simulation using $\varepsilon_r = 6$. The conductor radius of the high resolution simulation might therefore be approximated better with 0.46 mm according to Eq. (3.22) instead of the 0.42 mm that was set in modelling with difference of the radii of 0.04 mm under the high resolution grid length of 0.1 mm.

The biggest advantage of the simplified model are the reduced resource requirements with only $1.2\,\%$ of the voxels and $0.1\,\%$ of the necessary simulation calculation time t_c of the higher resolution model. The faster high resolution model was not able to resolve the wire properly, resulting in a minor SAR deviation.

Using such a simplified implant model is, in conclusion, possible for the special case of the implant being a straight line on the FDTD grid and results in the same SAR values as for a detailed simulation with reduced computational resources for distances above the grid length.

3.5 Thermal simulations

The IEC local SAR limits are not applicable for implants due to the implants' small volume of energy deposition that can result in high temperatures, even though the 10 g averaged limits are kept [35, 75].

It is therefore necessary to carry out thermal simulations in order to ensure implant safety, as temperature is directly correlated to tissue damage [47, 48, 127, 154] in contrast to SAR.

Thermal simulations were carried out in Sim4Life 5.0-7.0 using Pennes' bioheat equation [155, 156]

$$c\varrho\frac{\partial T}{\partial t} = k\nabla^2 T - h_\mathrm{b} + h_\mathrm{m} + h_\mathrm{RF} \tag{3.23}$$

$$h_\mathrm{b} = \varrho\omega\varrho_\mathrm{b}c_\mathrm{b}(T - T_\mathrm{b}) \tag{3.24}$$

where c is the specific heat capacity, ϱ is the mass density, k is the thermal conductivity and h is the rate of volumetric heat production respective transfer (unit: W m^{-3}) for blood (b), metabolism (m) and RF field (RF) where h_RF is equal to the volumetric absorption rate (VAR) [129]. The heat transfer rate to the blood h_b is dependent on the perfusion rate of the blood through the tissue ω (unit: m^3 s^{-1} kg^{-1}) as well as the blood's temperature T_b, mass density ϱ_b and specific heat capacity c_b.

The material properties of human tissue voxels (specific heat capacity c, mass density ϱ, thermal conductivity k, and metabolism heat production h_m) were extracted from the IT'IS Foundation's tissue properties database version 4.0 [62]. A thermal conductivity of 0.1 W m^{-1} K^{-1} was applied to the PVP/water[1] phantom according to [157].

[1] For reference: the thermal conductivity of water at 20 °C is 0.6 W m^{-1} K^{-1} [62].

Electric loss density maps

$$h_{\mathrm{RF}}(\boldsymbol{u}) = \frac{\sigma}{2}|\boldsymbol{E}(\boldsymbol{u})^2| \tag{3.25}$$

were calculated for the shim vectors under test $\boldsymbol{u}$ and used as heat source. The desired result of the thermal simulation was the steady state temperature that was assumed to be reached after 1 h of simulated time. The maximum observed temperature change was below 3 mK min^{-1} for the implant case [35] at this time.

Thermal simulations were carried out for three purposes:

1. **Calibration of the implant sensor** so that the sensor signal can be correlated against implant-caused temperature rise at the hazard spot of the implant tip. This requires many simulations to estimate the uncertainty. Simulations of a whole human voxel model are, however, time consuming and require a simulation run time around 1 d on an Intel Xeon Silver 4108 CPU. This run time was decreased by limiting the thermal simulation to the critical implant tip region. This region is, in this work, defined as the box around the implant tip, in which normalised SAR values above 1 can be found for RF-shim vectors, that are safe for the native case, with an additional safety margin of 30 mm in all directions. It was shown that the steady state temperature differences between partial simulation and full simulation in the ROI are below 20 mK, see Fig. 3.14.

2. **Verification of RF-shim vector safety.** A full body simulation was feasible due to the small number of RF-shim vectors.

3. **Investigation of implant hot spots.** An implant was simulated in a phantom to correlate the simulated temperature evolution against measurements. The methodology is described at the respective section for a better reading continuity.

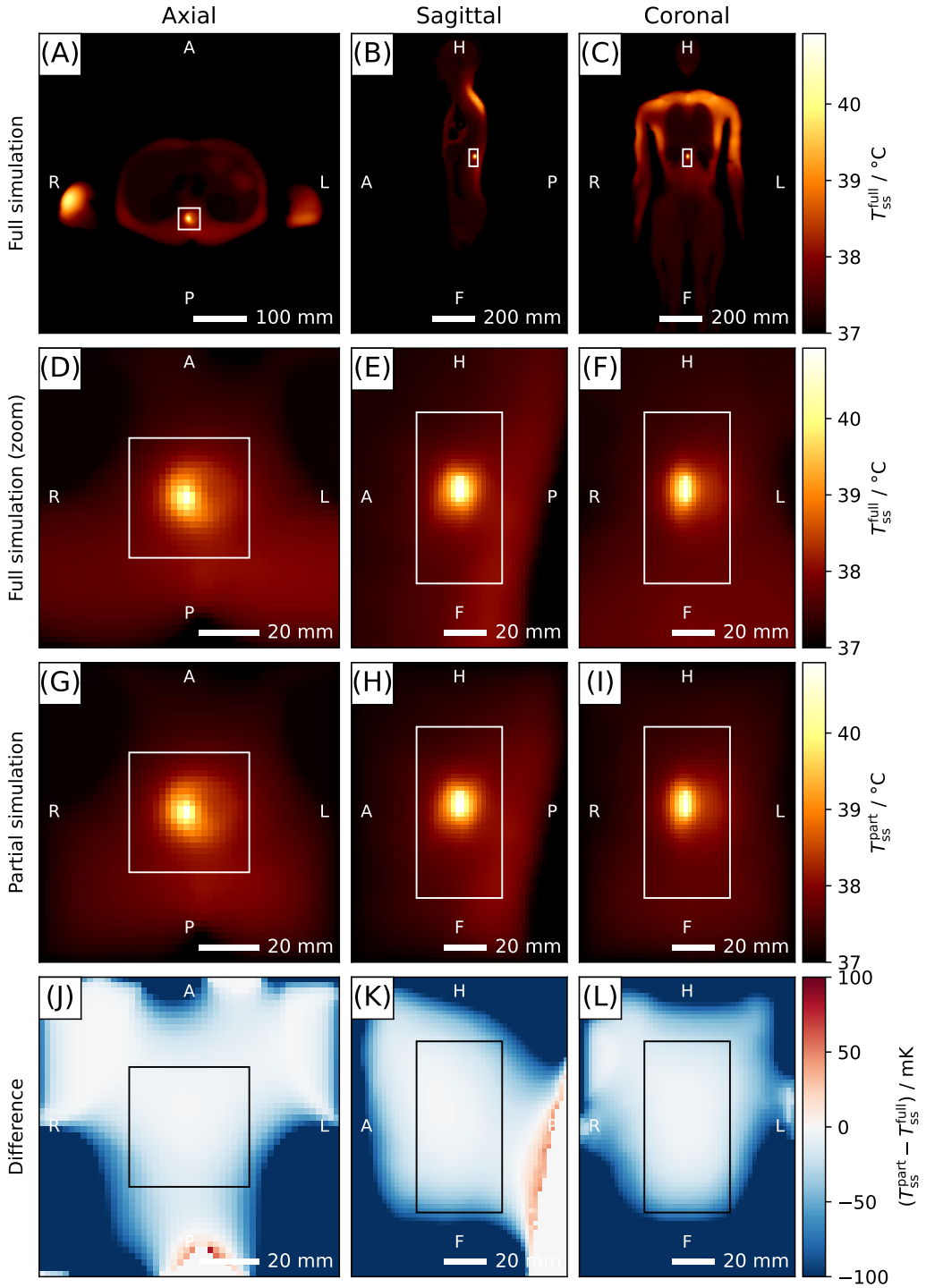

Fig. 3.14: Steady-state temperature maps for a full (**A-F**) and a partial (**G-I**) thermal simulation of human body model Duke with ROI (rectangle in white respective black) centred on an implant tip. The difference in the ROI (**J-L**) is minor. This figure by Petzold et al. [35] is licenced under CC BY 4.0.

4 Native RF SAR safety in pTx MR

This chapter investigates pTx safety with the IEC limits [45] for the native case, where no implant is present. The aim is to examine (i) if a higher $\mathrm{mean}(B_1^+)$ can be achieved with pTx compared to a single channel CP mode and (ii) whether the introduced complexity, by measuring the channels' phases for SCM, results in higher available $\mathrm{mean}(B_1^+)$ or whether PASCM and PCM that disregard phase information are sufficient if an appropriate safety factor is considered for all three limits.

Native safety is assured by combining the limits of multiple simulations with a safety factor [80]. Previous studies at $B_0 > 7\,\mathrm{T}$ with dedicated coils and SCM investigated patient movement [79, 158, 159], and patient model changes for head imaging [77, 160, 161], prostate imaging [58, 59] or scans of neonates [162].

This work expands this approach to the clinical field strength regime of 0.5 – 3 T. In doing so, more generally valid results can be obtained, since one ubiquitous transmit coil design exists at these lower field strengths: the cylindrical body coil [143–145]. A significant expansion of that previous work lies also in the comparison of different channel counts, as this aspect has previously mostly been investigated with respect to performance in coil design studies [163, 164], while its impact on the simulation uncertainties has not yet been addressed. Conceptually new is the comparison of the three safety limits SCM, PASCM and PCM.

Parts of this chapter were published in a journal paper [91] and two conference abstracts [76, 78].

4.1 Achievable mean B_1^+ with the three safety limits for a single configuration

The final achievable $\mathrm{mean}(B_1^+)$ for all safety limits is influenced by two criteria:

The initial conservativeness of the respective limit is caused by the neglect of information. The phase-agnostic limits PASCM and PCM must ensure that a given RF-shim vector is safe, even if the phase of each

channel is not known. The worst case phase configuration must therefore be assumed and all other phase configurations are equally affected. PCM likewise must assume that all channels have the same amplitude even though this is only the case for phase-shimming. It is therefore expected that all safety limits are ranked in terms of achievable $\mathrm{mean}(B_1^+)$ by SCM > PASCM > PCM if no safety factor is applied.

The applied safety factor is necessary to accommodate for unknown patient models, uncertain positions or unclear patient configurations (e.g. posture, breathing state).

This section investigates the initial conservativeness of all safety limits with the representative example of model Duke at 3 T and 8 channels in order to assess the $\mathrm{mean}(B_1^+)$ performance if full system information would be available. The trade-off between $\mathrm{mean}(B_1^+)$ and $\mathrm{CV}(B_1^+)$ was therefore optimised, see Fig. 4.1.

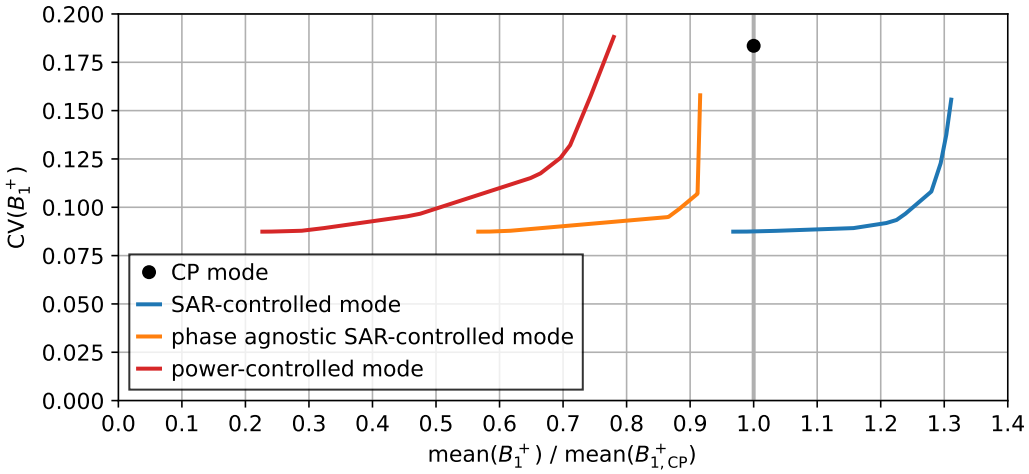

Fig. 4.1: Trade-off between optimised $\mathrm{mean}(B_1^+)$ and $\mathrm{CV}(B_1^+)$ of all three safety limits SCM, PASCM and PCM for model Duke at 3 T and 8 channels in cardiac imaging position.

The pTx B_1^+-inhomogeneity as measured by $\mathrm{CV}(B_1^+)$ is up to 50 % lower compared to the CP-mode. SCM results in 30 % higher $\mathrm{mean}(B_1^+)$ compared to the CP mode, while PASCM and PCM result in 10 % and 20 % decreased $\mathrm{mean}(B_1^+)$, respectively, confirming the expectation.

SCM's achievable $\mathrm{mean}(B_1^+)$ is higher than the CP mode, because the CP mode RF-shim vector is a part of all allowed SCM vectors while its single channel amplitudes are too high for both PASCM and PCM due to the neglect of phase information in the worst-case SAR estimation in both limits.

4.2 Anchor-Target analysis

This section describes a method to obtain a safety factor to compensate for model- and position-uncertainties in RF-safety assessment for MR exams with a limited amount of simulations.

An approach similar to the common separation of data into training-data (here called 'anchor') and test-data (here called 'target') in machine learning was adopted to extract the most information from the available configurations.

Multiple RF-shim vectors are thereby scaled to fully exploit the local SAR and head SAR of the anchor simulations[1] and a safety factor is subsequently derived from the highest local SAR violation caused by the scaled RF-shim vectors in the target simulation.

4.2.1 Underlying safety philosophy

The aim of the anchor-target analysis is the derivation of a reliable safety limit from finite simulation data, like a restricted number of human models, positions or postures in a given RF coil.

The limited number of simulations can be caused simply by the unavailability of digital human models or the computational burden to simulate more positions. It must also be taken care to avoid results with arbitrary precision that are not relevant in reality. If breathing changes the local SAR of a patient by more than 10 % [71], then there is little need to invest computational resources to derive a safety limit that is predicting the local SAR with error below 0.1 %.

It is not meaningful to define a global safety limit that considers all possible patient configurations in a given RF body coil at the same time. A larger-bodied patient having a cardiac exam and a neonate having a brain exam will require different limits in order to achieve safety and maximum possible RF performance in both cases.

'Easily accessible' measurements for each MR exam should therefore be used in order to tailor the derived limit closer to the explicit patient configuration by basing the limit on 'close' configurations only. Such easily obtainable values contain for example patient weight, patient height, the position of the patient in the MR scanner and the measured whole-body SAR for the current RF-shim vector. 'Close' means in this case, that the current patient

[1] The whole-body SAR and partial-body SAR limits of the *target* are monitored, too, because these values are in principle measurable. The associated whole-body and partial-body limits were, however, not restricting except for vastly different models, see Section A.4.

configuration should reasonably match the configurations that were used to derive the safety limit. Coming back to the previous example, this would result in a group of neonates undergoing brain MRI and a group of humans with weight of 120 – 160 kg in the cardiac imaging position.

It should be reasonable to expect that the generated safety limit covers additional, completely unknown patients within the given patient group. This has to be ensured with an appropriate safety factor that covers the model variability. The choice of the safety factor is essential to ensure safety and high RF performance. A too high safety factor is conservative, but limits performance more than necessary while a too low safety factor can result in damage for the patient. This work is therefore aiming at the lowest possible safety factor that still ensures safety for all investigated models, if the most susceptible model would be unknown.

4.2.2 Procedure

The anchor-target analysis consists of the following steps, see an illustration with anchor models Yoon-sun and Glenn and target model Louis in Fig. 4.2.

1. One target configuration and at least one anchor configuration are selected from a group of compatible configurations that have the same B_0-field strength and channel count N_c.

2. A random shim vector $\boldsymbol{u}_r$ is scaled with a scalar a to hit the local SAR and head SAR limit of the most restrictive anchor simulation.

   a) For SCM, this corresponds to the highest normalised SAR over all Q-matrices of the anchor simulations being one, see Eq. (2.20):

   $$\max_m \boldsymbol{u}_{\mathrm{SCM}}^{\dagger} \hat{\boldsymbol{Q}}^{(m)} \boldsymbol{u}_{\mathrm{SCM},r} = 1, \quad \boldsymbol{u}_{\mathrm{SCM},r} = a_{\mathrm{SCM},r} \boldsymbol{u}_r. \tag{4.1}$$

   b) For PASCM, this corresponds to the highest normalised SAR over all Q-matrices of the anchor simulations where the phase is neglected to being one, see Eq. (2.21):

   $$\max_m |\boldsymbol{u}_{\mathrm{PASCM}}|^{\dagger} \left|\hat{\boldsymbol{Q}}^{(m)}\right| |\boldsymbol{u}_{\mathrm{PASCM},r}| = 1, \quad \boldsymbol{u}_{\mathrm{PASCM},r} = a_{\mathrm{PASCM},r} \boldsymbol{u}_r \tag{4.2}$$

   where $|\cdot|$ denotes the element-wise absolute value for the shim vector $|\boldsymbol{u}|_k = |\boldsymbol{u}_k|$ and the Q-matrix $\left|\hat{\boldsymbol{Q}}\right|_{k,n} = \left|\hat{\boldsymbol{Q}}_{k,n}\right|$.

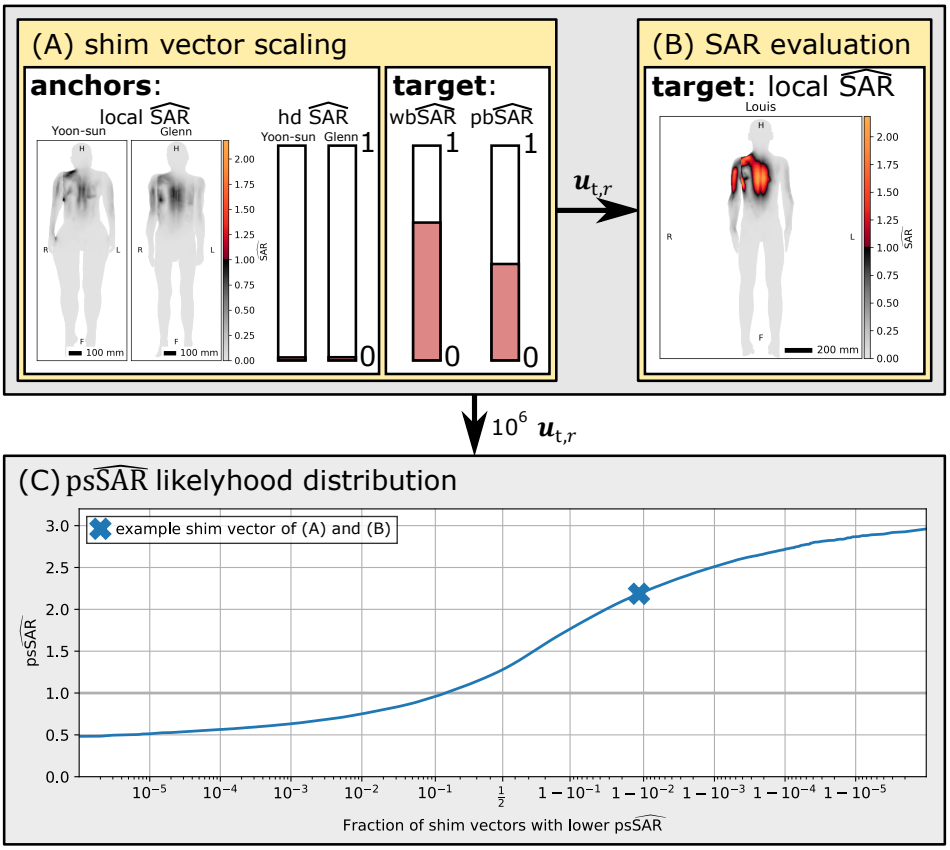

Fig. 4.2: Workflow of the anchor-target analysis, demonstrated with models Yoon-sun and Glenn as anchors and Louis as target at 8 channels and 3 T for SCM. (**A**) A random RF-shim vector is scaled by a scalar to hit the strictest of the anchor's local SAR and head SAR limits and target's whole-body and partial-body SAR limits. Maximum intensity projections of local SAR are shown for Yoon-sun and Glenn. (**B**) Applying this scaled vector $\boldsymbol{u}_{\mathrm{t},r}$ to the target simulation can result in $\mathrm{ps}\widehat{\mathrm{SAR}} > 1$. (**C**) Repeating this process 10^6 times results in a $\mathrm{ps}\widehat{\mathrm{SAR}}$ distribution over all tested shim vectors. The maximum $\mathrm{ps}\widehat{\mathrm{SAR}}$ of all shim vectors can then be used as safety factor. This figure by Petzold et al. [91] is licenced under CC BY 4.0.

c) For PCM, this corresponds to setting the highest single channel amplitude of $\boldsymbol{u}_{\mathrm{r}}$ to the lowest single channel amplitude limit $\alpha(a)$ of all anchor simulations a, see Eq. (2.23):

$$\max_c |\boldsymbol{u}^{(c)}_{\mathrm{PCM},r}| = \min_a \alpha(a), \qquad \boldsymbol{u}_{\mathrm{PCM},r} = a_{\mathrm{PCM},r}\boldsymbol{u}_r. \tag{4.3}$$

These scaled RF-shim vectors $\boldsymbol{u}_{\mathrm{s},r} = \boldsymbol{u}_{\mathrm{SCM/PASCM/PCM}}$ are by construction safe for the local SAR and head SAR for all anchor simulations.

3. The normalised whole-body of the target simulation is evaluated for each $\boldsymbol{u}_{\mathrm{s},r}$

$$\mathrm{wbSAR} = \boldsymbol{u}_{\mathrm{s},r}^{\dagger} \hat{\boldsymbol{Q}}_{\mathrm{wb}} \boldsymbol{u}_{\mathrm{s},r}. \tag{4.4}$$

The shim vector is subsequently scaled by $1/\sqrt{\mathrm{wbSAR}}$ if the whole-body SAR is violated, i.e. if $\mathrm{wbSAR} > 1$

$$\boldsymbol{u}_{\mathrm{t},r} = \begin{cases} \frac{1}{\sqrt{\mathrm{wbSAR}}} \boldsymbol{u}_{\mathrm{s},r} & \text{for } \mathrm{wbSAR} > 1 \\ \boldsymbol{u}_{\mathrm{s},r} & \text{for } \mathrm{wbSAR} \leq 1 \end{cases}. \tag{4.5}$$

The same process happened analogously for partial body SAR. Please note that always local SAR was the limiting factor and never whole-body SAR, unless anchor and target models were vastly different in body mass, see appendix A.4.

The resulting shim vectors $\boldsymbol{u}_{\mathrm{t},r}$ are therefore safe for the anchors and fulfil the whole-body and partial-body SAR limits of the target. They can, however, have local SAR overshoots in the target simulation. Overshoot o in context of this thesis is thereby the difference between a measure and its limit, for example $o = \mathrm{ps}\widehat{\mathrm{SAR}} - 1$.

4. The maximum $\mathrm{ps}\widehat{\mathrm{SAR}}$ of the target simulation's l Q-matrices

$$\mathrm{ps}\widehat{\mathrm{SAR}}(\boldsymbol{u}_{\mathrm{t},r}) = \max_{l} \boldsymbol{u}_{\mathrm{t},r}^{\dagger} \hat{\boldsymbol{Q}}^{(l)} \boldsymbol{u}_{\mathrm{t},r} \tag{4.6}$$

is subsequently used as safety measure.

5. Repeating steps 2 - 4 for 10^6 random RF-shim vectors (half with random phases and identical amplitude, half with both random phases and random amplitudes) results in a distribution of possible $\mathrm{ps}\widehat{\mathrm{SAR}}$ values and their likelihood.

6. The maximum $\mathrm{ps}\widehat{\mathrm{SAR}}$ of all random shim vectors $\boldsymbol{u}_{\mathrm{r}}$ is used as raw safety factor s' with

$$s' = \max_{r} \mathrm{ps}\widehat{\mathrm{SAR}}(\boldsymbol{u}_{\mathrm{t},r}) \tag{4.7}$$

for all safety limits. A raw safety factor $s' \leq 1$ is achieved for configurations where the target simulation was always safe if the local and head SAR limits for the anchor simulations and the whole-body and partial-body SAR limits of the target simulation were fulfilled. It is desired to

apply the safety factor to the respective limit to derive an overarching safety limit considering the observed uncertainties. A $s' < 1$ would, in this case, result in SAR-overshoots for at least one anchor simulation and is therefore not allowed. The adjusted safety factor s that is used in the following must hence be at least unity:

$$s = \max\{s', 1\}. \tag{4.8}$$

A maximum theoretical $\mathrm{ps}\widehat{\mathrm{SAR}}_{\mathrm{max}}$ can be calculated for PCM by Eq. (2.24) for the single channel amplitude limit $\alpha(a)$ of the anchor(s) a and $\alpha(t)$ of the target t with

$$\mathrm{ps}\widehat{\mathrm{SAR}}_{\mathrm{PCM,max}} = \left(\frac{\min_a \alpha(a)}{\alpha(t)}\right)^2, \tag{4.9}$$

that fulfils $\mathrm{ps}\widehat{\mathrm{SAR}}_{\mathrm{PCM,max}} \geq s' = \max_{\boldsymbol{u}_\mathrm{r}} \mathrm{ps}\widehat{\mathrm{SAR}}(\boldsymbol{u}_\mathrm{r})$ for all $\boldsymbol{u}$, see appendix A.2.

Such a mathematical upper limit is, to the author's knowledge, not existent for SCM and PASCM. It is furthermore not guaranteed that an optimisation with cost function

$$C(\boldsymbol{u}) = -\frac{\mathrm{ps}\widehat{\mathrm{SAR}}(\boldsymbol{u}, \mathrm{target})}{\mathrm{ps}\widehat{\mathrm{SAR}}(\boldsymbol{u}, \mathrm{anchor(s)})} = -\frac{\max_m \boldsymbol{u}^\dagger \hat{\boldsymbol{Q}}^{(m)}_{\mathrm{target}} \boldsymbol{u}}{\max_l \boldsymbol{u}^\dagger \hat{\boldsymbol{Q}}^{(l)}_{\mathrm{anchor}} \boldsymbol{u}} \tag{4.10}$$

finds the global worst case $\mathrm{ps}\widehat{\mathrm{SAR}}$ because the optimisation problem is not convex. As such optimisation results in a high computational burden without giving the mathematical certainty of the guaranteed maximum, the random shim vector approach was chosen. This results in a much faster calculation for multiple combinations of anchor(s) and target trough precalculation of the $\mathrm{ps}\widehat{\mathrm{SAR}}$ values corresponding to the identical random shim vectors for each configuration.

The resulting $\mathrm{ps}\widehat{\mathrm{SAR}}$ distribution could also be used to assess the likelihood of a given SAR overshoot height. It is possible to assess the patient-safety with the $\mathrm{ps}\widehat{\mathrm{SAR}}$ of a given percentile instead of the maximum $\mathrm{ps}\widehat{\mathrm{SAR}}$ in order to trade better $\mathrm{mean}(B_1^+)$ performance against a minor safety risk. Such trade-off is, however, departing from the 'worst-case shall be safe' doctrine of this thesis and is therefore beyond the scope of this work.

4.3 Investigated uncertainties and resulting simulation groups

Four groups of simulations were defined to investigate different causes of uncertainties. The first three groups contain simulations of model Duke at various spatial positions relative to the cardiac imaging position at $x = y = z = 0$ that is shown in Fig. 3.5, see Fig. 4.3.

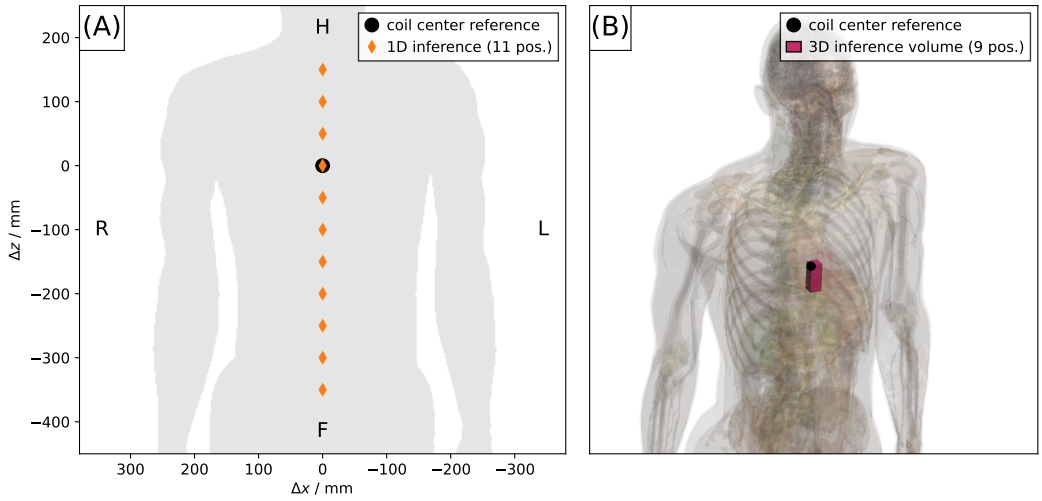

Fig. 4.3: Spatial positions of model Duke in anchor-target analysis runs. (**A**) 1D inference. (**B**) 3D inference. This figure by Petzold et al. [91] is licenced under CC BY 4.0.

1. **small z-shift**: The steps with the highest computational burden in the whole workflow are the primary simulation and the compression of the Q-matrices into VOPs. VOP compression [80] is necessary for SCM and PASCM and shows an exponential increase of computational load for decreasing SAR overestimations [133, 153]. Arbitrary precision in VOP calculation should therefore be avoided to save resources. This group compares simulations with 'negligible' z-shifts of 1 mm and 2 mm at z-positions −6 mm, −5 mm and −4 mm (3 positions) to estimate a sufficient SAR overestimation for VOP compression. Negligible means in this context that it is expected to be impractical to position a patient within the scanner with a higher accuracy.

2. **1D inference**: Scan positions of patients in a closed bore MR scanner vary mainly by their z-position as a consequence of the scanner's geometry. z-positions from $z = -350\,\mathrm{mm}$ to $z = 150\,\mathrm{mm}$ in steps of 50 mm

(11 positions) are analysed to investigate the suitability of unilateral and bilateral inference, see Fig. 4.3A.

3. **3D inference**: The patient position in the MR scanner can be measured. It is investigated how the safety factor and $\mathrm{mean}(B_1^+)$ performance is influenced by a 3D inference between the 8 corners of a rectangular cuboid located between −20 mm and 0 mm for x and y, and −50 mm and 0 mm for z as anchor and the centre point of the cuboid as target, see Fig. 4.3B. Only 3 T was investigated for this case.

A fourth group contains the 11 human voxel models, see Fig. 3.5.

4. **model dependency**: 11 human voxel models based on 10 different humans were analysed in cardiac imaging position, where the centre of the heart is located in the central z-plane of the coil. Only the 7 models between 50 kg and 80 kg are used for the anchor-target analysis to avoid artefacts caused by huge model size differences. See appendix A.4 for an analysis with all 11 models.

4.4 Investigation of numerical uncertainty (small z-shift)

This section investigates the uncertainty arising from minor changes in the FDTD simulation in order to establish a VOP overestimation that is not resulting in information loss while saving computational resources.

Model Duke was therefore simulated at 3 z-positions (−6 mm, −5 mm and −4 mm) with minor steps of 1 mm and constant x- and y-position. The model in the middle position at −5 mm was meshed differently compared to the outer positions, because meshing happened with an isotrop grid with 2 mm resolution that was aligned to the coil.

The anchor-target analysis was carried out for all 6 possibilities of 1 anchor and 1 target simulation (4 runs with 1 mm z-shift, 2 runs with 2 mm z-shift). The maximum VOP $\mathrm{ps}\widehat{\mathrm{SAR}}$ estimation for each channel configuration, field strength, z-shift and safety limit is shown in Fig. 4.4.

It was not possible to verify the $\mathrm{ps}\widehat{\mathrm{SAR}}$ that was calculated with the VOPs

$$\mathrm{ps}\widehat{\mathrm{SAR}}_{\mathrm{VOP}} = \frac{\max_j \boldsymbol{u}^\dagger \hat{\boldsymbol{Q}}^{(j)}_{\mathrm{VOP,target}} \boldsymbol{u}}{\max_k \boldsymbol{u}^\dagger \hat{\boldsymbol{Q}}^{(k)}_{\mathrm{VOP,anchor}} \boldsymbol{u}} \tag{4.11}$$

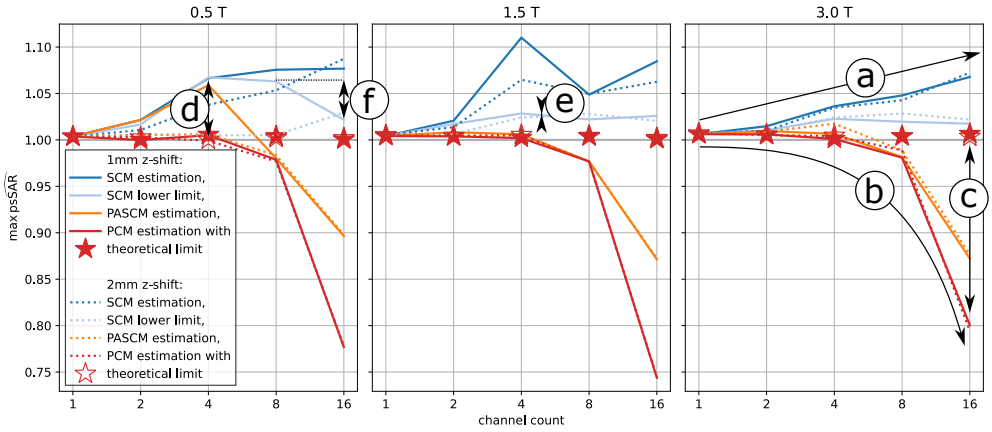

Fig. 4.4: Maximum $\widehat{\mathrm{psSAR}}$ in model Duke for an anchor-target analysis with z-shifts of 1 mm and 2 mm. Features (**a-f**) are explained in the text. This figure by Petzold et al. [91] is licenced under CC BY 4.0.

with the $\widehat{\mathrm{psSAR}}$ obtained from all normalised Q-matrices

$$\widehat{\mathrm{psSAR}}_{\mathrm{all}} = \frac{\max_l \boldsymbol{u}^\dagger \hat{\boldsymbol{Q}}^{(l)}_{\mathrm{all,target}} \boldsymbol{u}}{\max_m \boldsymbol{u}^\dagger \hat{\boldsymbol{Q}}^{(m)}_{\mathrm{all,anchor}} \boldsymbol{u}} \tag{4.12}$$

for the RF-shim vectors $\boldsymbol{u}$ that result in the highest $\widehat{\mathrm{psSAR}}_{\mathrm{VOP}}$ due to small errors introduced by the VOP compression, especially for small SAR values [165]. The VOP overestimation was set to the values of Tab. 4.1 to minimise the $\widehat{\mathrm{psSAR}}$ error while still maintaining a workable VOP calculation time. Lowering the 16 channel overestimation was not feasible due to the exponential increase in computational load [133, 153].

Tab. 4.1: VOP overestimations for the small z-shift analysis.

channel count	VOP overestimation / %
1	0
2	0.5
4	0.5
8	1
16	2

The VOP compression artefacts are investigated with a lower limit maximum $\widehat{\mathrm{psSAR}}$. The proof of existence of a realisation was carried out with two strategies:

1. **Lower limit with $\boldsymbol{B}^*$ core matrices**: The core matrices $\hat{\boldsymbol{B}}^{*(m)}_{\text{target}}$ are a subset of all normalised Q-matrices that is found with the original VOP compression algorithm [80] and acts as basis to derive the VOPs. The estimation of $\widehat{\text{psSAR}}_{\text{SCM,max}}$ happens with

$$\widehat{\text{psSAR}}_{\text{SCM,max}} \geq \frac{\max_m \boldsymbol{u}^\dagger \hat{\boldsymbol{B}}^{*(m)}_{\text{target}} \boldsymbol{u}}{\max_l \boldsymbol{u}^\dagger \hat{\boldsymbol{Q}}^{(l)}_{\text{VOP,anchor}} \boldsymbol{u}} \tag{4.13}$$

   where the core matrices are selected with 2 % overestimation [80]. The numerator of the fraction is always less or equal to the actual target $\widehat{\text{psSAR}}$ because the core matrices are a subset of all normalised Q-matrices. The denominator is greater or equal to the actual anchor $\widehat{\text{psSAR}}$ because of the VOP construction. A high number of 10^6 random shim vectors $\boldsymbol{u}$ was tested for this construction as the count of both core matrices and VOPs was below 1000.

2. **Lower limit with all Q-matrices**: The maximum $\widehat{\text{psSAR}}$ is estimated directly with all normalised Q-matrices $\hat{\boldsymbol{Q}}_{\text{all}}$ with

$$\widehat{\text{psSAR}}_{\text{SCM,max}} \geq \frac{\max_n \boldsymbol{u}^\dagger \hat{\boldsymbol{Q}}^{(n)}_{\text{all,target}} \boldsymbol{u}}{\max_p \boldsymbol{u}^\dagger \hat{\boldsymbol{Q}}^{(p)}_{\text{all,anchor}} \boldsymbol{u}}. \tag{4.14}$$

   Only the 1000 shim vectors with the highest $\widehat{\text{psSAR}}$ overestimation of the VOP estimation are used, as the number of Q-matrices $> 10^7$ results in a high computational load.

The theoretical upper limit $\widehat{\text{psSAR}}_{\text{PCM,max}}$ is additionally shown for PCM, see Eq. (4.9).

For SCM, there is a tendency for higher channel counts to result in higher overshoots that can be explained with the increased number of degrees of freedom (Fig. 4.4a). The opposite happens for PASCM and PCM where the overshoot tends to decrease with channel count (Fig. 4.4b).

The theoretical $\widehat{\text{psSAR}}$ overshoot for PCM was in all cases below 1 %. This overshoot was approximately realised with the scaled random RF-shim vectors for 1 to 4 channels independent of z-shift and B_0-field strength. The difference between realisation and theoretical maximum spreads for 8 channels to −3 % and for 16 channels to around −15 % (Fig. 4.4c).

For 0.5 T, there is a overestimation gap between 1 mm and 2 mm z-shift for both estimation and lower limit (Fig. 4.4d). Especially the lower limit of 2 mm z-shift stays near 1 % overshoot until 8 channels, while the 1 mm z-

shift lower limit overshoot is at 6 % for 4 and 8 channels. This indicates that the overshoot is mainly caused by different meshing and the small z-shift itself is negligible.

For 1.5 T and 3 T the difference between 1 mm and 2 mm z-shift vanishes. The z-shift-caused overshoot is therefore in the same order of magnitude as the meshing-caused overshoot (Fig. 4.4e).

As the 8 channel configuration is a subset of the 16 channel configuration, the 16 channel lower limit using all normalised Q-matrices cannot be lower than the 8 channel lower estimation (Fig. 4.4f). The dip of the 1 mm z-shift lower estimation can therefore be explained with the limited shim vector selection.

An example shim for a 2 mm shift with 4 channel at 3 T is shown in Fig. 4.5. The SAR limit is violated in a small region near the right shoulder with diameter below 30 mm. There is, however, an increase in SAR in the whole torso of up to 2.5 %.

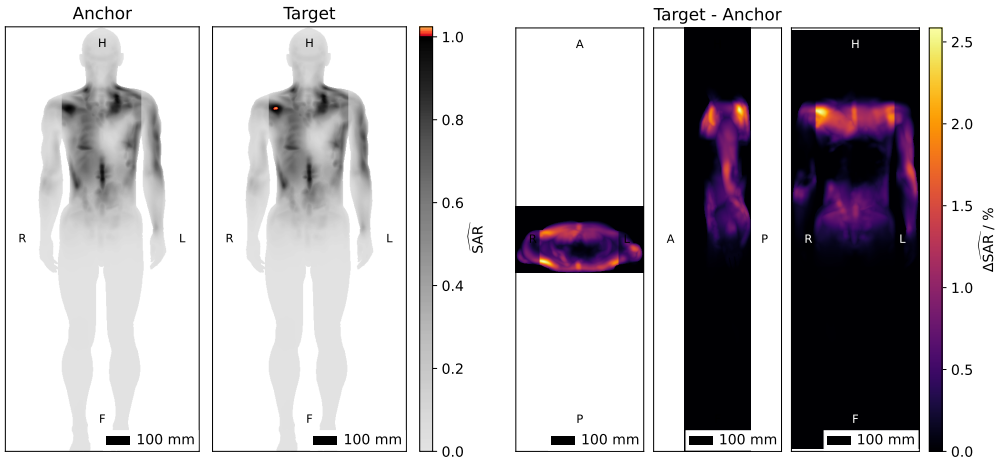

Fig. 4.5: Comparison of SAR of an anchor simulation and a by 2 mm in z-direction shifted target simulation for the same shim vector scaled to hit the limit of the anchor simulation. **Left:** Maximum intensity projection of SAR for anchor and target. **Right:** Maximum intensity projection of the SAR-difference between target and anchor simulation. Human voxel model Duke at 3 T and 4 channels. This figure by Petzold et al. [91] is licenced under CC BY 4.0.

The uncertainties of pTx are, in conclusion, higher than for a 1-channel CP mode system which is caused by more degrees of freedom. Uncertainties arise from shifted meshing and position shift itself and rise with channel count. PCM is the most conservative limit and shows only minor overshoots <1 % while confirmed PASCM and SCM overshoots can reach over 6 %. The uncertainty of the PCM mode can be reduced further by skipping the op-

tional VOP compression. The realisation gap for PCM, especially for 16 channels, shows that the tested 10^6 random RF-shim vectors are not enough to sufficiently scan the manifold of all possible RF-shim vectors. It was possible to find RF-shim vectors that reach >99.9 % by optimisation showing that the theoretical limit is indeed not arbitrarily large. It is expected that the tested RF-shim vectors are not sufficient for SCM and PASCM and the realisation gap becomes even larger, since one SCM vector tests only itself while a PCM vector tests a complete manifold of different phases and amplitudes.

A realised overshoot of 6 % for z-shifts of 1 mm and 2 mm is obviously still very minor and much larger overshoots will be present for bigger z-shifts, different human models, and especially when an implant gets involved. These overshoots, however, justify the use of a 2 % VOP compression overestimation of the worst case SAR for the following native simulations in order to use the available computational resources efficiently.

4.5 Uncertainties caused by unknown patient position

The position and orientation of a patient in a given posture in an MR scanner is described by six parameters: the three spatial coordinates and the three Euler angles. The parametrisation of a patient's posture requires the joint angles of each synovial joint and results in hundreds of degrees of freedom depending on the detail level. The human body model itself can be described with a nearly arbitrarily large amount of parameters starting from the 3D-shapes of each tissue to the tissues' material parameters. Uncertainties caused by a position-shift compared to a pre-calculated simulation are hence expected to be easier manageable by combining multiple anchor simulations than the uncertainties caused by a completely different model.

This section examines the uncertainties that arise from not knowing the exact patient position as first step before unknown patient models are investigated in a later section.

For this purpose, model Duke is investigated in a fixed posture aligned with the meshing grid to reduce the computational load. This reduces the degrees of freedom to the three spatial coordinates x, y and z. It is desired to carry out as few simulations as possible to obtain the most information possible of the the system 'human model in MR body coil'. The aim of the following subsections is therefore the approximation of a suitable simulation count and the respective human model positions.

4.5.1 Positions on the bore-axis

The most common position change in a closed bore scanner is the shift along the bore axis (here: z-axis) following its geometry. This subsection investigates model Duke in 14 positions: the 11 positions along the z-axis in steps of 50 mm and the 3 small z-shift positions, see Fig. 4.3. The analysis was carried out for all channel configurations, B_0-field strengths and safety limits.

It is desired to find the biggest position step Δz of two consecutive simulation positions that results in a sufficiently small safety factor in order to lower the computation load while also minimising performance loss caused by the safety factor.

Two methods to select anchor and target simulations were analysed for the anchor-target analysis:

Bilateral inference: Anchor simulations at $z + a$ **and** $z - a$ were used for the target at position z. 'The position is interpolated.'

Unilateral inference: Anchor simulations at **either** $z+a$ **or** $z-a$ were used for the target at position z. 'The position is extrapolated.'

The z-shift a corresponds thereby to the distance between measured patient position and available pre-calculated anchor position. It is assumed that a continuity of the $\mathrm{ps}\widehat{\mathrm{SAR}}$ exists for position shifts where a smaller distance a results in general in smaller changes of $\mathrm{ps}\widehat{\mathrm{SAR}}$. The z-shift of a represents therefore the worst-case patient position with the highest distance to the given pre-calculated anchor positions. Z-shift a is hence equal to using pre-calculated simulations with position step of $\Delta z = 2a$ to derive the appropriate safety limits.

The maximum $\mathrm{ps}\widehat{\mathrm{SAR}}$ for each z-shift a is shown in Figs. 4.6 and 4.7 as function of B_0-field strength and channel count.

The decrease in maximum $\mathrm{ps}\widehat{\mathrm{SAR}}$ for z-shifts above 200 mm is caused by the limited amount of available simulation combinations for higher z-shifts, because all 11 simulations (excluding the 3 small z-shift simulations) per field strength are spaced equally with steps of 50 mm. There are at the extreme of 500 mm z-shift only 2 possible variations of the available 2 simulations while there are 2×10 possibilities for 50 mm z-shift. This $\mathrm{ps}\widehat{\mathrm{SAR}}$ decrease is assumed to be an artefact and not a physical observation, as it is expected that a continuity exists where small z-shifts lead in general to smaller overestimations because of more similar Q-matrices.

Monotony of $\mathrm{ps}\widehat{\mathrm{SAR}}$ is hence enforced in Fig. 4.8. The 4 channel and 16 channel configurations are not shown for better readability.

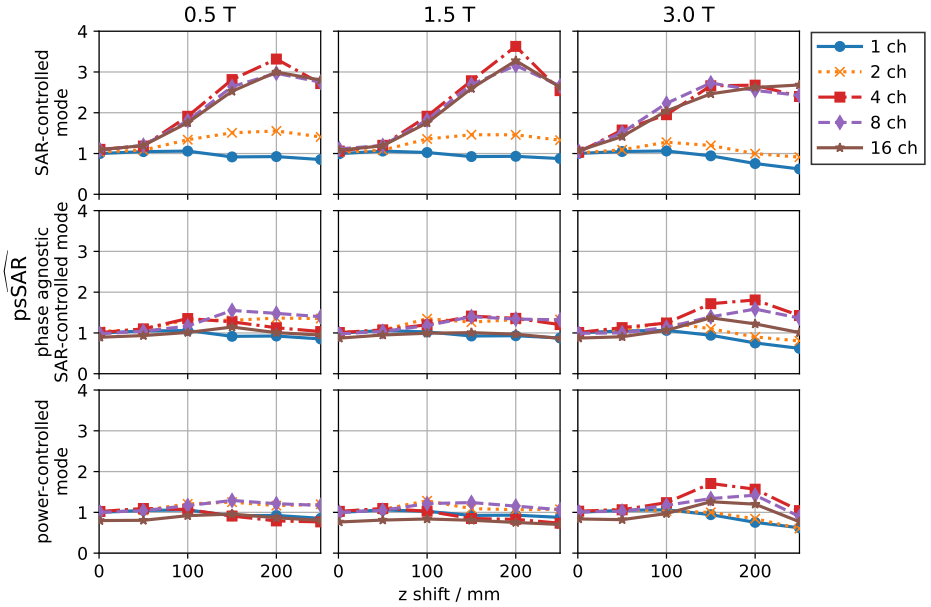

Fig. 4.6: Maximum $\widehat{\mathrm{psSAR}}$ as function of z-shift, channel count and B_0-field strength for bilateral inference.

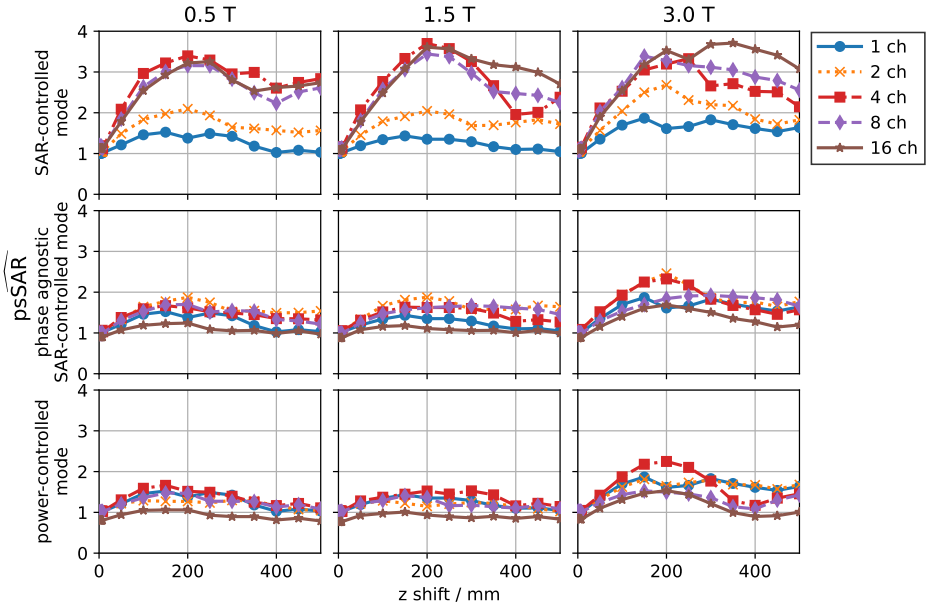

Fig. 4.7: Maximum $\widehat{\mathrm{psSAR}}$ as function of z-shift, channel count and B_0-field strength for unilateral inference.

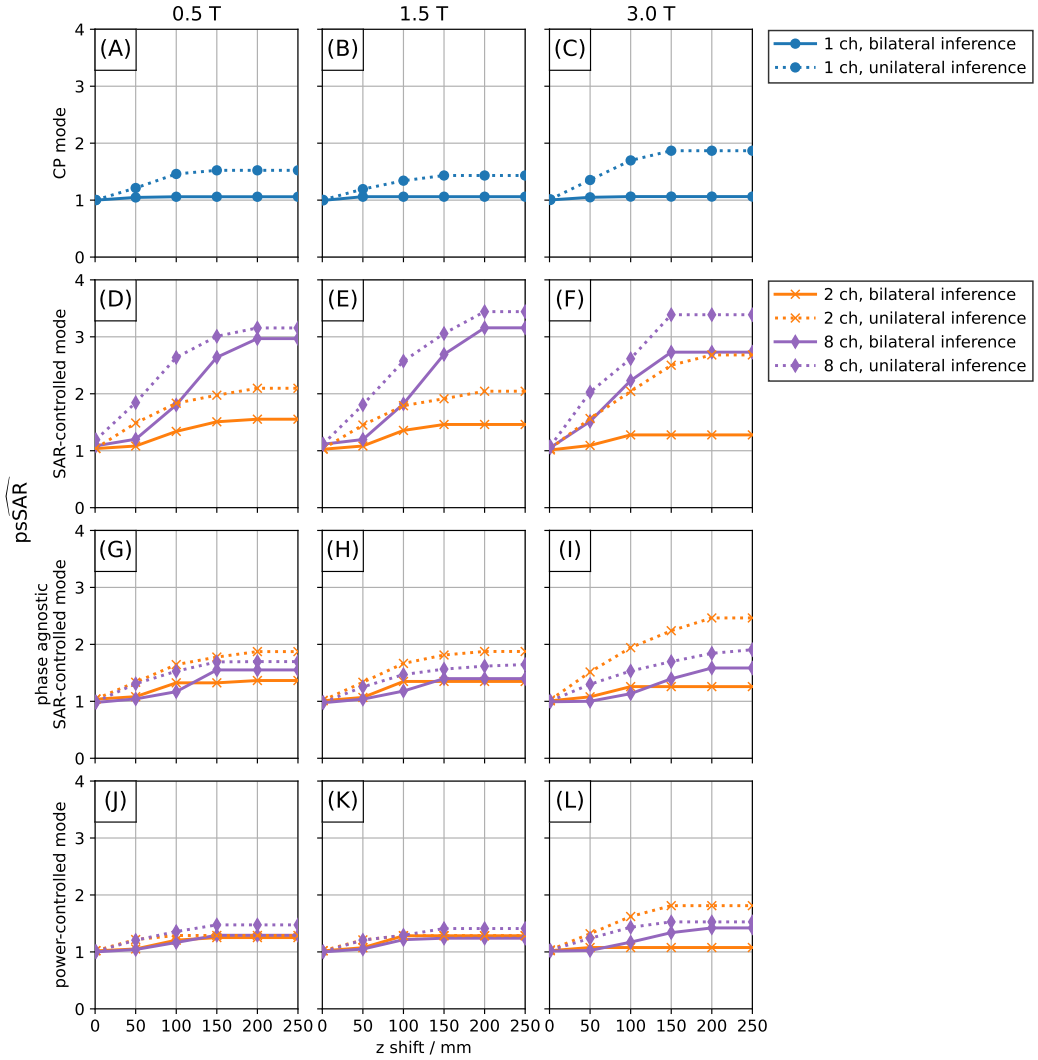

Fig. 4.8: Maximum $\widehat{\mathrm{psSAR}}$ for all z-shifts a' smaller than the maximum z-shift a ($\max_{a' \leq a} \widehat{\mathrm{psSAR}}(a')$) of all possible simulation combinations as function of channel count and B_0-field strength for bilateral and unilateral inference. This figure by Petzold et al. [91] is licenced under CC BY 4.0.

The 1 channel $\widehat{\mathrm{psSAR}}$ values are identical for all limits by construction, see Fig. 4.8A-C. The bilateral inference $\widehat{\mathrm{psSAR}}$ overshoot stays nearly constant and below 5 % for all z-shifts while the unilateral inference $\widehat{\mathrm{psSAR}}$ overshoot rises approximately linear to 40 – 90 % at $a = 150\,\mathrm{mm}$ depending on B_0.

The approximately linear relationship between $\widehat{\mathrm{psSAR}}$ and z-shift until $a = 150\,\mathrm{mm}$ for unilateral inference is present for all other safety limits and channel counts, too. Only minor differences occur between all field strengths for the same safety limit and channel count. The highest values are reached for SCM with around 3.4 for 3 T and 8 channels (panel F) while PASCM respective PCM stop at 2.5 (panel I) respective 1.8 (panel L) for 3 T and 2 channels. It is of particular note that 8 channels reach a higher $\widehat{\mathrm{psSAR}}$ than 2 channels for SCM in all cases, while this is switched for PASCM and little differences can be observed for PCM.

This observation matches with the behaviour of the small z-shifts, see Fig. 4.4a,b. The overestimation generally rises for SCM with channel count as more degrees of freedom are available, while the neglect of phases in the anchoring step for PASCM and PCM generally results in a higher conservativeness for more channels.

Bilateral inference between two positions leads to lower $\widehat{\mathrm{psSAR}}$ values than unilateral inference for all cases. Especially interesting is the z-shift were $\widehat{\mathrm{psSAR}}$ becomes nearly unity: An overshoot <20 % can be found for SCM for 0.5 T and 1.5 T and z-shift $a \leq 50\,\mathrm{mm}$ independent of channel count while a 60 % overshoot can be found for 3 T at 8 channels and z-shift $a \leq 50\,\mathrm{mm}$. The overshoot of PASCM and PCM are <5 % for all examined cases with z-shift $a \leq 50\,\mathrm{mm}$ and bilateral inference.

In conclusion, bilateral inference is, as expected, more conservative and results in lower necessary safety-factors. For PCM and PASCM, a simulation every $\Delta z = 100\,\mathrm{mm}$ is sufficient, independent of field strength and channel configuration, to achieve a low safety factor of 1.05. For SCM, a simulation every 100 mm is enough for 1.5 T, and 3 T with 2 channels, while a smaller distance between simulations would be necessary at 3 T for 4 channels and above to avoid a safety-factor of 1.6.

Unilateral inference is not recommended and results in high safety factors for SCM. PCM shows the highest conservativeness if unilateral inference cannot be avoided.

4.5.2 Inference in a cuboid

Slight patient position deviations below 20 mm perpendicular to the bore axis cannot be excluded. The possibility to infer the safety limit from the 8

corners of a cuboid as anchor for a target in the centre was hence examined to test whether it is possible to base the safety analysis of patient with known digital model on a limited number of anchor positions in a 3D grid.

Shifts perpendicular to the bore axis result in changes of the distance between patient and RF coil and are therefore expected to result in higher SAR changes. The size of the cuboid in x- and y-direction (20 mm) was chosen to be smaller than the size in z-direction (50 mm) to mitigate this effect. The centre point of the rectangular cuboid was selected as target position, because it has the highest spatial distance to all anchor simulations and therefore the highest expected difference of Q-matrices, and hence the highest worst case SAR potential.

The PCM single channel amplitude limits α were calculated for each simulation to obtain an overview over the proximity of all simulations, see Fig. 4.9 as representative example with the 8 channels.

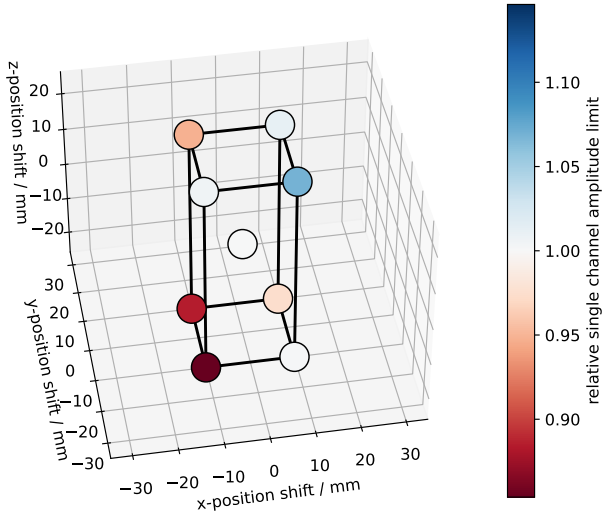

Fig. 4.9: Maximum single channel amplitude limit α relative to the central point of 9 simulations at the 8 corners and the central point of a rectangular cuboid. This figure by Petzold et al. [91] is licenced under CC BY 4.0.

The single channel amplitude limits α decrease in -x-, y- and -z-direction for all points except for the corner in -x,y,-z with the strongest gradient in -x direction. However, most important is the observation that the central point has a single channel amplitude limit α within the interval spanned by the corners' α. This allows the usage of the lowest α of the corners as conservative limit for the target simulation without an additional safety factor. It might even be possible to linearly interpolate between the corners for the included positions if appropriate caution is taken.

An anchor-target analysis with the corners' simulations as anchors and the centre point as target showed no need for a safety factor for any safety limit, see Fig. 4.10 as representative with 8 channels.

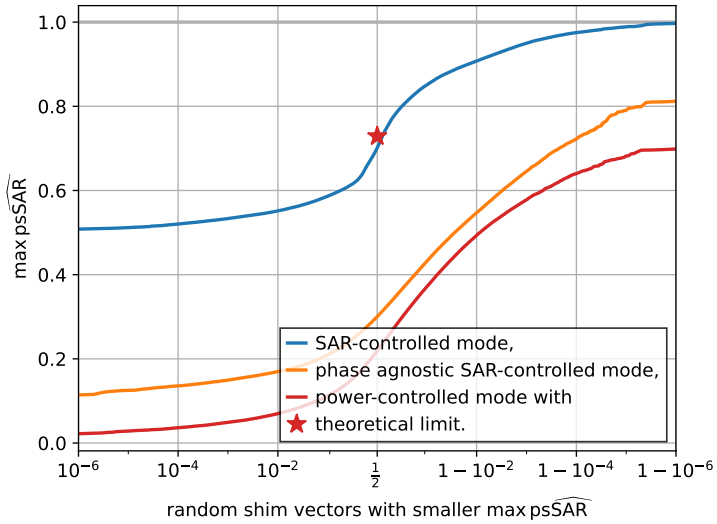

Fig. 4.10: Distribution of $\widehat{\mathrm{psSAR}}$ for an anchor-target analysis with the corners of a rectangular cuboid as anchor and the centre point as target with model Duke at 3 T and 8 channels. This figure by Petzold et al. [91] is licenced under CC BY 4.0.

The trade-off between optimised $\mathrm{mean}(B_1^+)$ and $\mathrm{CV}(B_1^+)$ in the target simulation using the anchors' combined safety limits is shown in Fig. 4.11. An additional optimisation was carried out for the 'position known' case, where SCM was used with the VOPs of the target simulation.

Applying 3D inference using the combined limits of all corners for the CP mode leads to a $\mathrm{mean}(B_1^+)$ decrease of 5 % compared to the known position's approach. This 3D inference drop is greater for the pTx shims with 10 % for SCM and nearly 50 % for PCM, both with same homogeneity as the CP mode.

While SCM shows an around 20 % higher $\mathrm{mean}(B_1^+)$ than the CP mode, PCM and PASCM results in a 30 % and 10 % drop of $\mathrm{mean}(B_1^+)$ compared to the CP mode, respectively. All safety limits perform best for 2 channels.

Conclusion

It is, due to limited resources, not feasible to simulate every digital human model at each possible spatial position with arbitrarily small resolution like 1 mm. Computational resources can be saved by simulation the available digital human models only on anchor positions and combining the limits of

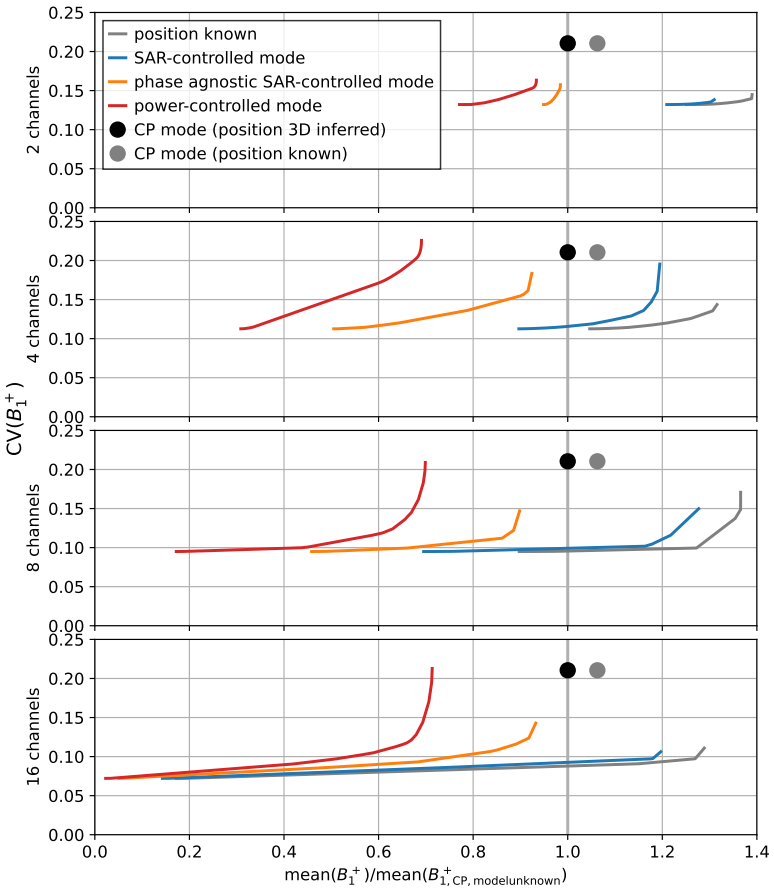

Fig. 4.11: Trade-off between optimised $\mathrm{CV}(B_1^+)$ and $\mathrm{mean}(B_1^+)$ for SCM, PASCM and PCM using the combined limits of all corners' simulations (red, orange and blue) and 'position known' using only the centre point's VOPs with SCM (grey).

the closest anchor positions with a safety factor to derive a safety limit for a new position. One possibility to establish such safety limits is the simulation of all valid positions on a rectangular grid and the usage of the closest corner points of the smallest rectangular cuboid encircling the requested position. The anchor grid should have a finer resolution in the axis perpendicular to the bore axis, as movements in this plane result in different distances between patient and RF coil (here: x- and y-direction). No additional safety factor is necessary for small enough resolutions (here: x, y: 20 mm, z: 50 mm at 3 T). $\mathrm{mean}(B_1^+)$ can however still be lowered by the additional constraints of the anchor simulations with an observed decrease of 5 % for the CP mode and 10 % for pTx.

4.6 Uncertainties caused by unknown patients

This section investigates the uncertainty of not knowing the exact patient model by examining the differences between known models.

4.6.1 Deriving a PCM limit from measurable parameters

For given exposure conditions (subject position, channel count, B_0), the PCM analysis results in a single scalar parameter for each investigated voxel model: the single-channel amplitude limit α. Sorting by α thus establishes a 'safety hierarchy' between different voxel models. This section examines whether it is possible to estimate α from easily measurable patient parameters in order to eliminate all model uncertainties and thus to achieve better $\mathrm{mean}(B_1^+)$ performance.

Patient mass $m = V_{\mathrm{voxel}} \sum_{\boldsymbol{r}} \varrho(\boldsymbol{r})$ with voxel volume $V_{\mathrm{voxel}} = (2\,\mathrm{mm})^3$, patient height h as largest z distance between the tissue containing voxels of the digital human model, and body mass index (BMI) as $\mathrm{BMI} = m/h^2$ were calculated for all 11 human voxel models μ in cardiac imaging position, see Fig. 3.5.

The single channel amplitude limits $\alpha(\mu, B_0, N_\mathrm{c})$ were calculated for all 11 models μ, 3 B_0-field strength 0.5 T, 1.5 T and 3 T and 5 channel counts N_c of 1, 2, 4, 8, and 16. The maximum permissible PCM power was calculated by $P(\mu, B_0, N_\mathrm{c}) \propto N_\mathrm{c}\,(\alpha(m, B_0, N_\mathrm{c}))^2$.

The normalised maximum permissible power

$$P_\mathrm{p}(\mu, B_0, N_\mathrm{c}) = \frac{P(\mu, B_0, N_\mathrm{c})}{\mathrm{mean}_{\mu,c}\, P(\mu, B_0, N_\mathrm{c})} \tag{4.15}$$

was calculated to eliminate channel dependency and plotted as boxplots as function of the patient parameters m, h and BMI for each B_0, respectively, see Fig. 4.12.

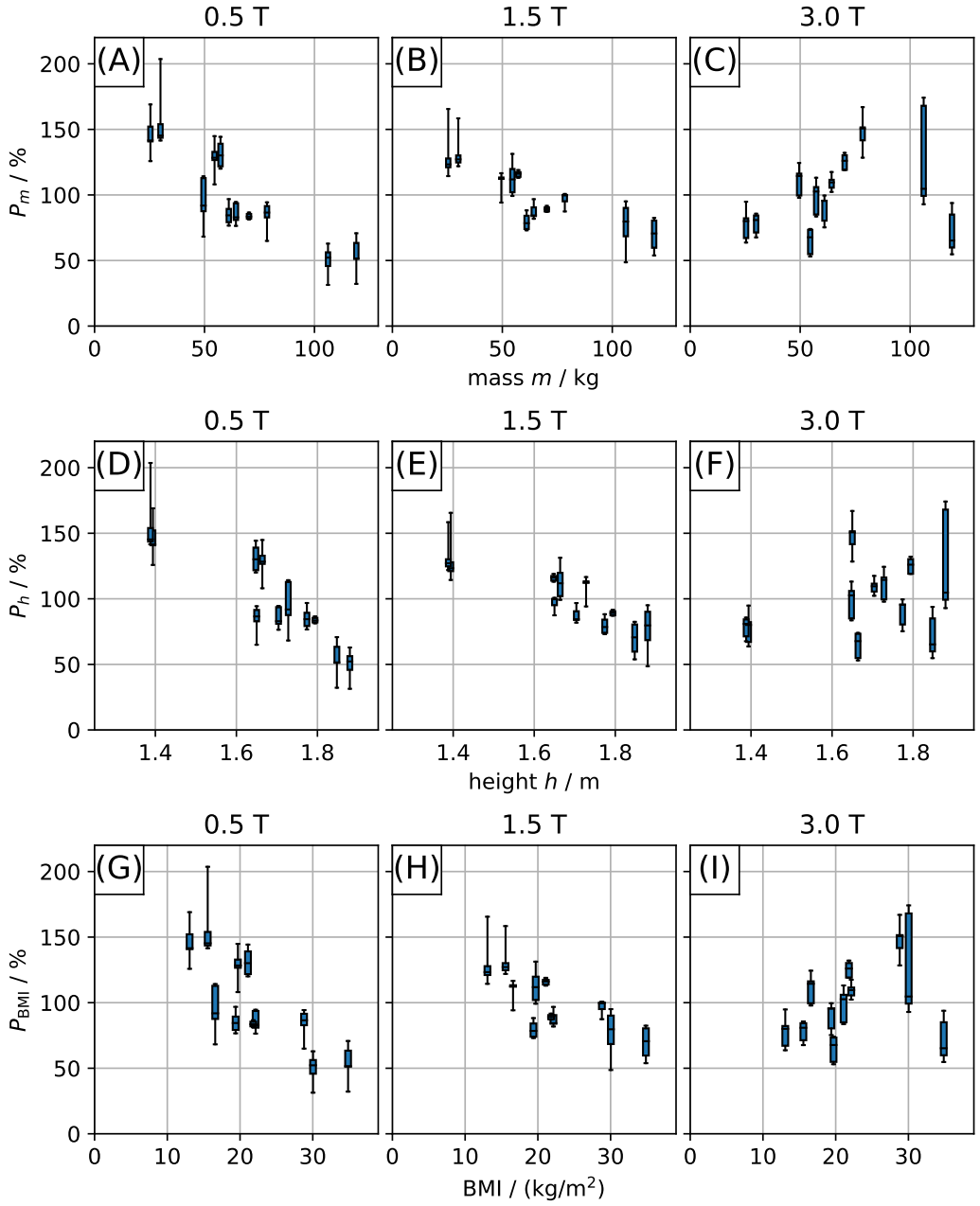

Fig. 4.12: Normalised maximum permissible power $P_\mathrm{p} \propto (\alpha(\mu, B_0, N_\mathrm{c}))^2$ as function of human voxel model mass m (**A-C**), height h (**D-F**) and BMI (**G-I**). Each box contains the values of all 5 channel configurations. This figure by Petzold et al. [91] is licenced under CC BY 4.0.

Linear trends can be observed for 0.5 T and 1.5 T: The normalised maximum allowed power decreases with higher mass and height. This holds true also for the BMI, albeit with larger error. No such trend is visible for 3 T.

The location of potential hotspots is analysed to investigate the difference between $B_0 \leq 1.5\,\mathrm{T}$ and $B_0 = 3\,\mathrm{T}$. The maximum achievable normalised SAR for the single channel amplitude limit of the whole-body Q-matrix is therefore calculated as the 1-norm of all normalised Q-matrices, see Section A.2.

The dominant potential hotspots for 0.5 T and 1.5 T are located at the sides of the torso, see blue arrows in Fig. 4.13.

It is not possible to examine mass-dependence, length-dependence and BMI dependence separately, because of the limited number of human models. A higher mass, higher length, respective higher BMI results in a higher patient volume and therefore closer proximity between the most relevant SAR hotspots at the sides of the torso and the RF coil, which in turn results in higher potential SAR and therefore lower SAR limits.

This behaviour cannot be observed for 3 T, especially for the height, where the correlation appeared strongest for 0.5 T and 1.5 T. A possible explanation is the shorter wavelength at 3 T (see Tab. 2.1) resulting in more hot spots that are also distributed over more areas of the torso, see blue arrows in Fig. 4.14.

It might therefore be possible to determine a safe single channel amplitude limit for PCM at $B_0 \leq 1.5\,\mathrm{T}$ by combining a patient's measured height with a RF-coil-specific calibration curve, while this appears to be not the case for 3 T.

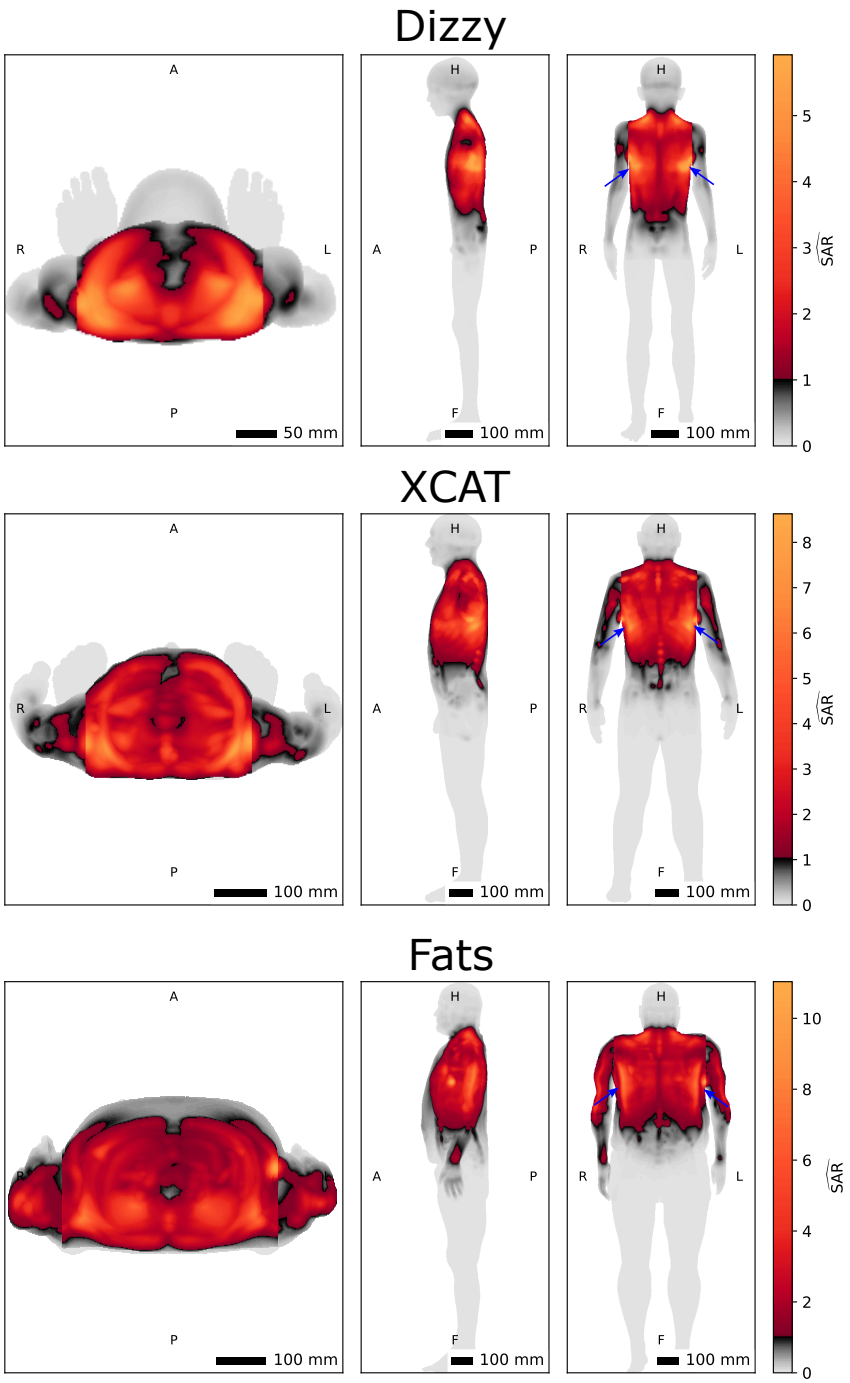

Fig. 4.13: Maximum achievable normalised SAR for models Dizzy (**top**, 25 kg), XCAT (**middle**, 78 kg) and Fats (**bottom**, 119 kg) at 16 channels and 0.5 T with PCM, when each single channel amplitude limit α is derived from the corresponding whole-body Q-matrix. Blue arrows point at regions with potential for high local SAR.

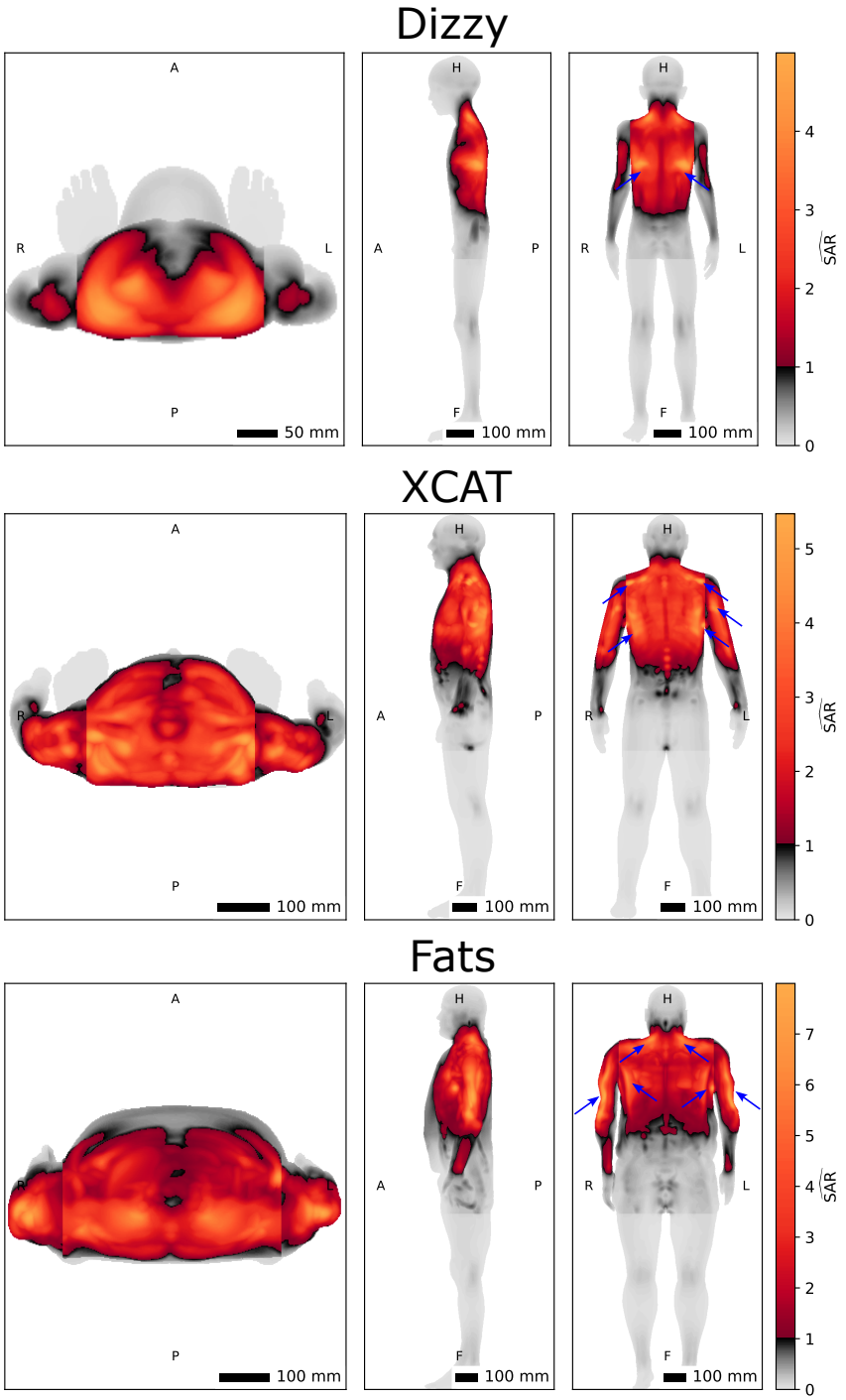

Fig. 4.14: Maximum achievable normalised SAR for models Dizzy (**top**, 25 kg), XCAT (**middle**, 78 kg) and Fats (**bottom**, 119 kg) at 16 channels and 3 T with PCM, when each single channel amplitude limit α is derived from the corresponding whole-body Q-matrix. Blue arrows point at regions with potential for high local SAR.

4.6.2 Safety factor estimation

A safety limit based on the combination of a 10 kg child-model and a 150 kg larger-bodied adult-model for a 80 kg patient would necessarily result in a high initial conservativeness due to the larger-bodied model combined with a high safety factor due to the expected high SAR in the larger-bodied model for an RF-shim that is safe for the child-model. Such approach is hence expected to result in vastly overconservative safety limits. The combination of only 'close' anchor models for a given patient is assumed to improve $\mathrm{mean}(B_1^+)$ performance without compromising safety if a sufficient number of models are available. For any practical implementation of this concept it is thus recommended that a broad variety of models is included in the initial analysis but only a smaller subset of 'most relevant' models, that are close in body height and mass to the patient, is evaluated for a specific application.

The further analysis in this chapter was limited to the relevant case of cardiac imaging for patients between 50 – 80 kg to avoid over-conservative limits as best as possible with the limited available models. This reduces the model count to seven. The analysis with all 11 models was carried out in appendix A.4. The possible height dependence of the amplitude limit α was not exploited due to the lack of certainty caused by only 11 tested models and the small differences between α of the seven included models that were below 20 %.

The anchor-target analysis was carried out with 10^6 random shim vectors for all combinations of 6 anchor models and 1 target model and for all safety limits, see Fig. 4.15. For PCM, the theoretical maximum can be calculated without testing any shim vector, see Eq. (2.24). This information is also included in the figure (red star symbols) and serves to illustrate the realisation gap, that is the difference between highest randomly encountered $\mathrm{ps}\widehat{\mathrm{SAR}}$ value and the theoretical limit $\mathrm{ps}\widehat{\mathrm{SAR}}_{\mathrm{max}}$.

The 1-channel CP mode $\mathrm{ps}\widehat{\mathrm{SAR}}$ values are by construction identical for all safety limits, see Fig. 4.15A-C. A clear hierarchy of the models is visible, like for the PCM single channel amplitude limit α, and $\mathrm{ps}\widehat{\mathrm{SAR}} > 1$ occurs only when the model with the strictest limits (Glenn for 0.5 T and 1.5 T, Yoon-sun for 3 T) becomes the target model.

Two degrees of freedom exist for the scaled RF-shim vectors at 2 channels: the relative phase-difference and amplitude-ratio between both channels. This results in a spread out distribution of $\mathrm{ps}\widehat{\mathrm{SAR}}$ with distinct more often occurring $\mathrm{ps}\widehat{\mathrm{SAR}}$ values, see Fig. 4.15D-F. Multiple models can reach $\mathrm{ps}\widehat{\mathrm{SAR}} > 1$ for SCM and PASCM, for example models Louis, Glenn, Jeduk, Duke and XCAT at 0.5 T, see panel D, as there is no hierarchy any more. Only one model can ever reach $\mathrm{ps}\widehat{\mathrm{SAR}} > 1$ for PCM by construction. The

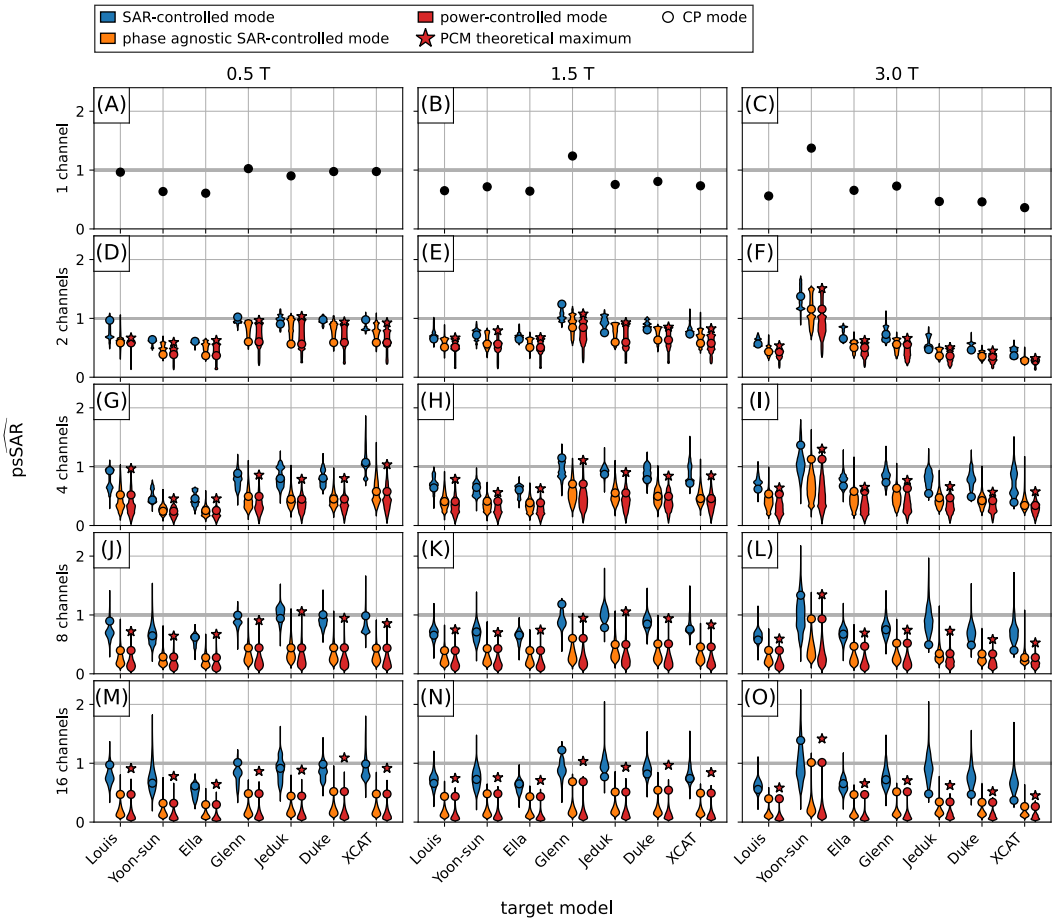

Fig. 4.15: $\widehat{\mathrm{psSAR}}$ as function of the target model in an anchor-target analysis with 10^6 random shim vectors scaled to hit the limit of the six remaining anchor models. Please note that all three control modes become identical for the single-channel CP mode. See Fig. A.3 for the analysis with all 11 anchor models. This figure by Petzold et al. [91] is licenced under CC BY 4.0.

theoretical $\widehat{\mathrm{psSAR}}$ maximum is reached for all models for PCM.

The 4 channel mode RF-shim vectors have 6 degrees of freedom and therefore more $\widehat{\mathrm{psSAR}}$ spread with smoother violin plots, see panels G-I. PCM and PASCM start to become more conservative than SCM with lower expressed $\widehat{\mathrm{psSAR}}$, as phase is neglected.

These trends continue for 8 and 16 channels, see panels J-O. Target models with $\widehat{\mathrm{psSAR}} > 1.8$ exist for 16 channels with SCM for all B_0-field strengths. The highest 10 % of $\widehat{\mathrm{psSAR}}$ values of each model occur less frequently than for the lower channel counts. The most susceptible model with the highest $\widehat{\mathrm{psSAR}}$ is not necessarily the same for all B_0: Yoon-sun is worst at 0.5 T and 3 T while Jeduk is worst at 1.5 T.

The theoretical maximum $\widehat{\mathrm{psSAR}}$ for PCM is not reached any more for PCM. Gaps of up to 30 % between highest realisation and maximum can be found for model Yoon-sun at 3 T.

The realisation gap for SCM was explored with RF-shim vector optimisation, because SCM and PASCM lack a theoretical $\widehat{\mathrm{psSAR}}$ maximum. The $\widehat{\mathrm{psSAR}}$ in model Yoon-sun at 3 T was thereby maximised for PCM and SCM with the Nelder-Mead algorithm [139] so that the six remaining models are safe, see Fig. 4.16. Model Yoon-sun was chosen as target, because it shows the highest $\widehat{\mathrm{psSAR}}$, when the other models are used as anchor.

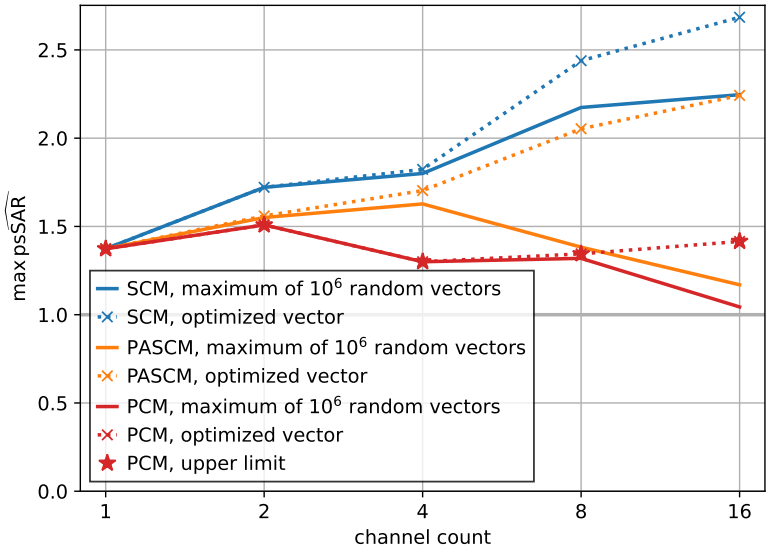

Fig. 4.16: Maximum $\widehat{\mathrm{psSAR}}$ as function of channel count for target model Yoon-sun and 6 anchors at 3 T. This figure by Petzold et al. [91] is licenced under CC BY 4.0.

The realisation gap between the 10^6 random RF-shim vectors and the optimised vector increases with channel count for all safety limits. Deviations above 5 % start to occur at 8 channels for SCM and PASCM, while they only occur for PCM at 16 channels. It can therefore be concluded that there is a remaining uncertainty for SCM and PASCM for $N_\mathrm{c} \geq 8$ when using 10^6 RF-shim vectors while PCM-safety can be ensured with its theoretical $\widehat{\mathrm{psSAR}}$ maximum.

A measure to analyse the influence of the number of anchor model on the target's $\widehat{\mathrm{psSAR}}$ overestimation is desired. Therefore, the anchor-target analysis is carried out for all combinations of 1-6 anchors and 1 target. The maximum $\widehat{\mathrm{psSAR}}$ over all shim vectors is plotted for each target as function of anchor model count as boxplot in Fig. 4.17. The 7 maximum values of

the violin plots in each panel in Fig. 4.15 are therefore contained in the rightmost boxplots with 6 anchor models of each panel in Fig. 4.17.

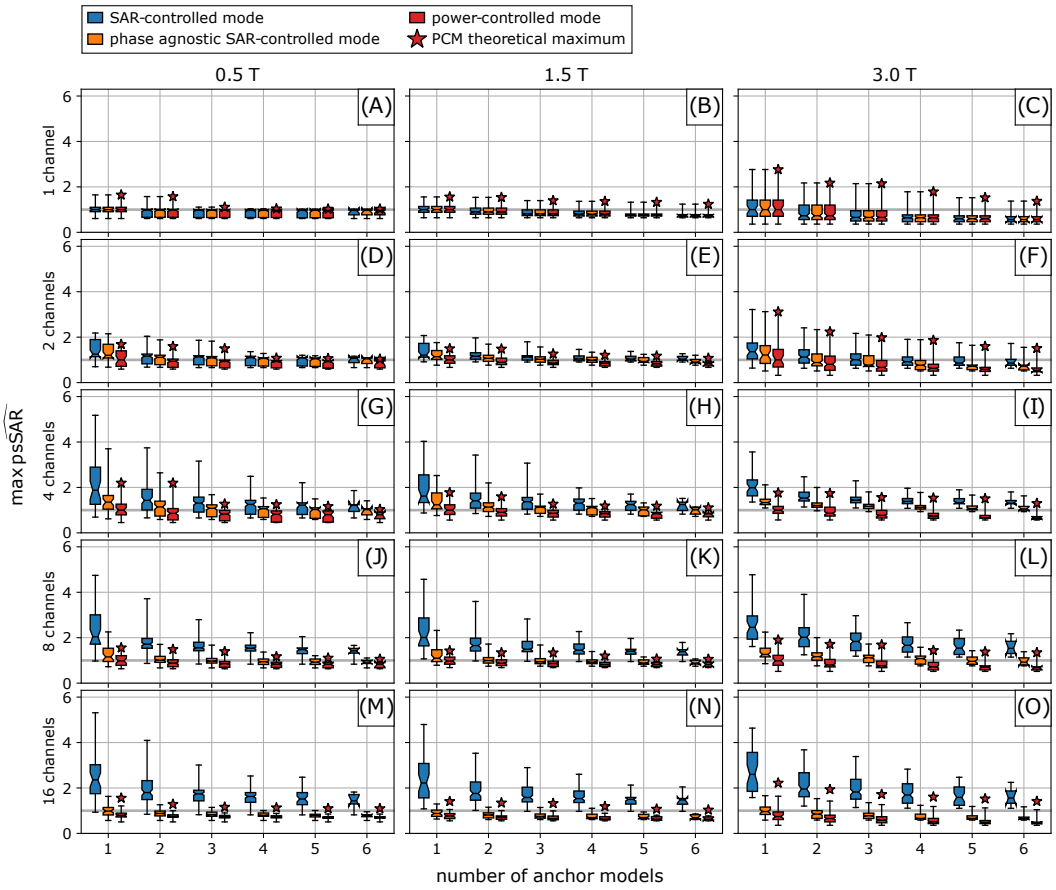

Fig. 4.17: Maximum $\widehat{\mathrm{psSAR}}$ as function of anchor model count for all possible combinations of anchor-model(s) and target model. See Fig. A.4 for the analysis with all 11 anchor models. This figure by Petzold et al. [91] is licenced under CC BY 4.0.

SCM results for only one anchor in the highest $\widehat{\mathrm{psSAR}}$ of around 5 at 0.5 T and 16 channels, see Fig. 4.17M. PASCM ($\widehat{\mathrm{psSAR}} \approx 4$ at 0.5 T and 4 channels (panel G)) and PCM ($\widehat{\mathrm{psSAR}} \approx 3$ at 3 T and 2 channels (panel F)) are more conservative. It is especially interesting to observe the 1-channel CP mode case at 3 T where 4 anchor models are necessary to achieve a safety factor below 2.

Higher numbers of anchor models lead, as expected, to more VOPs, more conservativeness, lower $\widehat{\mathrm{psSAR}}$ overshoots and therefore to lower safety factors for all channel counts and B_0-field strengths. Maximum $\widehat{\mathrm{psSAR}}$ as function of model count must therefore be (weakly) monotonically decreas-

ing. The decrease is stronger for low anchor model counts like $1 \rightarrow 2$ than for higher model counts like $5 \rightarrow 6$. It would be interesting to know how many models are necessary for each safety limit until the maximum $\widehat{\mathrm{psSAR}}$ approaches a value of 1.02 that is assumed to be negligible, see Section 4.4.

The theoretical overshoot for PCM will be zero if the lowest amplitude in a group of simulations is present twice. The most extreme case would be one anchor and one target simulation with the same single channel amplitude limit α that could lead to the conclusion that no additional simulations are necessary since safety-factor 1 is already reached. This false negative result can be avoided by checking against more target simulations. The boxplots with 5 anchors would require 3 models with the lowest amplitude limit to reach safety factor 1 if the safety factor is derived from $N_\mu - 2$ instead of $N_\mu - 1$ models. The number of selected anchors to determine the safety factor has to therefore be chosen according to the required safety needs. A more elegant way to determine the PCM limit would be the calibration against easily measurable parameters like patient mass and height, see Section 4.6.1.

4.6.3 Safety factor evaluation

It is intended to use the highest $\widehat{\mathrm{psSAR}}$ of the anchor-target analysis with 6 anchor models as safety factor for the further analysis. This safety factor, however, builds on the knowledge of all available 7 models in the patient group with body mass of 50 – 80 kg in cardiac imaging position. The model of the patient is usually not available. This section hence analyses the worst case SAR and possible $\mathrm{mean}(B_1^+)$ in completely unknown evaluation models in order to verify whether 7 models are sufficient to derive a suitable safety factor.

All $n = 7$ available models are thus separated into p primal models and $e = n - p \geq 1$ evaluation models. The purpose of the primal models is the derivation of a safety limit, which is tested for the evaluation models. An anchor-target analysis with 10^6 random RF-shim vectors is therefore carried out in the p primal models analogously to the previous subsection and the highest $\widehat{\mathrm{psSAR}}$ in the most susceptible target model for $p - 1$ anchors is used as safety factor s. The derived safety limit therefore consists of the VOPs of all p primal models multiplied by s.

The maximum possible $\widehat{\mathrm{psSAR}}$ and $\mathrm{mean}(B_1^+)$ in the e evaluation models is subsequently calculated for the 10^6 random shim vectors that are scaled to hit the limit of the primal models, see Figs. 4.18 and 4.19. This evaluation was carried out for all possible combinations of primal models and evaluation models. As at least one evaluation model and one target model is required,

this analysis is only possible up to $n - 2 = 5$ anchor models.

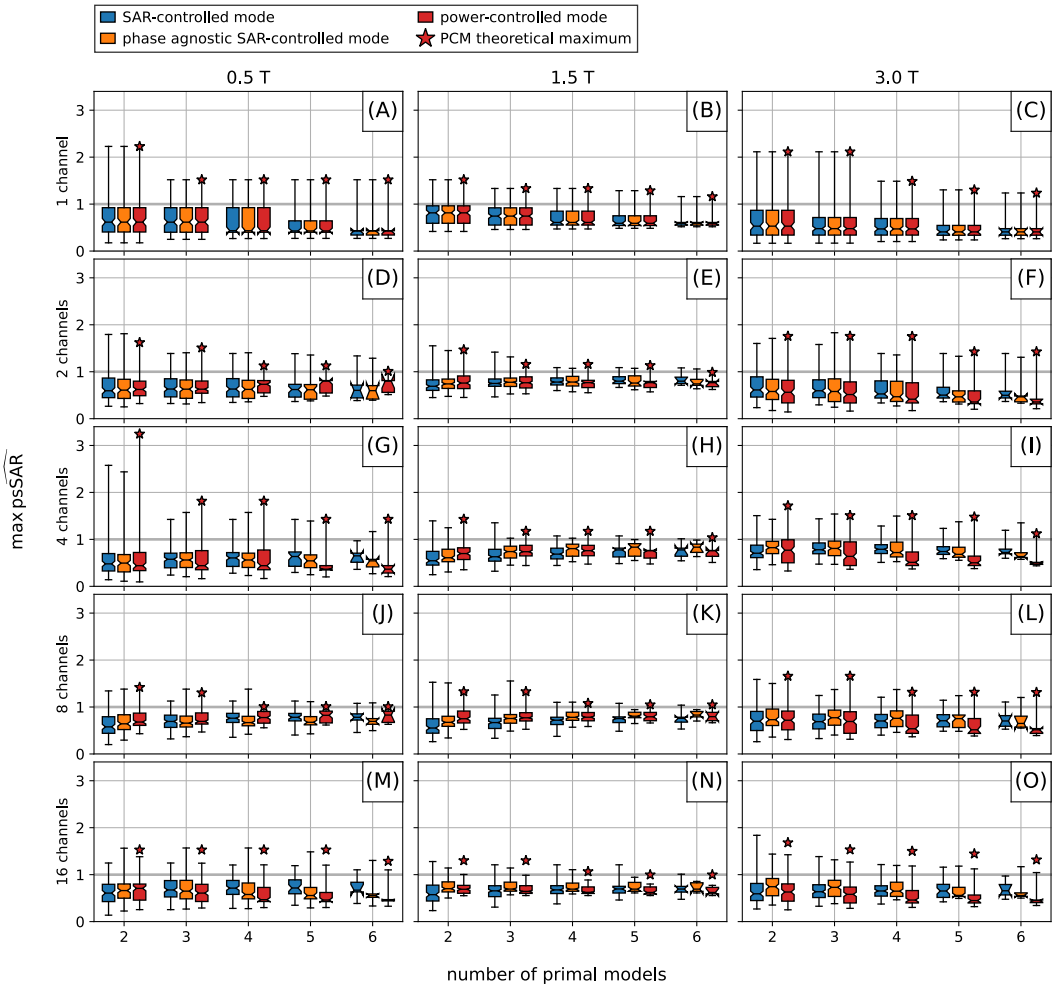

Fig. 4.18: Maximum $\widehat{\mathrm{psSAR}}$ in all evaluation models as function of primal model count for all possible combinations of evaluation and primal models. Safety limits are derived from the primal models in an anchor-target analysis with the leave one out method to obtain a safety factor. The 10^6 random shim vectors are subsequently used to calculate the $\widehat{\mathrm{psSAR}}$ in the previously unseen evaluation models.

The maximum $\widehat{\mathrm{psSAR}}$ found in the evaluation models is in general below 2, see Fig. 4.18 and the dynamic of adding models is lower than in Fig. 4.17, because no safety factor is incorporated in the later case. This safety factor leads also to the observation, that the highest $\widehat{\mathrm{psSAR}}$ for each count of n primal models in Fig. 4.18 must be smaller than the highest $\widehat{\mathrm{psSAR}}$ for n anchor models in Fig. 4.17.

Notable is the observation that the maximum $\widehat{\mathrm{psSAR}}$ decreases with the

number of primal models, even though the applied safety factor is decreasing simultaneously. This can be seen at the minimum of the $\mathrm{ps}\widehat{\mathrm{SAR}}$ boxplots, that rises with the number of primal models. It must further be noted that the safety hierarchy SCM<PASCM<PCM is no longer valid and all safety limits are very comparable. This shows the successful application of the safety factor. A sufficient model count is assumed, when $\mathrm{ps}\widehat{\mathrm{SAR}} = 1$. This is the case for 1.5 T and more than 4 channels while additional models are required for the 2 channel cases.

The decreasing safety factor with increasing primal model count can also be seen at the increasing median of the achievable $\mathrm{mean}(B_1^+)$ for SCM at 0.5 T and 1.5 T, see Fig. 4.19. This effect cannot be seen at 3 T.

The decrease in $\mathrm{mean}(B_1^+)$ with rising channel count can be explained with the increasing safety factor for higher channel counts, because it is possible to obtain field configurations where local SAR hot spots are present in one model while the other models are not affected, due to the higher number of degrees of freedom.

It can be concluded, that a higher primal model count leads to higher patient safety and higher or at least equal $\mathrm{mean}(B_1^+)$ compared to a low primal count. It is therefore indicated to derive the safety limit from as much primal models as possible and use the safety factor of the leave one out method.

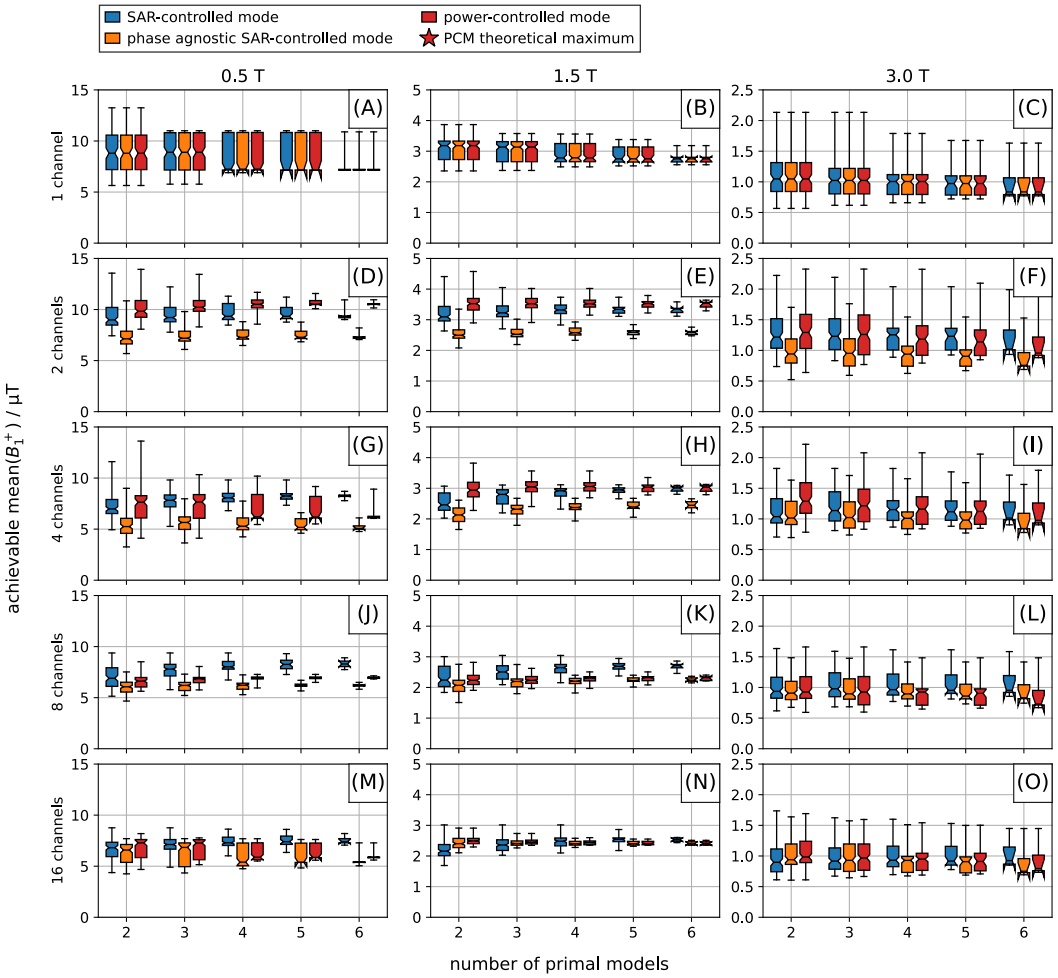

Fig. 4.19: Maximum $\mathrm{mean}(B_1^+)$ in all evaluation models as function of primal model count for all possible combinations of evaluation and primal models. Safety limits are derived from the primal models in an anchor-target analysis with the leave one out method to obtain a safety factor. The 10^6 random RF-shim vectors are subsequently used to calculate the maximum $\mathrm{mean}(B_1^+)$ in the previously unseen evaluation models.

4.6.4 B_1^+ performance comparison

An RF-shim vector for a given channel count can be scaled to fulfil any safety limit. This scaling results in different $\mathrm{mean}(B_1^+)$ but the same $\mathrm{CV}(B_1^+)$, see Eq. (2.27). The performance of all safety limits can therefore be assessed with the maximum achievable $\mathrm{mean}(B_1^+)$ for a given inhomogeneity.

It is evident from the previous analysis that SCM requires a higher safety factor than PASCM and PCM, see Fig. 4.17. SCM has, on the other hand, the best initial $\mathrm{mean}(B_1^+)$ performance, see Fig. 4.1. It is therefore interesting

to know whether these two effects cancel each other out.

This subsection therefore examines the $\mathrm{mean}(B_1^+)$ performance of the overarching safety limits that were obtained by combining the safety limits of all 7 models with the safety-factors derived from the anchor-target analysis with 6 anchors, see Fig. 4.20. The additional safety limit 'model known' is shown as reference. This mode corresponds to SCM with the current model's VOPs only without additional safety factor.

The trade-off between $\mathrm{CV}(B_1^+)$ and $\mathrm{mean}(B_1^+)$ for human voxel model Duke with 8 channels is shown as L-curve in Fig. 4.20A-C for 0.5 – 3 T. The CP mode's position with the combined limits ('model unknown'), and the model specific limit without safety factor ('model known') are shown as well.

The safety limits can be ordered in terms of their generally achievable $\mathrm{mean}(B_1^+)$ by PCM < PASCM < CP mode accommodating model uncertainty < SCM < CP mode for a known model < pTx with known model. The grey model-known data points are presented for an informative purpose and represent the best possible performance that could be reached if full knowledge about the patient would be available. This illustrates the resulting loss of $\mathrm{mean}(B_1^+)$ to ensure safety for patients where no exact model is known, but is also not safely reachable in general.

Interesting is the slope at highest $\mathrm{mean}(B_1^+)$ of all L-curves where <5 % of $\mathrm{mean}(B_1^+)$ can be traded for 50 % lower $\mathrm{CV}(B_1^+)$. A major improvement in homogeneity can therefore be traded for a minor decrease in $\mathrm{mean}(B_1^+)$.

Two performance measures were compared for all configurations:

1. The $\mathrm{mean}(B_1^+)$ of the intersection between the L-curve and $\mathrm{CV}(B_1^+) = 0.1$ that was marked by squares. $\mathrm{CV}(B_1^+) = 0.1$ corresponds to the worst homogeneity for the single channel mode at 1.5 T of all 7 tested models. This homogeneity is assumed to be sufficient because of the lack of pTx in clinical scanners at 1.5 T, but not achievable for low channel counts at 3 T, see Fig. 4.20D-F.

2. The lowest cost $C = -\mathrm{mean}(B_1^+)/\mu\mathrm{T} + \lambda \times \mathrm{CV}(B_1^+)$ of all shim vectors for $\lambda = 3$. The shim vector with minimal C was marked with a triangle. The regularisation parameter $\lambda = 3$ was chosen to result in $\mathrm{CV}(B_1^+) \approx 0.1$ for 3 T. This performance measure has the advantage that all channel counts of 3 T can be included in the comparison. See Fig. 4.20G-I.

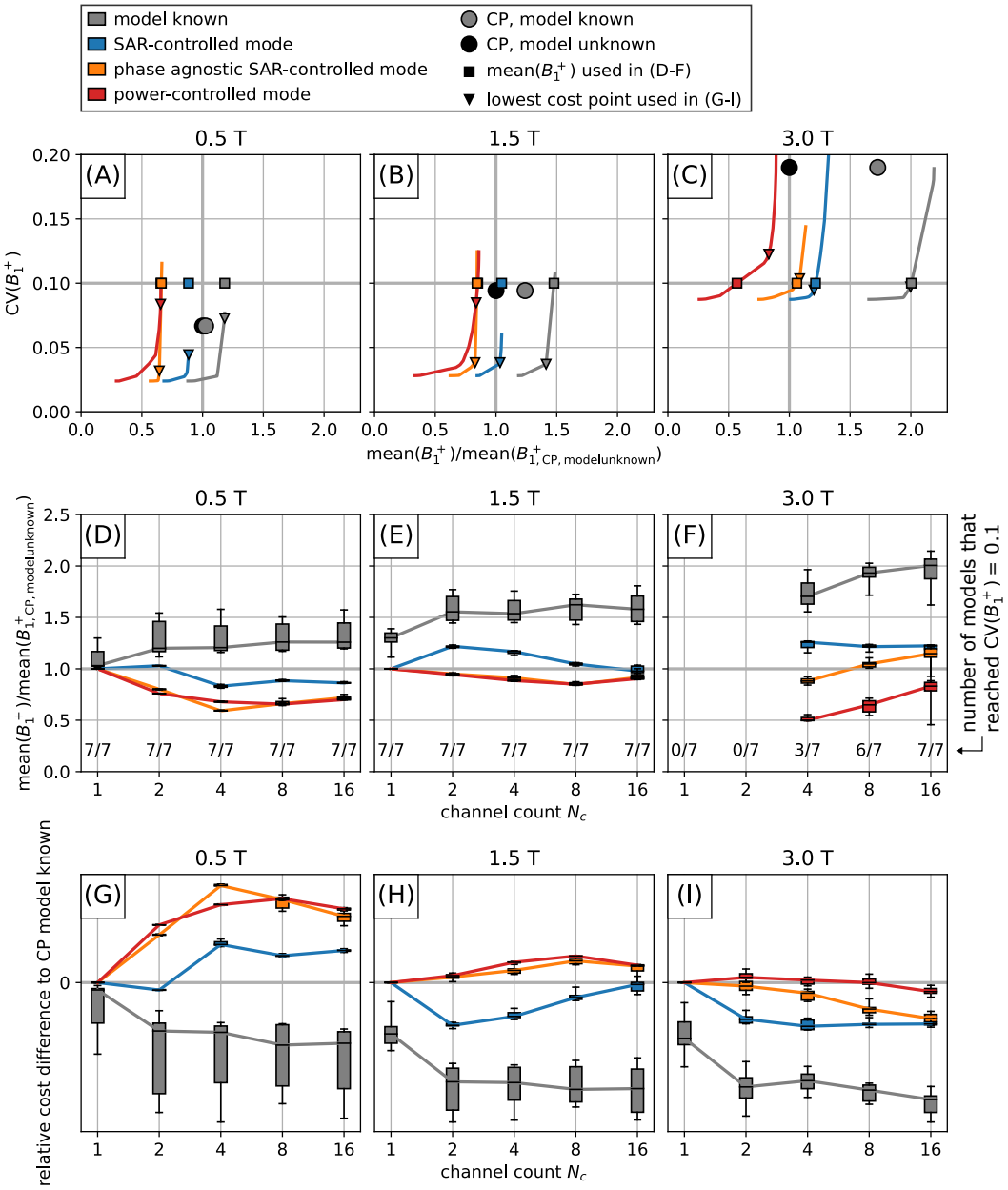

Fig. 4.20: $\mathrm{mean}(B_1^+)$ performance for SCM, PASCM and PCM (unknown model condition, i.e. the VOPs of all 7 models are combined with a safety limit specific safety factor) or with model known (SCM, VOPs of current model only, no safety factor). $\mathrm{mean}(B_1^+)$ is plotted relative to the $\mathrm{mean}(B_1^+)$ of the CP mode with unknown model condition. (**A-C**) Trade-off between $\mathrm{mean}(B_1^+)$ and $\mathrm{CV}(B_1^+)$ for model Duke and 8 channels. (**D-F**) $\mathrm{mean}(B_1^+)$ that reaches $\mathrm{CV}(B_1^+) = 0.1$ divided by the $\mathrm{mean}(B_1^+)$ of the CP mode. Higher values are better. (**G-I**) Difference of cost $C = -\mathrm{mean}(B_1^+)/\mu\mathrm{T} + 3 \times \mathrm{CV}(B_1^+)$ between CP mode and the best shim vector of the pTx optimised shim vectors. G-I use different y-scales and are hence not directly comparable. See Fig. A.5 for the analysis with all 11 anchor models. This figure by Petzold et al. [91] is licenced under CC BY 4.0.

The boxplots of SCM, PASCM and PCM in panel D-I show very little spread compared to the model known boxplots. This safety limit is the same for all points of the SCM, PASCM and PCM boxes, respectively, but model dependent for the 'model known' boxes. The channel-wise B_1^+ maps are the only changing optimisation parameters between the SCM, PASCM and PCM optimisation runs for all models. It must therefore be concluded, that the safety limit is of higher relevance in determining the $\mathrm{mean}(B_1^+)$ performance.

An increase of 30 – 100 % of $\mathrm{mean}(B_1^+)$ would be possible if the exact patient model would be known. A better, or at least the same, $\mathrm{mean}(B_1^+)$ performance as for the 8 channel configuration is expected for the 16 channel 'model known' configuration, because the 8 channel configuration is a proper subset of the 16 channel configuration. The $\mathrm{mean}(B_1^+)$ drops, however, between 8 channels and 16 channels for model known at 0.5 T and 1.5 T (Fig. 4.20D-F). This can be explained with VOP compression artefacts, see Fig. 4.4, and does not occur if all Q-matrices instead of the VOPs are used for safety assessment.

PCM and PASCM perform very close to each other for 0.5 T and 1.5 T, but, in general, worse than the CP mode, see Fig. 4.20D,E,G,H.

SCM performs best of all safety limits with its highest performance for 2 channels. For 0.5 T, higher channel counts lead to a lower $\mathrm{mean}(B_1^+)$ compared to the CP mode. For 1.5 T, the $\mathrm{mean}(B_1^+)$ is higher than the CP mode, but it decreases until it approaches the CP mode's performance at 16 channels. The decrease of performance for higher channel counts is caused by higher safety factors and VOP compression losses that are stronger than the gain from more available degrees of freedom. The performance differences between all 3 modes are minor for 1.5 T at 16 channels.

The general performance order PCM < PASCM < SCM also holds for 3 T, see Fig. 4.20F,I. Different to 0.5 T and 1.5 T is that PASCM performs for low channel counts comparable to PCM and for high channel counts close to SCM with only minor differences between PASCM and SCM for 16 channels. At least 16 channels were necessary to reach $\mathrm{CV}(B_1^+) = 0.1$ for all models, while 2 channels were sufficient for no model, see Fig. 4.15F.

4.7 Discussion

Not knowing the exact body model, position or posture of the patient leads to lower $\mathrm{mean}(B_1^+)$ to accommodate local SAR uncertainties.

Position uncertainty can be mitigated by combining the VOPs of the 8 simulations on the corners of a rectangular cuboid to assess possible patient positions within the given cuboid. No additional safety factor is needed

for tight enough spacing of the pre-calculated simulations. A nevertheless occurring small loss of 5 % $\mathrm{mean}(B_1^+)$ for CP mode and 10 % $\mathrm{mean}(B_1^+)$ for pTx is caused by the more conservative limits of the anchors.

The $\mathrm{mean}(B_1^+)$ loss to accommodate for unknown patient models is, with up to 50 % depending on channel count and B_0-field strength, much larger than $\mathrm{mean}(B_1^+)$ loss caused by position uncertainty. The use of pTx was for all B_0-field strengths advantageous compared to the single channel CP mode, even if higher safety factors were required. The highest pTx $\mathrm{mean}(B_1^+)$ increase of 25 % was found for SCM at 2 channels (0.5 T and 1.5 T) or 4 channels (3 T). A higher number of channels brings B_1^+ homogeneity gains but no improvements or even a decrease in $\mathrm{mean}(B_1^+)$. With the possible exception of 3 T, higher channel counts are not motivated by performance; the capability to mitigate implant heating [9, 35] is the discipline where pTx excels.

Local SAR is not relevant for single channel volume coils when following the IEC standard [45]. It was included in this analysis, as too high local SAR values are reached for a CP shim scaled to hit the whole body limit [46, 47, 128] with $\mathrm{ps}\widehat{\mathrm{SAR}}$ overshoots of up to factor 4 for the models of this analysis, see Fig. 3.7, that corresponds to a factor of 2 in $\mathrm{mean}(B_1^+)$. If it is assumed that the IEC global SAR limits are appropriate – burns are reported in only 0.000 75 % of all MR exams [166] – then an update of the IEC standard's approach to local SAR is recommended.

Small possible standard changes would be the increase of the local SAR limits and the introduction of tissue- and region-specific local SAR limits with higher granularity than the binary choice between extremities and remaining body. Major overhauls, like the cumulative equivalent minutes at 43 °C (CEM43°C) formalism [127, 154, 167, 168] or temperature matrices [169] with a limit of 39 °C or tissue specific limits, are scientifically appealing but have been explicitly rejected during the last revision of this document [45, 126]. It is recommended to use an exponential decrease as windowing function instead of the 6 min long rectangular pulse like in SAR for a more natural dynamic of heat transfer.

SCM, PASCM and PCM are applicable to any limit where a shim vector $\boldsymbol{u}$ is considered safe if $\boldsymbol{u}^\dagger \boldsymbol{M} \boldsymbol{u} \leq 1$ for a normalised matrix M. Pivoting, for example, to temperature matrices [169] would not change the principle, but might alter safety factors and resulting $\mathrm{mean}(B_1^+)$ performance.

A possible implementation of a native safety limit would be the simulation of multiple models at multiple positions and subsequent combination of their safety limits [80]. A spatial resolution of 3 steps in x- and y-direction (e.g. with 50 mm distance) and 10 steps in z-direction (e.g. with 100 mm distance) results in around 100 positions per model. With 10 different voxel models, this results in 1000 simulations. The EM FDTD simulation for 3 T

took 8 h for 48 ports with a Nvidia Quadro GV100 GPU and resulted in around 50 GB of data. Around 4 h of time are required for VOP compression with an Intel Xeon Silver 4108 CPU for an 8 channel configuration with 10^7 voxels [133]. Processing these 1000 simulations with this setup would take 500 d for SCM and 300 d for PCM where VOP calculation is not necessary. 50 TB of raw data are generated in this process. Such computational loads should be manageable for an MR system manufacturer.

Safety assessment could then happen with the combined safety limits of the closest simulations in all 3 spatial directions forming a box around the patient position. It might be advantageous to split patients into certain groups like 0 – 30 kg, 25 – 60 kg, 50 – 100 kg, 80 kg+ and only use the VOPs corresponding to the patient for safety assessment to eliminate artefacts caused by vastly different models. For PCM there might be the possibility to derive an appropriate single channel amplitude limit by using the patients mass or height and interpolate the single channel amplitude limit α between the corner's anchor simulations.

5 A sensor-based implant safety concept

This chapter describes an AIMD RF safety concept that is separating native safety assessment (patient without implant) from implant safety, see Fig. 5.1.

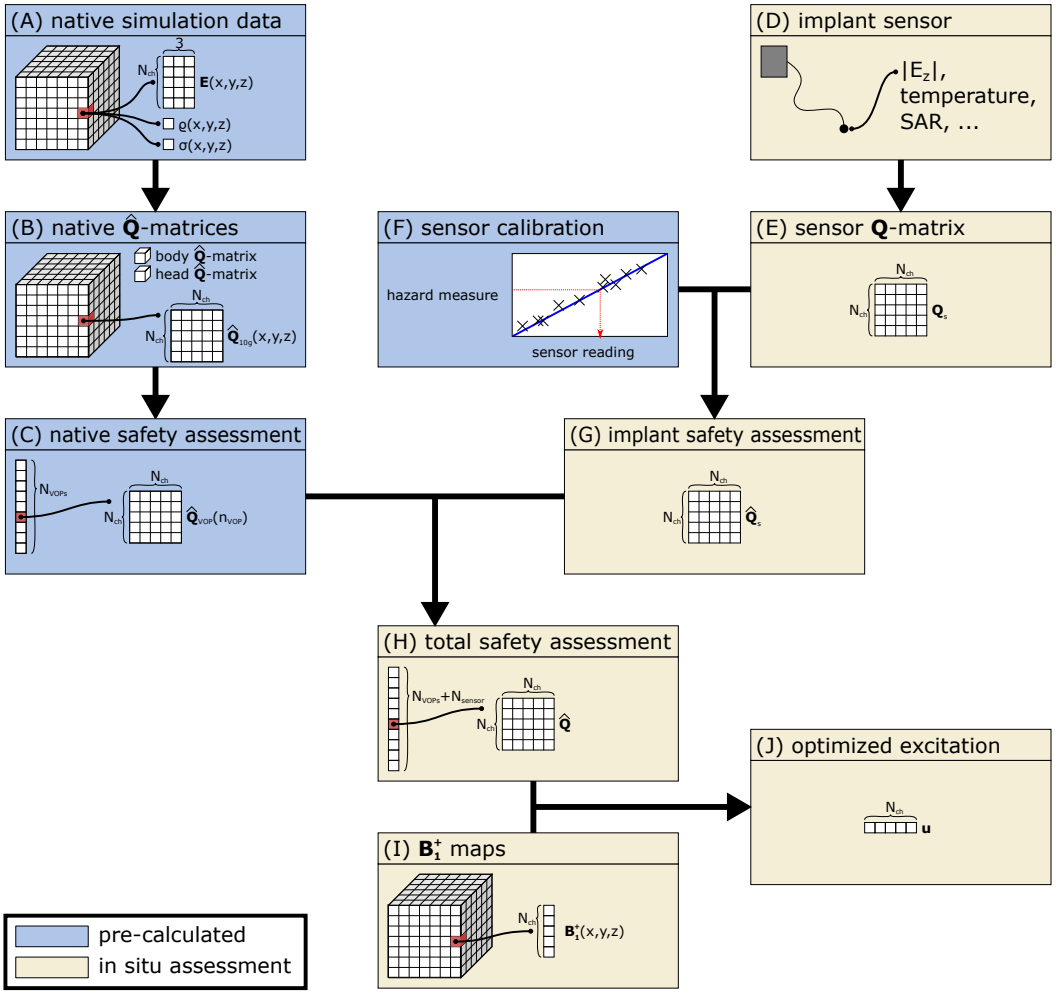

Fig. 5.1: Concept to ensure implant RF safety in pTx MRI. Native safety assessment (**A-C**) is pre-calculated and separated from implant safety assessment (**D-G**). Combining both parts gives the total safety assessment (**H**). If pTx is available and the channel-wise B_1^+ maps are known (**I**), the RF-shim vector providing the best image quality can be selected from the set of all safe vectors (**J**). This figure by Petzold et al. [35] is licenced under CC BY 4.0.

The presented concept builds on the well-known fact that the multiple degrees of freedom in pTx can be used to modify the electromagnetic field to avoid pathologic hot spots at implants [9, 10, 33–43]. New in the proposed concept is the calibration of an implant sensor to integrate implant safety into existing native safety concepts. A short overview is given in the following before the details are elaborated in further sections.

The first part of the concept consists of the native safety assessment for the patient if no implant is present, see Chapter 4 for possible steps to ensure safety even if the patient's exact digital patient model is not available or no simulation with the right spatial position is present. Native safety is in the responsibility of the MR system manufacturer. On the scanner, it is implemented via pre-calculated excitation limits that are valid for the patient under test, see Fig. 5.1A-C for an example with SCM.

This chapter focuses on possible implant-integrated sensors and strategies on how to use the sensor information to provide implant-safe RF-shims for patients. The aim is to use affordable and small RMS sensors to measure the RF-safety directly in AIMDs [10, 25–27].

The need for additional electronics renders this concept less suited for passive implants like hip joints. This concept benefits significantly from pTx, where the available degrees of freedom can be leveraged to achieve implant-safe RF-shims with high $\mathrm{mean}(B_1^+)$ [9].

Ensuring implant-safe RF-shims would lie in the joint responsibility of the implant manufacturer and MR system manufacturer. The implant manufacturer would be required to provide the necessary safety information to the MR scanner: a measure that is correlated to the implant-caused hazard and its maximum safe value. The implant manufacturer shall ensure that the sensor (D) is placed on the implant in such a way that the safety relevant hotspot is correctly covered. The sensor's output must correlate with an appropriate hazard measure and must be calibrated in that metric (F). If this is fulfilled, a sensor matrix $\boldsymbol{Q}_s$ can be constructed in situ from the RMS measurements like in Section 2.5.2 [10] (E) and normalised with the hazard measure (G).

The combination of native safety assessment and implant safety assessment leads to the total safety assessment (H) that can be used together with channel-wise B_1^+ maps of the patient (I) for optimisation of the RF-shim (J).

Spinal cord stimulators can result in a high potential patient danger in MRI because of sensitive neural tissue at the implant's tip. A list of MR conditional spinal cord stimulators is shown in Tab. 5.1.

Tab. 5.1: Spinal cord stimulators with the best MR compatibility of the 4 companies active in the US market [13].

manufacturer	product line	B_0	leads	RF transmit coils	patient scan position	patient orientation	SAR limit	B_1^+ RMS limit	time limit	source
Medtronic	Intellis, Vanta	1.5	SureScan	body, head, lower extremity	all	prone, supine	normal mode	-	30 min in 90 min	[15]
Boston Scientific	Precision Montage	1.5	Avista (percutaneous 8 contacts)	body, head, lower extremity	all	prone, supine	normal mode	-	-	[14]
		1.5	others	body, head, lower extremity	all	prone, supine	normal mode; $\mathrm{wbSAR} \leq 0.2\,\mathrm{W\,kg^{-1}}$, if no B_1^+ RMS available	2 µT		
Nevro	Senza HFX iQ	1.5	percutaneous	body	between nose and 203 mm superior to knee	all	$\mathrm{wbSAR} \leq 0.4\,\mathrm{W\,kg^{-1}}$, $\mathrm{hdSAR} \leq 0.6\,\mathrm{W\,kg^{-1}}$	2 µT	30 min, then 60 min cooling	[16]
		1.5	percutaneous	body	else	all	normal mode	-		
		1.5	surpass surgical	body	all	all	$\mathrm{wbSAR} \leq 0.24\,\mathrm{W\,kg^{-1}}$, $\mathrm{hdSAR} \leq 0.4\,\mathrm{W\,kg^{-1}}$	1.6 µT		
		1.5, 3	all	head, local	no part of implant within the coil	all	normal mode	-		
Abbott	Proclaim XR, Proclaim Plus	1.5	Octrode 3186	body, head, extremity	all	supine with arms at side	normal mode	-	30 min, then 30 min cooling	[170]
		1.5	Penta 3228	body	all	supine with arms at side	$\mathrm{wbSAR} \leq 0.1\,\mathrm{W\,kg^{-1}}$	-		
		1.5	Penta 3228	head, local	head, extremities except hip and shoulder	supine with arms at side	normal mode	-		

The implant with the least restrictions (Boston Scientific Precision Montage [14]) is only allowed for 1.5 T in prone or supine imaging with a body coil for body imaging at normal mode SAR limits. Head coils and lower extremity coils are allowed as well. The implants of all other vendors require additional time limits with generally 30 min scan time followed by cooling for 30 – 60 min, limited B_1^+ RMS and limited whole body SAR.

Implementing the described safety approach for spinal cord stimulators would allow for a direct, measurement-based patient-specific safety assessment. This results in less required safety leeway and therefore higher B_1^+ performance. Currently imposed limits like global B_1^+ RMS, scan time, patient orientation and native SAR restriction beyond the IEC standard would not be needed any more. Different B_0-field strengths like 0.5 T, 3 T and 7 T are possible with a corresponding calibration as well.

These benefits are independent of the availability of pTx. Small spatial patient movements could be examined if no pTx is present, in order to find a position with lower tip heating as the tip heating is very sensitive to implant-path or -position changes [8, 10, 90, 171]. The added major benefit of pTx is the ability to modulate the E-field to lower the implant tip heating, resulting in better image quality with higher $\mathrm{mean}(B_1^+)$, improved homogeneity and less susceptibility artefacts [9].

It was hence decided to investigate the implant safety concept with a spinal cord mock implant because of the high potential to improve the patient safety while maintaining $\mathrm{mean}(B_1^+)$ [35]. The implant was an insulated straight wire with 300 mm length and 10 mm uninsulated tip, see Fig. 5.2.

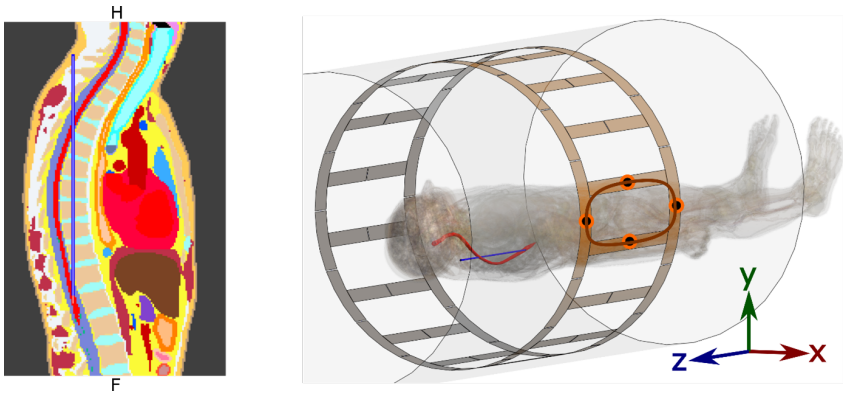

Fig. 5.2: Setup of the simulated spinal cord mock implant (blue) in human voxel model Duke touching the spinal cord (red) with its tip at position $x = 0$, $y = -106\,\mathrm{mm}$, $z = -130\,\mathrm{mm}$ relative to the coil centre. Left: Sagittal slice. Right: 3D view. One channel of the 8 channel configuration and its ports are marked in orange. This figure by Petzold et al. [35] is licenced under CC BY 4.0.

The exact knowledge of the patient model in the cardiac imaging position was assumed. The implant safety concept is first demonstrated at 3 T and 8 channels with SCM. The native safety limits accounting for model uncertainties from the previous chapter and other combinations of B_0 (0.5 T, 1.5 T and 3 T) and channel count (1, 2, 4, 8, 16) are presented subsequently to assess the $\mathrm{mean}(B_1^+)$ performance of the native limits.

Two series of simulations were carried out: the native case (Duke without implant) and the implant case (Duke with the implant).

Parts of this chapter was published in a journal paper [35] and in two conference abstracts [92, 93].

5.1 Investigating the implant sensor placement

The described safety concept requires sensor measurements from all possible implant-caused hot spots. The implant is safe and no further action is necessary if no hot spot exists. The number of required sensors is otherwise equal to the number of hot spots. Multiple sensors are likely required for implants with multiple electrodes and sufficient span like spinal cord stimulators [172]. It is worth noting that the number and severity of the hotspots depend on the used native safety limit.

Two simulation-based methods are presented that can discover all hot spots as a consistence check for the specific investigated implant, that can be simulated in Tier 4. The general method is a modified anchor-target analysis and is applicable with all presented safety limits.

The native case is thereby used as anchor, while the implant case acts as target. It is not possible to use a high amount of RF-shim-vectors for testing as the SAR needs to be evaluated for all Q-matrices of the implant case. It was therefore decided to use the eigenvectors with the highest eigenvalue of all VOPs $\boldsymbol{u}$ of anchor and target, because of the expected broad distribution in the RF-shim vector space. These vectors were scaled according to the native case limit with all normalised anchor Q-matrices $\hat{\boldsymbol{Q}}_{\mathrm{nat}}$ and used to calculate an estimation for the highest local SAR $\widehat{\mathrm{SAR}}_{\mathrm{maxest.}}(\boldsymbol{r})$ at location $\boldsymbol{r}$ for the implant case $\hat{\boldsymbol{Q}}_{\mathrm{imp}}$.

This results for SCM in

$$\widehat{\mathrm{SAR}}_{\mathrm{maxest.}}(\boldsymbol{r}) = \max_{\boldsymbol{u}} \frac{\boldsymbol{u}^\dagger \hat{\boldsymbol{Q}}_{\mathrm{imp}}(\boldsymbol{r})\boldsymbol{u}}{\max_{\boldsymbol{r}} \boldsymbol{u}^\dagger \hat{\boldsymbol{Q}}_{\mathrm{nat}}(\boldsymbol{r})\boldsymbol{u}}. \tag{5.1}$$

The estimations for PASCM and PCM follow analogously to Eq. (5.1). Maximum intensity projections of $\widehat{\mathrm{SAR}}_{\mathrm{maxest.}}(\boldsymbol{r})$ for SCM are shown in Fig. 5.3.

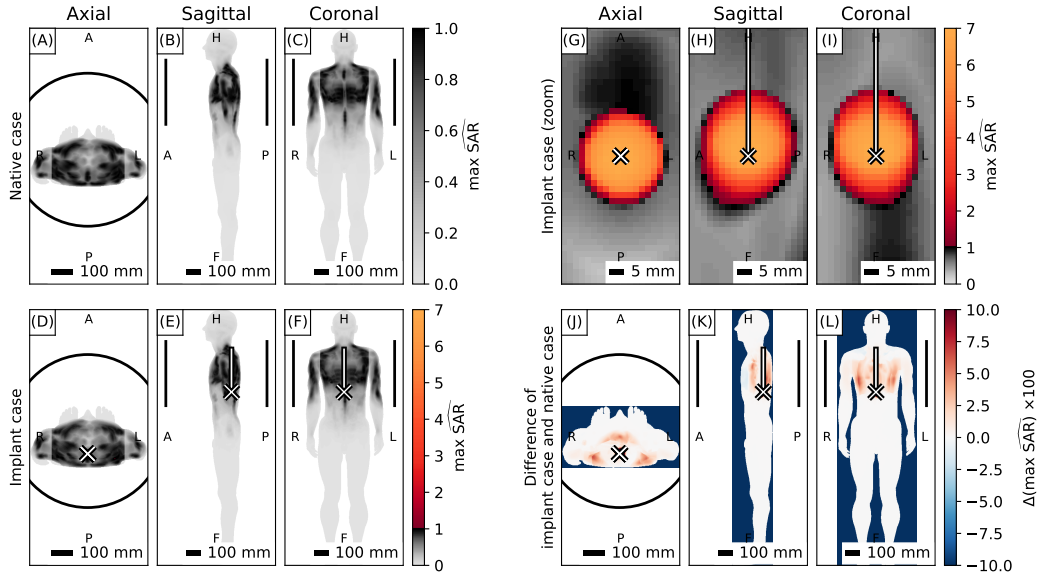

Fig. 5.3: Estimated worst case $\widehat{\mathrm{SAR}}$ as estimation based on the eigenvectors of the VOPs of native case and implant case scaled to hit the native case limit for SCM. (**A-C**) Native case. $\max \widehat{\mathrm{SAR}} \leq 1$ is fulfilled by construction. (**D-I**) Implant case, with (**G-I**) as zoom. (**J-I**) Difference implant case - native case in percent. The implant is marked by a white line with a cross at its uninsulated tip. The position of the RF-coil is marked with black lines. This figure by Petzold et al. [35] is licenced under CC BY 4.0.

The second, PCM specific method exploits the ability to derive a mathematical upper limit with the one-norm of the Q-matrices, see Section A.2. The maximum possible SAR at each location $\boldsymbol{r}$ in the implant case is calculated directly using the maximum single channel amplitude α_{nat} of the native case and the normalised Q-matrices of the implant case $\hat{\boldsymbol{Q}}_{\mathrm{imp}}$ by

$$\widehat{\mathrm{SAR}}_{\mathrm{max}}(\boldsymbol{r}) = \alpha_{\mathrm{nat}}^2 \sum_{i,k} |(\hat{\boldsymbol{Q}}_{\mathrm{imp}}(\boldsymbol{r}))_{i,k}| \tag{5.2}$$

Maximum intensity projections of $\widehat{\mathrm{SAR}}_{\mathrm{max}}(\boldsymbol{r})$ are shown in Fig. 5.4.

Only one hot spot with a diameter of 30 mm at the uninsulated tip is visible for both approaches. A $\mathrm{ps}\widehat{\mathrm{SAR}}$ estimation of 7 can be found for SCM compared to theoretical $\mathrm{ps}\widehat{\mathrm{SAR}} = 5$ for PCM showing the higher conservativeness of PCM. Some minor SAR increase below 10 % is also visible all over the exposed upper body, but negligible in comparison to the implant.

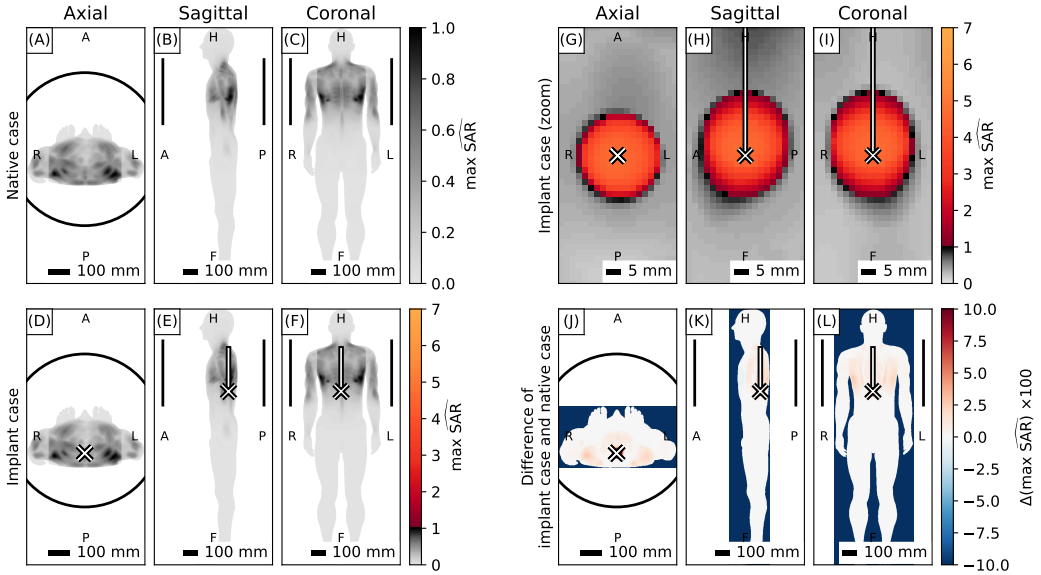

Fig. 5.4: Theoretical worst case $\widehat{\mathrm{SAR}}$ based on the native case single channel amplitude limit α and the Q-matrices of native case respective implant case for PCM. (**A-C**) Native case. $\max \widehat{\mathrm{SAR}} \leq 1$ is fulfilled by construction. (**D-I**) Implant case, with (**G-I**) as zoom. (**J-I**) Difference implant case - native case in percent. The implant is marked by a white line with a cross at its uninsulated tip. The position of the RF-coil is marked with black lines.

It is important to note that local $\widehat{\mathrm{SAR}}$ values below 1 are not sufficient to ensure safety for implants as the concentrated energy deposition can be focused on a region much smaller than the 10 g averaging region [75]. This can also be seen for the investigated implant where a temperature of nearly 41 °C can be found at the implant tip for the CP mode RF-shim scaled to hit the normal mode limit of 10 W kg^{-1} for the implant case, see Fig. 5.5.

The presence of only one hot spot was expected for the given implant geometry. The location of the single hot spot at an implant's tip is also a requirement for the common Tier 3 implant safety assessment according to ISO/TS 10974 [11], using the transfer function [130]. It is generally necessary to verify the assumed hot spots as they might also occur at unexpected positions [171] like the generator housing [18].

Hot spot locations might also be determined experimentally in commercially available test beds. Manufacturers should still carry out simulations for verification purposes.

Please note that Tier 4 simulations are required to search for hot spot locations with this simulation approach. Such simulations are not feasible for realistic implants with the currently available computational power. The

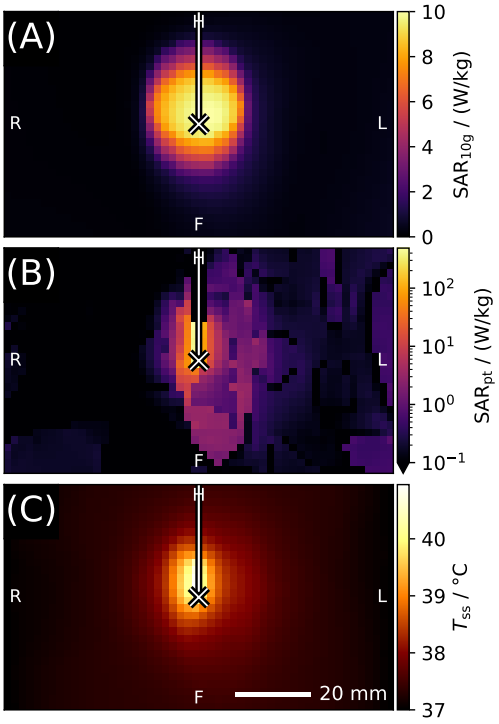

Fig. 5.5: The failure of the 10 g averaged SAR limit for implant safety assessment. Excitation of model Duke at 3 T with the CP mode scaled to hit the normal mode 10 g averaged SAR limit of 10 W kg^{-1}. (**A**) 10 g averaged SAR. (**B**) Point SAR. Please note the logarithmic scale. (**C**) Steady state temperature. This figure by Petzold et al. [35] is licenced under CC BY 4.0 and was adapted by only showing 3 panels.

hot spot can be assumed to be at the tip of implant leads following the assumptions of the state of the art Tier 3 approach [11].

5.2 Investigating safety measures

This sections examines which sensors are suitable for implant safety assessment by investing the correlation between possible sensor readings and hazard measures.

Four hazard measures were tested:

1. 10 g averaged SAR $\mathrm{SAR}_{10\,\mathrm{g}}$, like local SAR for native tissue in IEC 60601-2-33 [45],

2. point SAR $\mathrm{SAR}_{\mathrm{pt}}$ that corresponds to the voxel volume $(2\,\mathrm{mm})^3$,

3. steady state temperature T_{ss} and

4. implant-caused temperature rise ΔT_{imp} as difference between the steady state temperatures of implant case and native case.

For each of these hazard measures, its maximum value was evaluated in the ROI that is the volume $x \times y \times z = 40\,\mathrm{mm} \times 40\,\mathrm{mm} \times 80\,\mathrm{mm}$ centred on the implant tip containing the allocated hot spot, see Figs. 5.3 and 5.4.

These hazard measures were compared to five RMS sensor signals. It is necessary that the measurement time of these sensors is reasonably small to achieve Q-matrix acquisition times $t_{\mathrm{Q}} \ll 1\,\mathrm{min}$ in order to be integrable in the safety concept. The most obvious sensor reading, the steady state temperature, is therefore not possible. More constraints like the sensor integrability and measurement errors [10] need to be accounted for in a practical implementation. The first four presented sensor signals were determined as mean value over the 8 voxels that touch the implant tip with their corners:

1. point SAR, called sensor SAR in the following for better clarity,

2. magnitude of the E-field in z-direction $|E_z|$,

3. magnitude of the H-field $|\boldsymbol{H}|$ and

4. temperature rise $\mathrm{d}T/\mathrm{d}t|_{T=T_{\mathrm{i}}}$ in the first second ('$\mathrm{d}t = 1\,\mathrm{s}$') of heating for initial temperatures $T_{\mathrm{i}} = 37.2\,^{\circ}\mathrm{C},\ 37.5\,^{\circ}\mathrm{C},\ 38\,^{\circ}\mathrm{C}$ and $38.5\,^{\circ}\mathrm{C}$. $37.2\,^{\circ}\mathrm{C}$ corresponds to the steady state temperature of the native case without RF power that is caused by the metabolism.

5. The current in the implant I_{RF} at two positions z_{sensor} in 10 mm and 250 mm distance to the implant tip, respectively, was calculated using Ampère's circuital law in a 2×2 voxel rectangular loop around the lead on curve C by

$$I_{\mathrm{RF}} = \oint_C \boldsymbol{H}\mathrm{d}l. \tag{5.3}$$

The curve was evaluated on the voxel mesh for each channel c with

voxel size $\Delta l = 2\,\mathrm{mm}$ as

$$\boldsymbol{I}_{\mathrm{RF}} = \boldsymbol{I}_{\mathrm{RF},y\uparrow} + \boldsymbol{I}_{\mathrm{RF},x\rightarrow} + \boldsymbol{I}_{\mathrm{RF},y\downarrow} + \boldsymbol{I}_{\mathrm{RF},x\leftarrow} \quad \text{with} \tag{5.4}$$

$$\boldsymbol{I}_{\mathrm{RF},y\uparrow} = \sum_{y} \boldsymbol{H}(c, x = x_{\mathrm{low}}, y, z = z_{\mathrm{sensor}})\Delta l, \tag{5.5}$$

$$\boldsymbol{I}_{\mathrm{RF},x\rightarrow} = \sum_{x} \boldsymbol{H}(c, x, y = y_{\mathrm{high}}, z = z_{\mathrm{sensor}})\Delta l, \tag{5.6}$$

$$\boldsymbol{I}_{\mathrm{RF},y\downarrow} = -\sum_{y} \boldsymbol{H}(c, x = x_{\mathrm{high}}, y, z = z_{\mathrm{sensor}})\Delta l \text{ and} \tag{5.7}$$

$$\boldsymbol{I}_{\mathrm{RF},x\leftarrow} = -\sum_{x} \boldsymbol{H}(c, x, y = y_{\mathrm{low}}, z = z_{\mathrm{sensor}})\Delta l. \tag{5.8}$$

A $\boldsymbol{Q}_{\mathrm{RF}}$ matrix was calculated with $\boldsymbol{I}$ analogously to the SAR Q-matrices, see Eq. (2.11).

All four hazard measures (rows) are shown as function of sensor measurements (columns) in a matrix to investigate the correlation, see Fig. 5.6. This correlation is necessary for a later calibration of the hazard measure against the sensor measurement. The hazard measures are power quantities linked to the energy deposition in the tissue. The root-power quantities (E_z, $|\boldsymbol{H}|$, I_{RF}) were therefore depicted as squared value to achieve a linearisation.

Only minor differences between the four hazard measure rows can be seen. The main difference of the hazard measures lies in their susceptibility to record signals caused by the native background instead of the implant. Point SAR is robust against native influences as the implant-caused high point SAR values at the sensor's location dominate the ROI even for a low implant tip hazard. A native influence can be observed for $\mathrm{SAR}_{10\,\mathrm{g}} \leq 10\,\mathrm{W\,kg^{-1}}$ where a higher than expected $\mathrm{SAR}_{10\,\mathrm{g}}$ is caused by the native SAR within the ROI at a location away from the implant tip that cannot be measured by the sensor directly. No native influence on ΔT_{imp} is observable as expected by construction. A smaller influence than for $\mathrm{SAR}_{10\,\mathrm{g}}$ exists for steady state temperature $T_{\mathrm{ss}} \leq 39\,^{\circ}\mathrm{C}$. It must therefore be concluded, that there is no benefit of arbitrarily low implant safety limits well below the native hazard as the native hazards are dominating in this case.

Comparing the temperature hazards with the SAR-based hazards, the temperature hazards have the distinct advantage that the temperature correlates directly to tissue damage [128] and problems with SAR averaging in vicinity of implants [75] can be eliminated.

A more differentiated picture emerges for the different sensors. Sensor SAR correlates linearly to all hazard measures. The same holds true for the square of the E-field's dominant $|E_z|$ component that can be measured by a diode [10]. $|\boldsymbol{H}|$ scatters too much for a suitable sensor calibration. The

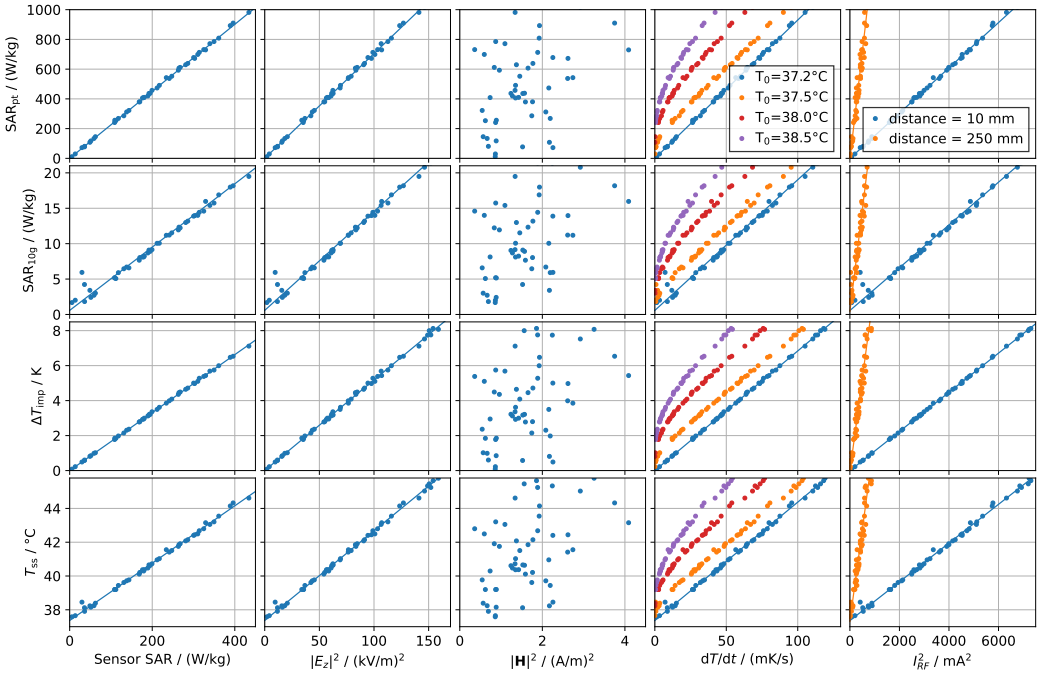

Fig. 5.6: Four implant hazard measures (rows) as function of five implant sensor readings (columns) for 100 random shim vectors scaled to hit the native SCM limit. This figure by Petzold et al. [35] is licenced under CC BY 4.0 and was adapted by using different VOP for the native case.

calibration curve for $\mathrm{d}T/\mathrm{d}t$ depends on the initial temperature. Additional care in the calibration process would therefore be necessary because of multiple temperature-dependent calibration curves as a consequence. The big advantage of this sensor is the direct usability of the thermistor as a safety watch-dog [173]. The RF current sensor is linearly correlated to the hazard measures with lower signal-to-noise ratio (SNR) for higher distances to the implant tip. It must be ensured that the current sensor is placed so that no modes exist that can lead to zero measured current while the tip heating is pathologic [174]. No such modes were found for the investigated implant.

The existence of sensor types that can be calibrated in terms of implant hazard is therefore shown. The point SAR sensor is used in the following as representative of all suitable sensor types.

5.3 Investigation of the B_1^+ optimisation potential

Many RF-shim vectors of the native case must be significantly scaled down to avoid tissue temperatures of more than 39 °C at the implant tip, see Fig. 5.6. This results in a diminished $\mathrm{mean}(B_1^+)$ performance. This section investigates the manifold of the remaining vectors to test for the RF-shim vector optimisation potential and to examine whether the sensor provides enough information to distinguish between safe and unsafe RF-shim vectors for SCM and PCM.

20000 random RF-shim vectors (half with random phase and identical amplitude, half with random phase and random amplitude) were scaled to hit the native case limit and the implant case SAR was evaluated for 2 channels (Fig. 5.7) and 8 channels (Fig. 5.8). Two hazard limits were chosen: $\mathrm{SAR}_{10\,\mathrm{g}} = 10\,\mathrm{W\,kg^{-1}}$ (equivalent to $\Delta T_{\mathrm{imp}} = 3.5\,\mathrm{K}$) following the IEC standard [45] and $\Delta T_{\mathrm{imp}} = 2\,\mathrm{K}$.

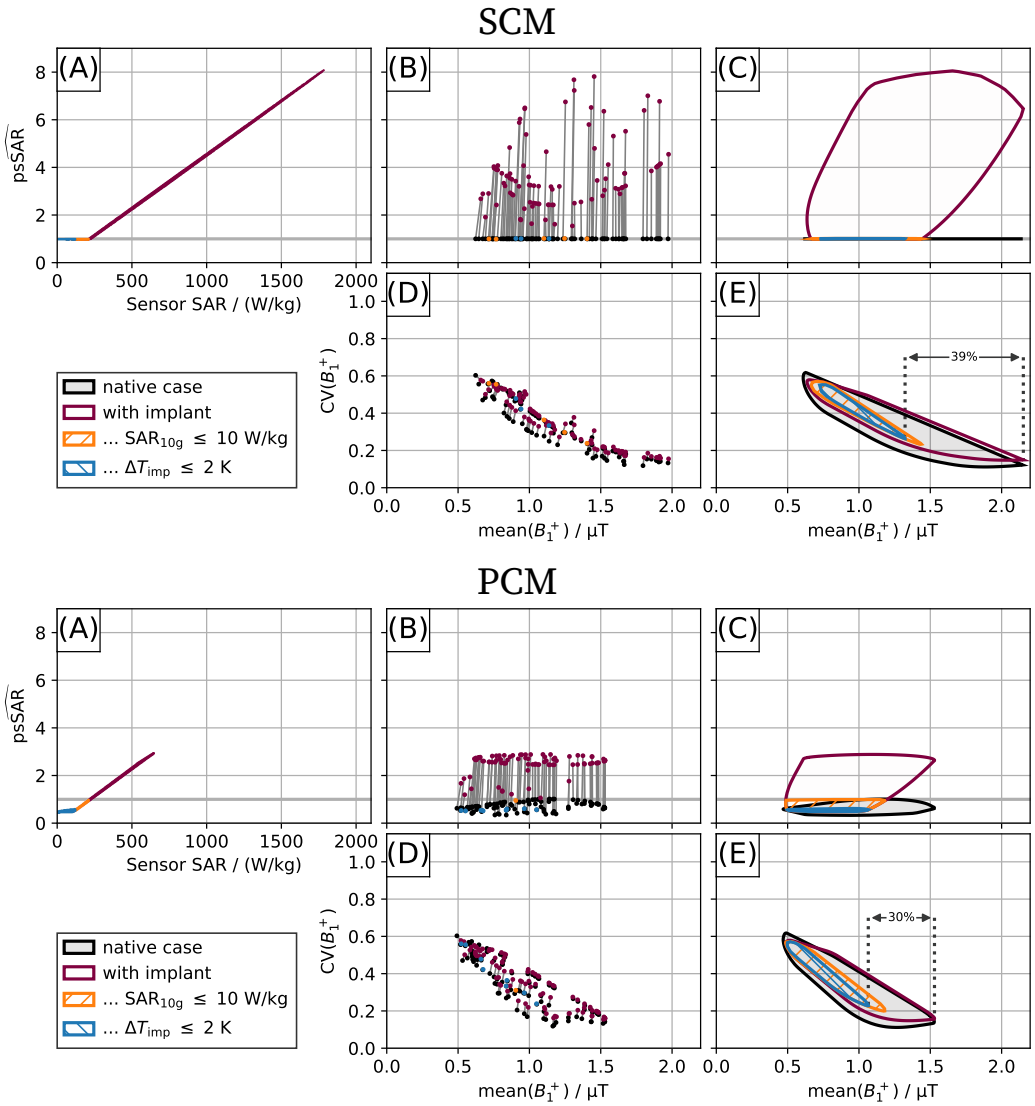

Fig. 5.7: Evaluation of 20000 **2-channel** RF-shim vectors for the implant case that were scaled to hit the native safety limit in terms of $\widehat{\mathrm{psSAR}}$, $\mathrm{mean}(B_1^+)$ and $\mathrm{CV}(B_1^+)$. **Top**: SCM. **Bottom**: PCM. (**A**) $\widehat{\mathrm{psSAR}}$ as function of sensor SAR. Only the calibrated sensor SAR is used to group the shim vectors, see calibration curve in Fig. 5.6. Please note that the limited spread of $\widehat{\mathrm{psSAR}}$ for PCM and $\widehat{\mathrm{psSAR}} < 1$ is caused by the availability of only 2 degrees of freedom. (**B**) $\widehat{\mathrm{psSAR}}$ as function of $\mathrm{mean}(B_1^+)$ of 100 selected shim vectors for native case (black) and implant case (colour). Lines connect the corresponding native and implant values of the same RF-shim vector. (**C**) Convex hull of all 20000 shim vectors as in (B). (**D**) $\mathrm{CV}(B_1^+)$ as function of $\mathrm{mean}(B_1^+)$ of 100 selected shim vectors for native case (black) and implant case (colour). Lines connect the corresponding native and implant values of the same RF-shim vector. (**E**) Convex hull of all 20000 shim vectors as in (D). This figure by Petzold et al. [35] is licenced under CC BY 4.0 and was adapted by using 2-channel data and including PCM.

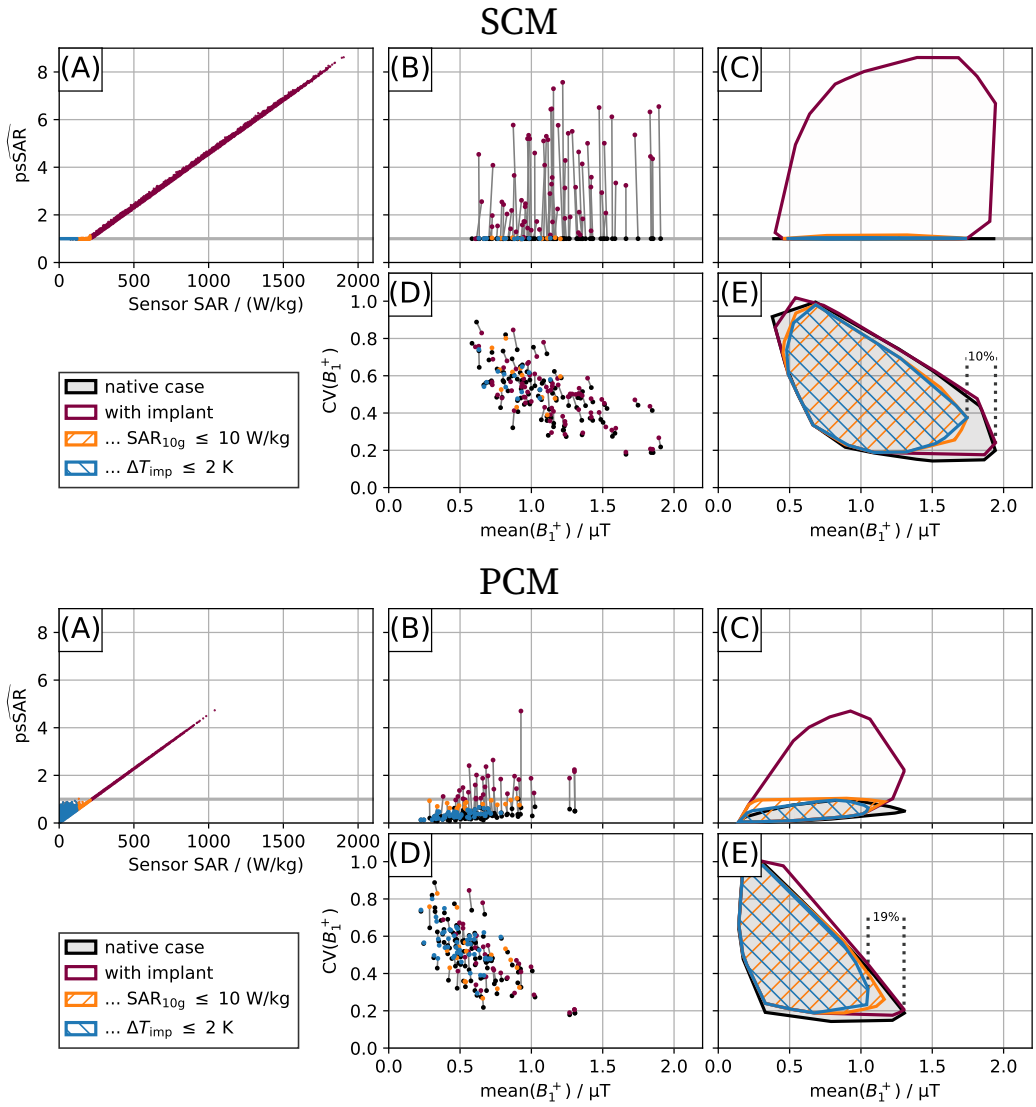

Fig. 5.8: Evaluation of 20000 **8-channel** RF-shim vectors for the implant case that were scaled to hit the native safety limit in terms of $\mathrm{ps\widehat{SAR}}$, $\mathrm{mean}(B_1^+)$ and $\mathrm{CV}(B_1^+)$. **Top**: SCM. **Bottom**: PCM. (**A**) $\mathrm{ps\widehat{SAR}}$ as function of sensor SAR. Only the calibrated sensor SAR is used to group the shim vectors, see calibration curve in Fig. 5.6. Please note that $\mathrm{ps\widehat{SAR}} \geq 0.05$ for PCM. (**B**) $\mathrm{ps\widehat{SAR}}$ as function of $\mathrm{mean}(B_1^+)$ of 100 selected shim vectors for native case (black) and implant case (colour). Lines connect the corresponding native and implant values of the same RF-shim vector. (**C**) Convex hull of all 20000 shim vectors as in (B). (**D**) $\mathrm{CV}(B_1^+)$ as function of $\mathrm{mean}(B_1^+)$ of 100 selected shim vectors for native case (black) and implant case (colour). Lines connect the corresponding native and implant values of the same RF-shim vector. (**E**) Convex hull of all 20000 shim vectors as in (D). This figure by Petzold et al. [35] is licenced under CC BY 4.0 and was adapted by including PCM.

The $\widehat{\mathrm{psSAR}}$ vs. sensor-SAR curve (panel A of Figs. 5.7 and 5.8) has the upper limit $\widehat{\mathrm{psSAR}} = 1$ until the predefined hazard limit for the sensor signal of $\mathrm{SAR}_{10\,\mathrm{g}} = 10\,\mathrm{W\,kg^{-1}}$ is reached. This behaviour occurs for both, SCM and PCM and all channel counts. While the curve stays at $\widehat{\mathrm{psSAR}} = 1$ for SCM by construction, it fans out for PCM and can, in principle, assume all values between 0 and 1. This is because PCM is conservative and certain excitation vectors hit the PCM limit before their actual $\widehat{\mathrm{psSAR}}$ reaches a value of 1.

A linear increase of $\widehat{\mathrm{psSAR}}$ following the sensor calibration curve (Fig. 5.6) is visible for sensor SAR values above the $\mathrm{SAR}_{10\,\mathrm{g}} = 10\,\mathrm{W\,kg^{-1}}$ limit for both SCM and PCM. The sensor is therefore able to completely describe the single hot spot in the patient when the implant is added and $\widehat{\mathrm{psSAR}} > 1$ is caused by the implant hot spot alone.

The higher conservativeness of PCM compared to SCM can be seen when comparing the maximum $\widehat{\mathrm{psSAR}}$ values that reach 8 for SCM but only 5 and 3 for PCM for 8 channels and 2 channels, respectively. The maximum found $\widehat{\mathrm{psSAR}}$ of 8.5 for SCM at 8 channels was higher than the value of 7 that emerged in the hot spot location analysis of Fig. 5.3. This is explained by the absence of a theoretical limit for SCM and more (10^6 vs. 411) RF-shim vectors that were evaluated and increased the likelihood to find a vector closer to the extremes.

$\widehat{\mathrm{psSAR}}$ as function of $\mathrm{mean}(B_1^+)$ is shown in panels B for 100 RF-shim vectors, and panels C for the convex hull of all 20000 RF-shim vectors. Panels D and E show $\mathrm{CV}(B_1^+)$ as function of $\mathrm{mean}(B_1^+)$ for the 100 RF-shim vectors and the convex hulls of all 20000 RF-shim vectors, respectively. $\mathrm{CV}(B_1^+)$ and $\mathrm{mean}(B_1^+)$ show little difference between native case and implant case as they are based on the whole torso in the image plane and the implant is only changing a minor area. $\widehat{\mathrm{psSAR}}$, on the other hand, is strongly influenced by the implant.

Maximum $\mathrm{mean}(B_1^+)$ for native case (black) and with strictest implant limit $\Delta T_{\mathrm{imp}} = 2\,\mathrm{K}$ (blue) in panels E have a difference of 10 %/19 % for 8 channels and SCM/PCM, showing a good potential for optimisation. The gap is with 39 %/30 % higher for 2 channels and SCM/PCM indicating a significantly reduced optimisation potential.

It is, in conclusion, possible to use a sensor at the implant tip for an instantaneous assessment of the tip heating hazard. The anchor-target analysis showed that there is a higher potential for high $\mathrm{mean}(B_1^+)$ shims for higher channel counts due to their higher count of degrees of freedom.

5.4 B_1^+-Optimisation with known digital patient model

Optimisations of $\mathrm{mean}(B_1^+)$ and $\mathrm{CV}(B_1^+)$ were carried out for the combination of the native case with SCM and five implant sensor limits, see Fig. 5.9:

- a very low limit to test the pTx performance of $\Delta T_{\mathrm{imp}} \leq 0.01\,\mathrm{K}$,
- a low limit that could be suitable for critical patients of $\Delta T_{\mathrm{imp}} \leq 0.1\,\mathrm{K}$,
- two limits that are surmisable for general patients of $\Delta T_{\mathrm{imp}} \leq 1\,\mathrm{K}$ as well as $\Delta T_{\mathrm{imp}} \leq 2\,\mathrm{K}$, and
- a local SAR limit based on the IEC limits [45] of tip $\mathrm{SAR}_{10\,\mathrm{g}} \leq 10\,\mathrm{W\,kg^{-1}}$ that corresponds to $\Delta T_{\mathrm{imp}} \leq 3.5\,\mathrm{K}$ for this specific case, see Fig. 5.6.

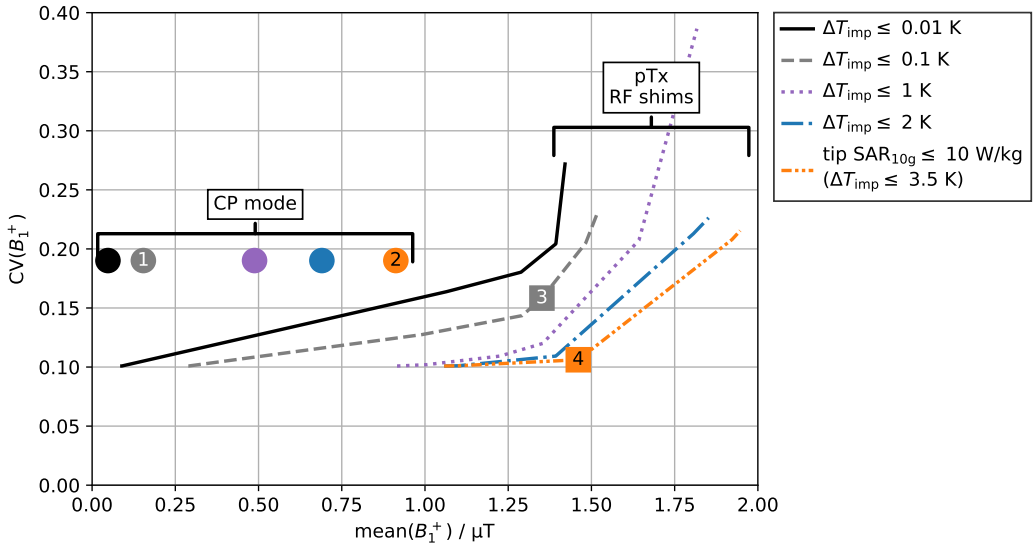

Fig. 5.9: Trade-off between $\mathrm{CV}(B_1^+)$ and $\mathrm{mean}(B_1^+)$ for SCM with a spinal chord mock implant at 8 channels, 3 T. Shim vectors marked with numbers 1-4 are displayed in Fig. 5.10. This figure by Petzold et al. [35] is licenced under CC BY 4.0 and was adapted by adjusting the line styles.

The pTx optimised RF-shims with the strictest implant limit of $\Delta T_{\mathrm{imp}} = 0.01\,\mathrm{K}$ show a higher $\mathrm{mean}(B_1^+)$ than the CP mode with the most lenient limit of $\Delta T_{\mathrm{imp}} = 3.5\,\mathrm{K}$, which demonstrates the advantage of pTx. The $\mathrm{mean}(B_1^+)$ of the CP mode scales with $\sqrt{\mathrm{SAR}} \propto \sqrt{\Delta T_{\mathrm{imp}}}$ resulting in a high $\mathrm{mean}(B_1^+)$ drop for stricter limits while the pTx optimisations lose less $\mathrm{mean}(B_1^+)$ due

to the available degrees of freedom. The pTx RF-shims can reach half of the CP mode's $\mathrm{CV}(B_1^+)$.

The shim vectors marked with numbers are shown in Fig. 5.10.

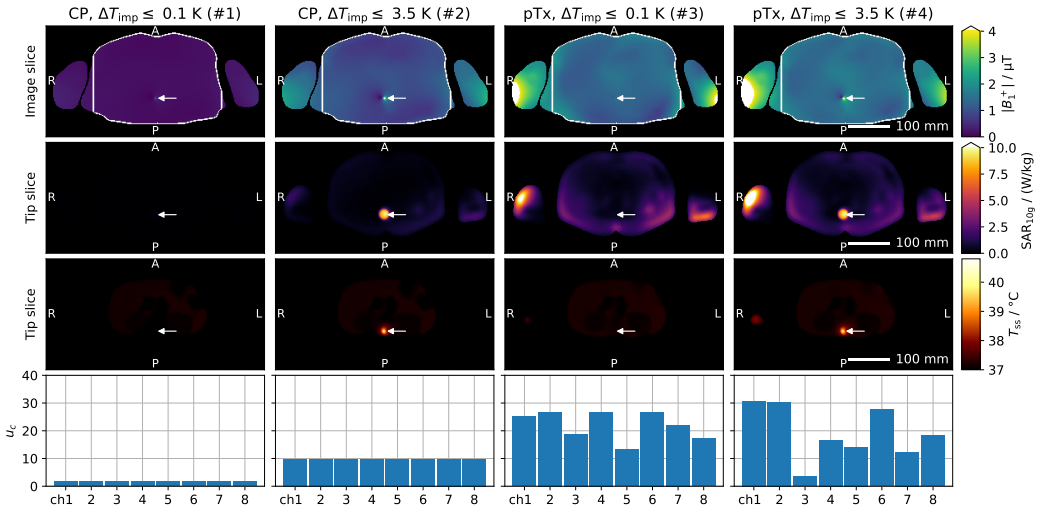

Fig. 5.10: Example shims for CP mode and pTx optimisation for implant tip limits $\Delta T_{\mathrm{imp}} \leq 3.5\,\mathrm{K}$ corresponding to $\mathrm{SAR}_{10\mathrm{g}} \leq 10\,\mathrm{W\,kg^{-1}}$ and $\Delta T_{\mathrm{imp}} \leq 0.1\,\mathrm{K}$, see with numbers marked positions in Fig. 5.9. $|B_1^+|$ is shown in the image slice, SAR and steady state temperature T_{ss} are shown in the tip slice. The bottom row shows the single channel amplitudes u_c of the respective shim vector. This figure by Petzold et al. [35] is licenced under CC BY 4.0 and was adapted by using different VOPs.

The pTx shims show an up to 18-times higher single channel amplitude for the strict temperature limit (#1 vs. #3) and a 3-times higher single channel amplitude for the lenient SAR limit (#2 vs #4). This results in a 7-fold increased $\mathrm{mean}(B_1^+)$ and better B_1^+ homogeneity compared to the CP mode with the strict limit where no temperature hot spot is visible for both cases. The $\mathrm{SAR}_{10\mathrm{g}} = 10\,\mathrm{W\,kg^{-1}}$ hazard limit results for both CP mode (#2) and pTx optimisation (#4) in a hot spot of nearly 41 °C at the implant tip and may thus be considered too lenient.

The optimisation can also account for additional limits like a single channel amplitude limit which is caused by the hardware in all MR scanners. In Fig. 5.11, the single channel voltage was limited by $U_c = 20\,\mathrm{V}$[1] for demonstration purposes. This results in 15 % lower $\mathrm{mean}(B_1^+)$ for the pTx shims for the same $\mathrm{CV}(B_1^+)$ as the CP mode, while the CP mode is not affected as the implant limit is dominating.

[1]The port voltage with 4 ports per element is 20 V. It is not possible to directly infer the transmit voltage.

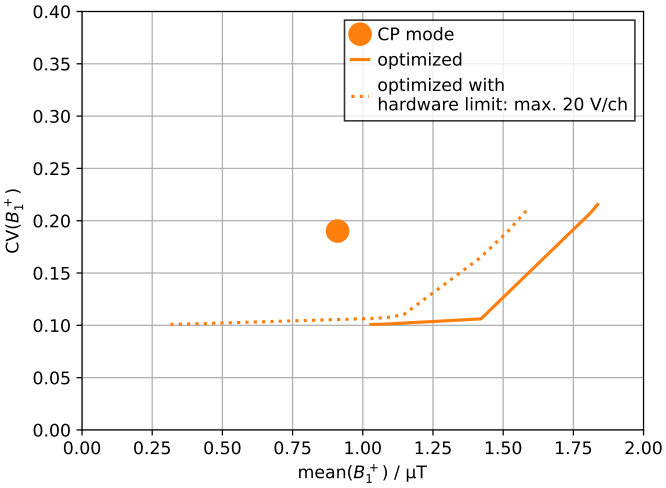

Fig. 5.11: (**A**) Trade-off between $\mathrm{CV}(B_1^+)$ and $\mathrm{mean}(B_1^+)$ for SCM, implant tip limit $\mathrm{SAR}_{10g} \leq 10\,\mathrm{W\,kg^{-1}}$ and with additional hardware limit $u_c \leq 20$. This figure by Petzold et al. [35] is licenced under CC BY 4.0 and was adapted by using a different hardware limit.

It is, in conclusion, possible to use the calibrated sensor signal, the native safety limit and channel wise B_1^+ maps to achieve RF-shims with high $\mathrm{mean}(B_1^+)$, low $\mathrm{CV}(B_1^+)$, native safety and implant safety.

5.5 B_1^+-Optimisation accounting for an unknown patient model

This sections combines the implant safety concept with the native safety mitigation for unknown patient models, see Chapter 4. The $\mathrm{mean}(B_1^+)$ and $\mathrm{CV}(B_1^+)$ were optimised for model Duke with the spinal cord dummy implant and implant-caused temperature rise limits of $\Delta T_{\mathrm{imp}} = 1\,\mathrm{K}$ and $2\,\mathrm{K}$. Different to the previous section is the native safety limit where the knowledge of the exact digital model with SCM is no longer assumed and the limit is derived from the combined native safety limits of the 7 models between 50 – 80 kg with the safety factor derived from the 6-anchor-to-1-target analysis to adjust for unknown patient models instead.

The optimisation was carried out for the native limits SCM, PASCM and PCM, for 0.5 T, 1.5 T and 3 T and for channel counts 1, 2, 4, 8 and 16. A second set of optimisation was carried out for the native case without implant to assess the $\mathrm{mean}(B_1^+)$ impact of the implant. The trade-offs between $\mathrm{mean}(B_1^+)$ and $\mathrm{CV}(B_1^+)$ are shown in Fig. 5.12.

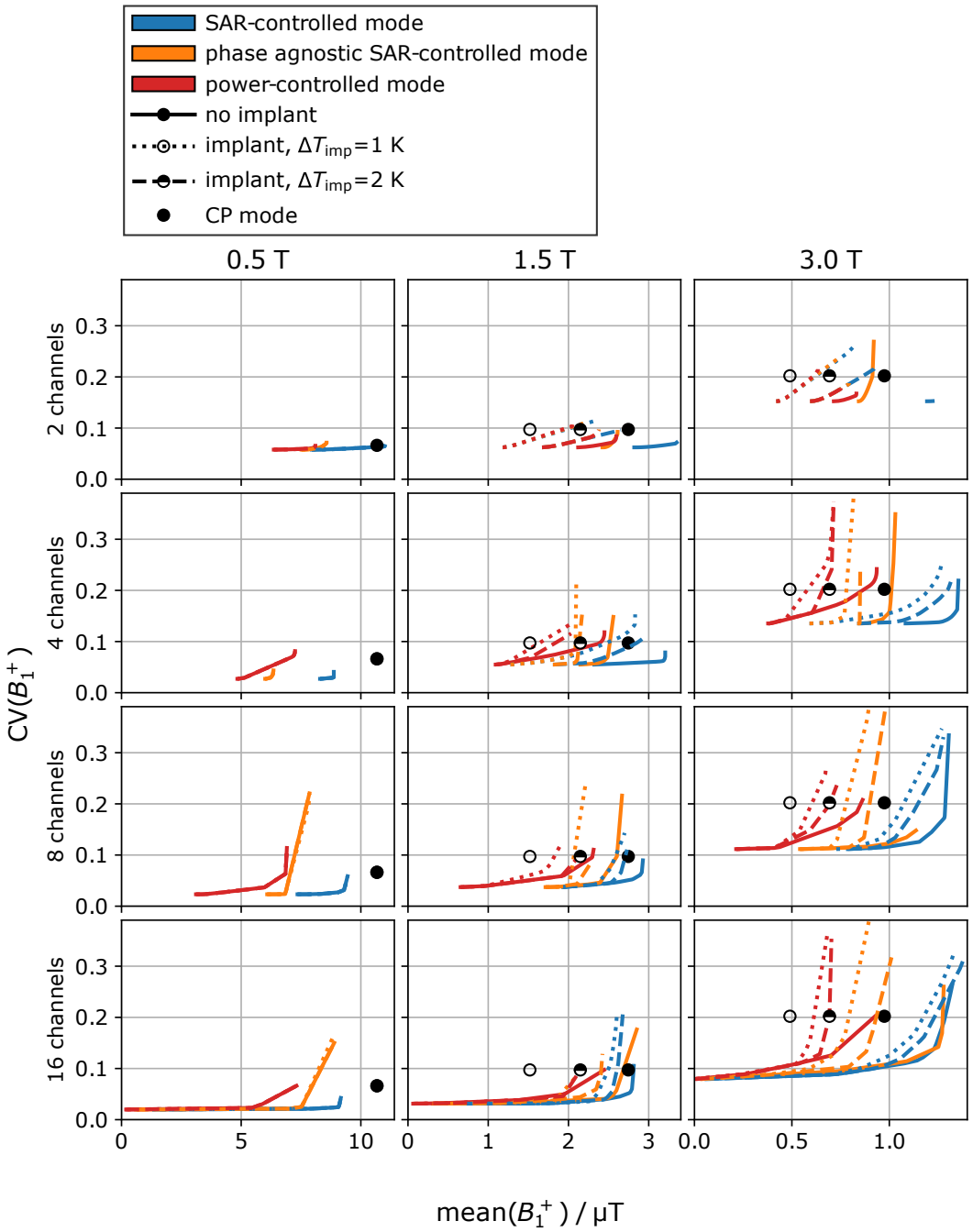

Fig. 5.12: Trade-off between $\mathrm{CV}(B_1^+)$ and $\mathrm{mean}(B_1^+)$ for SCM, PASCM and PCM based on the anchor-target analysis with 7 models, see Fig. 4.20. With implant (limits: $\Delta T_{\mathrm{imp}} \leq 2\,\mathrm{K}$, dashed; $\Delta T_{\mathrm{imp}} \leq 1\,\mathrm{K}$, dotted) and without implant (solid).

It is noticeable that there is only a minimal difference in $\mathrm{mean}(B_1^+)$ between native case and implant case for 0.5 T. Increasing the channel count furthermore leads to a lower $\mathrm{mean}(B_1^+)$ compared to the CP mode. It can therefore be concluded that the tested implant is safe for 0.5 T in this specific position, and the CP mode fulfilling the local SAR limits is sufficient to achieve patient safety. A decreasing B_0 leads for the native case without implant and the same $\mathrm{mean}(B_1^+)$ in general to a lower SAR [175, 176]. This does, however, not ensure that all possible configurations of the test implant are safe for 0.5 T. In light of this, it might be still considered to integrate a sensor, at least for watch-dog purposes [173].

Reductions in $\mathrm{mean}(B_1^+)$ between native case and implant case are visible for 1.5 T and 3 T for CP mode and pTx optimised RF-shims. The reduction is stronger for the stricter $T_{\mathrm{imp}} = 1\,\mathrm{K}$ hazard limit than for $T_{\mathrm{imp}} = 2\,\mathrm{K}$. Accommodating for the implant affects the CP mode more strongly than the pTx RF-shims because of the fewer degrees of freedom. The 2-channel mode likewise performs worse than 4-16 channels that show only minor differences. This is likely the result of stricter safety factors cancelling the gain of the additional degrees of freedom.

The general performance order of the safety limits for the native case is PCM < PASCM < SCM, as expected from the previous chapter, see Fig. 4.20.

The $\mathrm{mean}(B_1^+)$ of the implant-case with the same homogeneity as the CP mode relative to the $\mathrm{mean}(B_1^+)$ of the CP mode is shown in Fig. 5.13A-C for both hazard limits $\Delta T_{\mathrm{imp}} = 1\,\mathrm{K}$ and $2\,\mathrm{K}$. The values above unity signal that pTx is advantageous compared to the CP mode.

The $\mathrm{mean}(B_1^+)$ quotient of $\Delta T_{\mathrm{imp}} = 1\,\mathrm{K}$ and $2\,\mathrm{K}$ for the homogeneity of the CP mode is shown in Fig. 5.13D-F. A value of $\sqrt{2}$ represents the case where only the implant is limiting $\mathrm{mean}(B_1^+)$ and the native limit is not relevant. A value of 1 represents, in contrast, the case where only the native limit is limiting $\mathrm{mean}(B_1^+)$ and a more lenient implant hazard limit would not improve $\mathrm{mean}(B_1^+)$ at all.

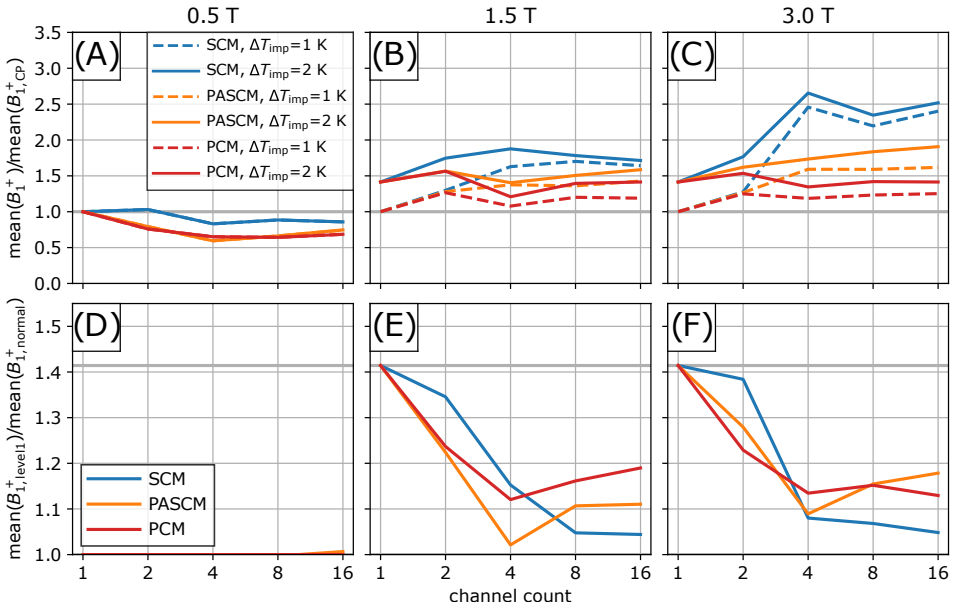

Fig. 5.13: Comparison of $\mathrm{mean}(B_1^+)$ for pTx optimised implant shims for the same $\mathrm{CV}(B_1^+)$ as the CP mode. (**A-C**): $\mathrm{mean}(B_1^+)$ relative to the $\mathrm{mean}(B_1^+)$ of the CP normal mode. (**D-F**): $\mathrm{mean}(B_1^+)$ quotient at the same $\mathrm{CV}(B_1^+)$ as the CP mode of the implant case with hazard limits $\Delta T_{\mathrm{imp}} = 1\,\mathrm{K}$ and $2\,\mathrm{K}$.

No effect of the implant can be seen for 0.5 T.

The additional degrees of freedom of the pTx system offer substantial benefit for 1.5 T and 3 T with up to 2.5 times more $\mathrm{mean}(B_1^+)$ than the CP mode for 3 T at 16 channels with $\Delta T_{\mathrm{imp}} = 2\,\mathrm{K}$, SCM while PASCM and PCM increase the available $\mathrm{mean}(B_1^+)$ by 1.9 and 1.4, respectively, see Fig. 5.13C.

The $\mathrm{mean}(B_1^+)$ quotient of both hazard limits is decreasing with channel count for both 1.5 T and 3 T from $\sqrt{2}$ at one channel to approximately 1.1 at 4 channels, showing that 4 channels are necessary for this specific case to harvest the full $\mathrm{mean}(B_1^+)$ potential of the more strict hazard limit.

The usage of pTx is, in conclusion, beneficial if the same local SAR limits are used, both for CP mode and pTx. There was no additional $\mathrm{mean}(B_1^+)$ advantage of pTx for 0.5 T for the tested implant, in contrast to 1.5 T and 3 T where an improvement of $\mathrm{mean}(B_1^+)$ can be achieved with pTx. A high enough count of channels is necessary to harvest the full pTx potential. A channel count of at least 4 would be recommended for the tested case. The $\mathrm{mean}(B_1^+)$ advantage of SCM over PASCM below 30 % for 3 T and 10 % for 1.5 T for the tested implant configuration might be not worth the added complexity of incorporating phase information. This decision has to be taken by the MR system manufacturer for the actual coil geometry and must be based on more simulated implant cases.

6 A sensor calibration strategy for implant manufacturers

The implant sensor was until now positioned in the critical region at the implant tip to test the feasibility of the implant safety concept as this location provides the most valuable information about the implant hazard [10, 26, 177]. The design of new implant leads with integrated sensors might be not straightforward because the sensor placement might antagonise other design constraints like material, size or clearance around the electrode.

This chapter therefore takes a different approach requiring fewer constraints for the implant design: One-dimensional implants are designed to transmit signals between implantable pulse generator (IPG) and the tip of the lead. All RF signals that are captured by the tip are therefore transmitted to the IPG, where a filter is generally available that protects the electronic components from the RF influence. This chapter investigates the possibility to instead use the RF signal at the other end of a coaxial cable as hazard measure. A coaxial cable is very suitable for this purpose, as interferences along the cable are shielded.

The feasibility to use a voltage sensor at the IPG end of pre-existing coaxial leads [178, 179] is tested for the dummy implant of a coaxial cable with uninsulated tip. Such a sensor could be integrated into the IPG [27] where less constraints apply and communicate with the MRI scanner trough standardised communication protocols like Bluetooth [26].

A prerequisite for the feasibility of such sensors is the RF-shim-vector-stability and trajectory-stability of the sensor signal, meaning that the correlation between sensor signal and hazard measure should be independent of RF-shim vector and implant lead trajectory. These prerequisites were tested by an experiment.

The sensor signal must furthermore be calibrated so that it correlates with the actual worst case hazard measure and not just with the hazard measure at a single position. Simulations were carried out for this purpose in a second step.

Parts of this chapter were published in a conference abstract [94], one journal paper by Petzold et al. [35] and one journal paper by Silemek et al. [27].

6.1 Calibration of a remote sensor

A 7 T (297 MHz) pTx testbed [90] was used for the experiments. A cylinder PVP/water phantom (radius: 100 mm, height: 198 mm, relative permittivity $\varepsilon_r = 43.8$, electrical conductivity $\sigma = 0.35\,\mathrm{S\,m^{-1}}$) was placed in the 7 T 8-channel head coil [180].

A semi-rigid coaxial cable (SUCOFORM_141_CU_FEP, Huber+Suhner AG, Herisau, Switzerland, 12 mm of shield at tip uninsulated, 5 mm extended inner conductor) acts as mock implant and was bent into a loop to pick up RF-current from multiple channels on the outer conductor, see Fig. 6.1A. The radial E-field and the temperature near the coaxial cable tip were measured by two probes (E1TDSz SNI, SPEAG, Zürich, Switzerland; respective FBG/FBG-TEMP-XXS with controller CANFDX/L-FBG-T8, imc Test & Measurement GmbH, Berlin, Germany) with the loop being submerged into the phantom so that its tip rested 15 mm below the liquid surface, see Fig. 6.1B. The voltage between inner and outer conductor (the 'sensor signal') was measured outside of the RF coil by the testbed's analog-to-digital converter (ADC).

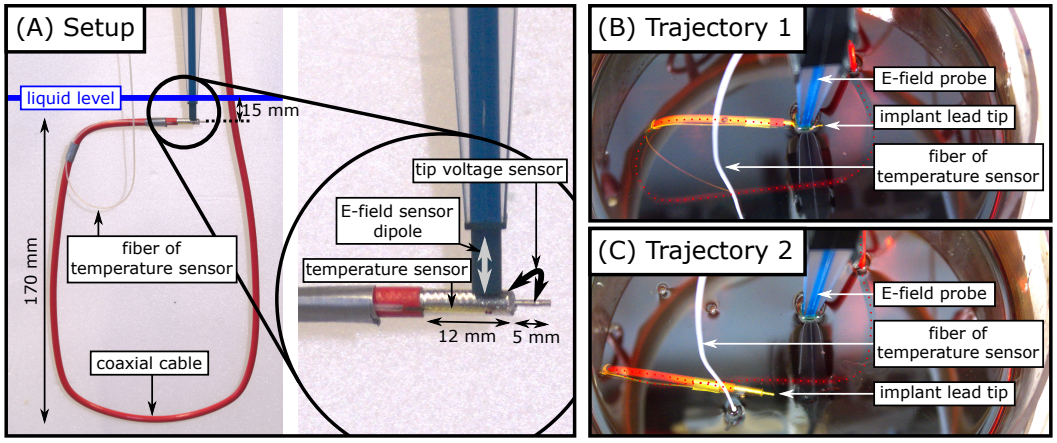

Fig. 6.1: Experimental setup to correlate implant tip heating with E-field and tip temperature. (**A**) A semi-rigid coaxial cable with uninsulated tip is bent into a loop. A fibre-optical temperature sensor is attached to the tip. An E-field sensor is positioned to be close to the tip (see zoom). (**B**) Trajectory 1 in the PVP/water phantom and 8-channel head coil. (**C**) Trajectory 2 where the tip was bent approximately 50 mm. This figure by Petzold et al. [35] is licenced under CC BY 4.0 and was adapted by rearranging the panels.

Radial E-field and sensor signal were measured for 1000 RF shim vector pulses with random phase and amplitude with maximum single channel amplitude of 0.55 V and 100 µs duration each, see Fig. 6.2A. The maximum

voltage was chosen to avoid saturation effects of the E-field probe.

Temperature and sensor signal were measured for 10 RF-shim vectors that were selected from the 1000 previous shim vectors so that they are spaced approximately equidistant over the span of possible sensor signals.[1] These selected RF-shim vectors were scaled by factor 5 to 2.75 V maximum single channel amplitude for an increased SNR of the temperature measurements with 60 s duration each, see Fig. 6.2B-E.

The heating experiments were repeated for trajectory 2 where the implant's tip was bent 50 mm away from the E-field probe to test for trajectory-stability, see Fig. 6.1C.

There is a good linear correlation between sensor signal and radial E-field with Pearson $r = 0.97$ for trajectory 1. This indicates that the calibration is independent of the chosen shim vector. Temperature and sensor signal are linearly correlated with $r = 0.99$ for the measurements of both trajectories, indicating that the calibration curve is independent of lead trajectory as well.

A baseline temperature drift can be observed for the temperature evolution curve of Fig. 6.2C. The temperature rise curve where the mean temperature in the 5 s before heating starts was subtracted is shown in Fig. 6.2D. The curve of shim vector 10 stays the same despite 0.5 K higher baseline temperature for the repetition showing a good linearity for the phantom. The normalised temperature curves where the mean temperature between 58 s and 62 s was additionally set to 1 is shown in Fig. 6.2E. All shim vectors except for #1 (not shown) with the lowest temperature rise show a similar time course additionally showing the linearity of the system.

[1] *I wish to thank Dr. Rüdiger Brühl for providing his temperature sensor measurement recording scripts and assistance with the temperature measurements.*

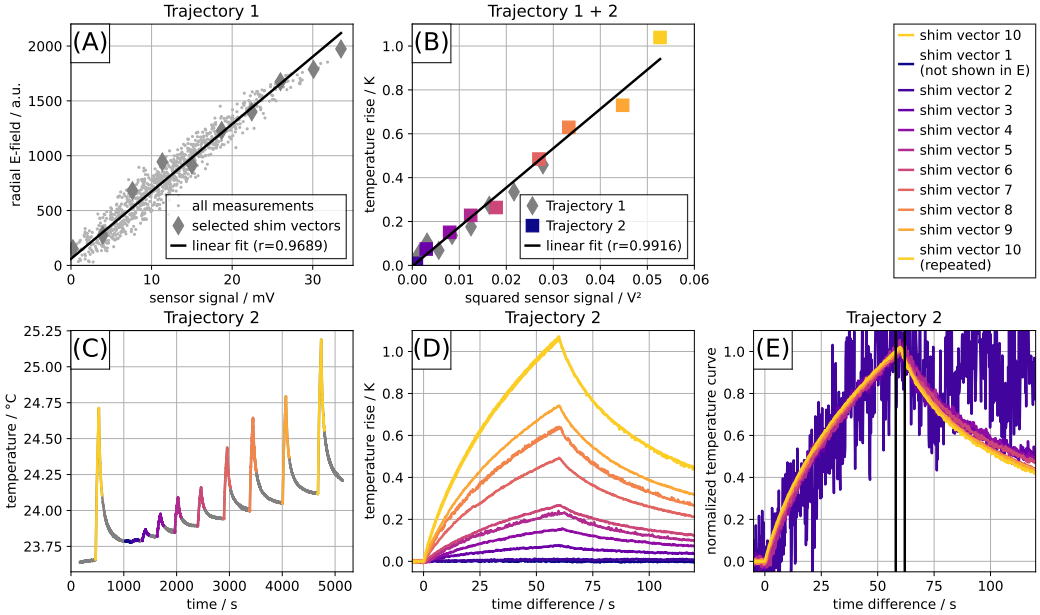

Fig. 6.2: Measurements from the implant tip sensor calibration setup. (**A**) Radial E-field as function of sensor signal for 1000 random shim vectors with maximum single channel amplitude 0.55 V and implant trajectory 1. 10 vectors spread over all possible sensor signal are marked with diamonds. A beginning saturation of the E-field sensor is visible above 1500 E-field units. (**B**) Temperature difference as function of squared sensor signal for trajectory 1 and 2. 10 shim vectors with maximum single channel amplitude 2.75 V each. The shim vectors of trajectory 1 marked with grey diamonds correspond to the measurements of panel A. The colour coded square shim vectors of trajectory 2 correspond to the temperature curves of panels C-E. (**C**) Temperature as a function of time for the complete heating experiment of trajectory 2. (**D**) Temperature difference as function of time difference of all tested shim vectors of trajectory 2. (**E**) Normalised temperature curves as function of time difference of trajectory 2. Shim vector 1 is not shown. Adopted from [35, 94].

6.2 Hazard determination near implant tips

The indicated RF-shim-vector-stability and trajectory-stability allow to simplify the simulation by only focusing on the implant tip and excite the implant directly without intermediate RF coil. A isotropic spatial resolution of 100 µm was used for the EM FDTD- and thermal simulation of a $44\,\mathrm{mm} \times 44\,\mathrm{mm} \times 74\,\mathrm{mm}$ region around the coaxial cable tip in a rectangular PVP/water phantom (relative permittivity $\varepsilon_r = 43.8$, electrical conductivity $\sigma = 0.35\,\mathrm{S\,m^{-1}}$, thermal conductivity $0.1\,\mathrm{W\,m^{-1}\,K^{-1}}$ [157]), see Fig. 6.3.

The implant tip was excited by a voltage source between outer conductor and a ground plane at the remote end of the coaxial cable, to reduce the

background SAR level at the lead tip and minimise the simulation space for lower computational load. The voltage across a 50 Ω resistor between inner conductor and outer conductor was recorded.

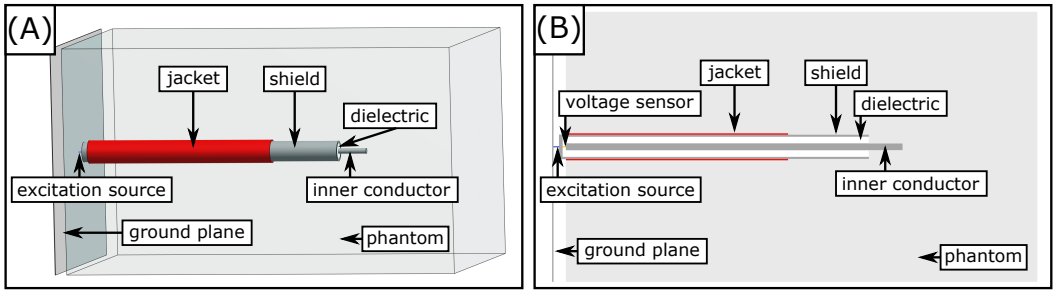

Fig. 6.3: Simulation setup to correlate voltage between core and shield of the coaxial cable with tip temperature. (**A**) 3D view of coaxial cable. (**B**) Cross section through the coaxial cable. Adapted from [94].

SAR hotspots are found at the end of the tip and the edges of the outer conductor, see Fig. 6.4.

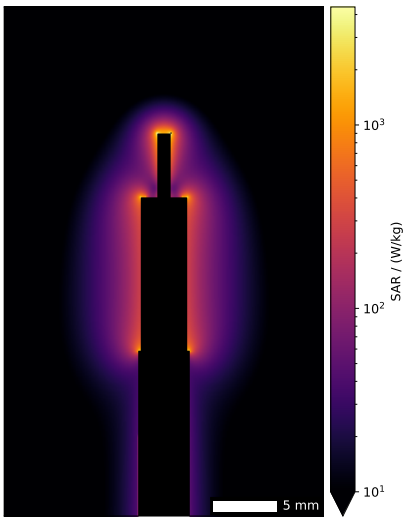

Fig. 6.4: Simulated coaxial tip SAR. Please note the logarithmic scale. From [94].

The thermal simulations with 60 s of heating followed by 60 s of cooling use the electric loss density map of the EM simulation as heat source. The temperature of inner and outer conductor was fixed to the base temperature, as the high heat conductivity of the metal would otherwise require very small time steps resulting in a not feasible computational load.

The temperature curve was scaled with a scalar to qualitatively match

the curve of shim vector #10, see Fig. 6.5A.[2] The distinct advantage of the simulation lies in the possibility to review different spatial positions of the temperature, see Fig. 6.5B,C. A 40 % higher maximum temperature can be found at the tip of the implant compared to the sensor position. The simulation further demonstrated, that the time dependency of the hot spot location after heating stopped needs to be considered for safety assessment.

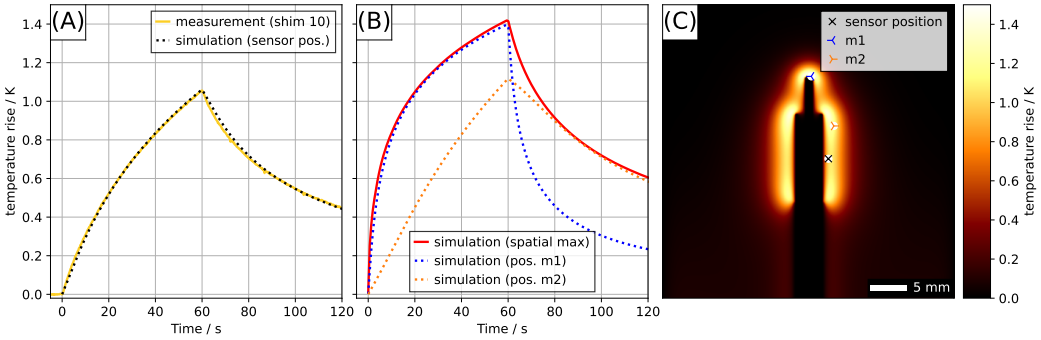

Fig. 6.5: Simulated coaxial tip temperature dynamics. (**A**) Temperature rise as function of time for shim vector #10 and scaled simulated temperature difference. (**B**) Temperature rise as function of time for the spatial maximum (red) and two positions (m1,m2) that show the highest temperature at different given times. (**C**) Temperature rise map after 60 s with marked sensor position. From [94].

It is further possible to review different tissues at the implant tip by means of simulation, see Figs. 6.6 and 6.7. The voltage of the simulated sensor was set to the same value as for the PVP/water phantom and the temperature evolution curves were scaled accordingly for additional simulations with the phantom properties of white matter, grey matter and cerebrospinal fluid.

The maximum spatial temperature evolution of the PVP/water phantom is comparable to the curve of cerebrospinal fluid. The PVP/water phantom could hence be used with an appropriate safety factor for a calibration that is valid for the typical tissues encountered around the tip of a deep brain stimulator.

The described approach combining measurement and simulation can, in summary, be used to investigate implant safety for different implant leads. The simulation is necessary to ensure that the actual patient hazard is correctly reflected in the sensor calibration. The measurements are necessary to validate the simulations.

[2]The cable attenuation alone is not sufficient to explain the difference between measured voltage and simulated voltage in this case. This was not further investigated as the necessary factor to adjust simulation to experiment can be estimated with the temperature curve.

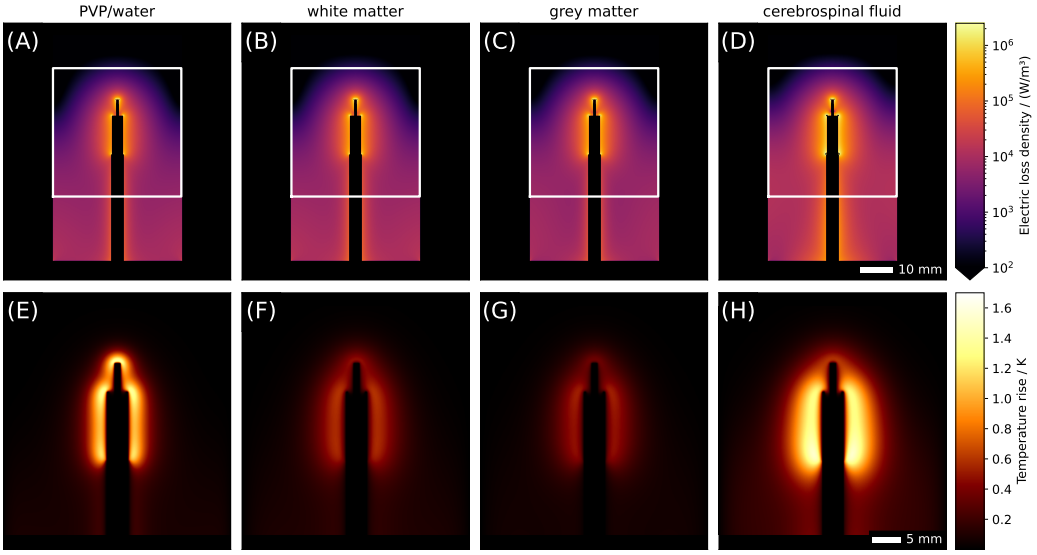

Fig. 6.6: (**A-D**) Electric loss density maps (please note the logarithmic scale) and (**E-H**) temperature rise maps of the central plane trough the implant tip for the four phantom materials PVP/water, white matter, grey matter and cerebrospinal fluid for the same simulated voltage sensor measurement. This figure by Silemek et al. [27] is licenced under CC BY 4.0.

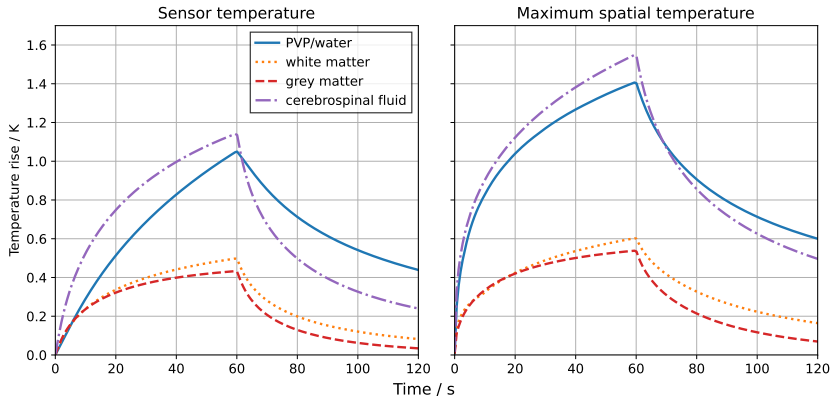

Fig. 6.7: Temperature rise as function of time for the sensor position (left) and the maximum spatial temperature (right) for different simulated phantoms. This figure by Silemek et al. [27] is licenced under CC BY 4.0.

7 Summary

This thesis focused on improving the pTx RF safety for patients in MRI. The native pTx safety of a patient without implant was explored first. It was shown that pTx is advantageous in terms of maximum possible $\mathrm{mean}(B_1^+)$ over the CP mode for the tested birdcage coil at 0.5 T, 1.5 T and 3 T if the same local SAR limits apply to the CP mode that are required for pTx. A channel count of 2 with SCM is able to achieve the best native performance for 0.5 T and 1.5 T with $\mathrm{mean}(B_1^+)$ improvements of up to 30 %. A higher channel count of 16 is required for 3 T to achieve the 1.5 T CP mode B_1^+ homogeneity of $\mathrm{CV}(B_1^+) = 0.1$ for all models. SCM and PASCM have, in this case, a very similar $\mathrm{mean}(B_1^+)$ performance. It was demonstrated that a safety limit for a patient with a position between pre-calculated anchor positions can be inferred from the closest anchors.

The main advantage of pTx emerges when an implant is present and the available degrees of freedom can be exploited to adjust the electromagnetic RF field so that implant-caused heating is minimised while $\mathrm{mean}(B_1^+)$ performance is maintained. The mock implant posed no safety hazard for the tested configuration at 0.5 T. For 1.5 T and 3 T and the very specific tested configuration, a major improvement in $\mathrm{mean}(B_1^+)$ of factor 3 compared to the CP mode can be achieved. This pTx advantage is likely to be situation dependent.

The main contributions to the field include

1. the demonstration how pTx RF safety can be ensured if the uncertainties are properly accounted for arising from the fact that the actual patient's anatomy and position in the scanner are not precisely known,

2. the demonstration of an implant safety concept separating native patient safety and and implant-related safety hazards, and

3. the analysis of the three safety modes SCM, PASCM and PCM in terms of their performance and robustness for native safety and implant safety.

Appendix

A.1 Estimation of the limit mass fraction where whole body SAR and partial body SAR are equally limiting.

The partial body SAR limits l_{pb} is calculated by

$$l_{\mathrm{pb}} = l_{\mathrm{pba}} - l_{\mathrm{pbb}} \frac{m}{M} \tag{A.1}$$

with ratio of patient mass in the effective volume of the coil m and total patient mass M. The fraction m/M where whole body and partial body SAR limits are equally limiting can be roughly estimated by assuming that power P is deposited in the patient. The safety condition of the whole body limit is thereby

$$\frac{P}{M} \leq l_{\mathrm{wb}}. \tag{A.2}$$

Assuming that power rP with $0 \leq r \leq 1$ is deposited in the partial body mass results in the safety condition for partial body SAR

$$\frac{rP}{m} \leq l_{\mathrm{pba}} - l_{\mathrm{pbb}} \frac{m}{M}. \tag{A.3}$$

Setting Eqs. (A.2) and (A.3) equal results in a quadratic equation for m/M with solution

$$\frac{m}{M} = \frac{1}{2} \frac{l_{\mathrm{pba}}}{l_{\mathrm{pbb}}} \pm \sqrt{\frac{1}{4} \frac{l_{\mathrm{pba}}^2}{l_{\mathrm{pbb}}^2} - r \frac{l_{\mathrm{wb}}}{l_{\mathrm{pbb}}}}. \tag{A.4}$$

The '+' solutions are not relevant as $m \leq M$. This results for assumed $r = 0.95$ in $m/M \approx 0.23$ for normal mode ($l_{\mathrm{wb}} = 2\,\mathrm{W\,kg^{-1}}$, $l_{\mathrm{pba}} = 10\,\mathrm{W\,kg^{-1}}$, $l_{\mathrm{pbb}} = 8\,\mathrm{W\,kg^{-1}}$) and $m/M \approx 0.59$ for first level controlled mode ($l_{\mathrm{wb}} = 4\,\mathrm{W\,kg^{-1}}$, $l_{\mathrm{pba}} = 10\,\mathrm{W\,kg^{-1}}$, $l_{\mathrm{pbb}} = 6\,\mathrm{W\,kg^{-1}}$). For body imaging it is hence expected that the whole body SAR is limiting for normal mode while the partial body SAR is limiting for first level controlled mode.

A.2 Derivation of the maximum single channel amplitude limit

The normalised upper limit SAR $\widehat{\mathrm{SAR}}_{\mathrm{max}}$ can be estimated with 1-norm $\|\cdot\|_1$ and supremum norm $\|\cdot\|_\infty$ for each normalised SAR matrix $\hat{\boldsymbol{Q}}$ and arbitrary RF-shim vector $\boldsymbol{u}$ as

$$\begin{aligned}\widehat{\mathrm{SAR}} = |\widehat{\mathrm{SAR}}| &= |\boldsymbol{u}^\dagger \hat{\boldsymbol{Q}} \boldsymbol{u}| \\ &\leq \|\boldsymbol{u}\|_\infty \cdot \|\hat{\boldsymbol{Q}}\boldsymbol{u}\|_1 && \text{Hölder's inequality [138]} \\ &= \|\boldsymbol{u}\|_\infty \cdot \sum_i |(\hat{\boldsymbol{Q}}\boldsymbol{u})_i|. && \text{(A.5)}\end{aligned}$$

For the ith component of vector $\hat{\boldsymbol{Q}}\boldsymbol{u}$ follows

$$\begin{aligned}|(\hat{\boldsymbol{Q}}\boldsymbol{u})_i| &= |\hat{\boldsymbol{Q}}_i, \boldsymbol{u}| \\ &\leq \|\boldsymbol{u}\|_\infty \cdot \|\hat{\boldsymbol{Q}}_i\|_1. && \text{Hölder's inequality} \quad \text{(A.6)}\end{aligned}$$

Combining Eqs. (A.5) and (A.6) results in

$$\begin{aligned}\widehat{\mathrm{SAR}} &\leq \|\boldsymbol{u}\|_\infty \sum_i (\|\boldsymbol{u}\|_\infty \cdot \|\hat{\boldsymbol{Q}}_i\|_1) \\ &= \|\boldsymbol{u}\|_\infty^2 \sum_i \|\hat{\boldsymbol{Q}}_i\|_1 \\ &= \|\boldsymbol{u}\|_\infty^2 \sum_{i,k} |\hat{\boldsymbol{Q}}_{i,k}| \equiv \widehat{\mathrm{SAR}}_{\mathrm{max}}. && \text{(A.7)}\end{aligned}$$

Setting $\widehat{\mathrm{SAR}}_{\mathrm{max}} = 1$, i.e. one SAR value hits the respective IEC limit, results in:

$$\max_c |u_c| = \|\boldsymbol{u}\|_\infty = \frac{1}{\sqrt{\sum_{i,k} |\hat{\boldsymbol{Q}}_{i,k}|}}. \tag{A.8}$$

The maximum allowed amplitude α of all normalised SAR matrices $\hat{\boldsymbol{Q}}^{(j)}$ is therefore

$$\alpha = \min_j \frac{1}{\sqrt{\sum_{i,k} |\hat{\boldsymbol{Q}}^{(j)}_{i,k}|}}. \tag{A.9}$$

Combining Eqs. (A.7) and (A.9) results in the upper limit maximum SAR $\widehat{\mathrm{SAR}}_{\mathrm{max}}$ that a system with single channel amplitude limit α_t can have, if an RF-shim vector with maximum single channel amplitude α_a is used:

$$\widehat{\mathrm{SAR}}_{\mathrm{max}} = \left(\frac{\alpha_a}{\alpha_t}\right)^2 . \tag{A.10}$$

A.3 Avoiding body loops

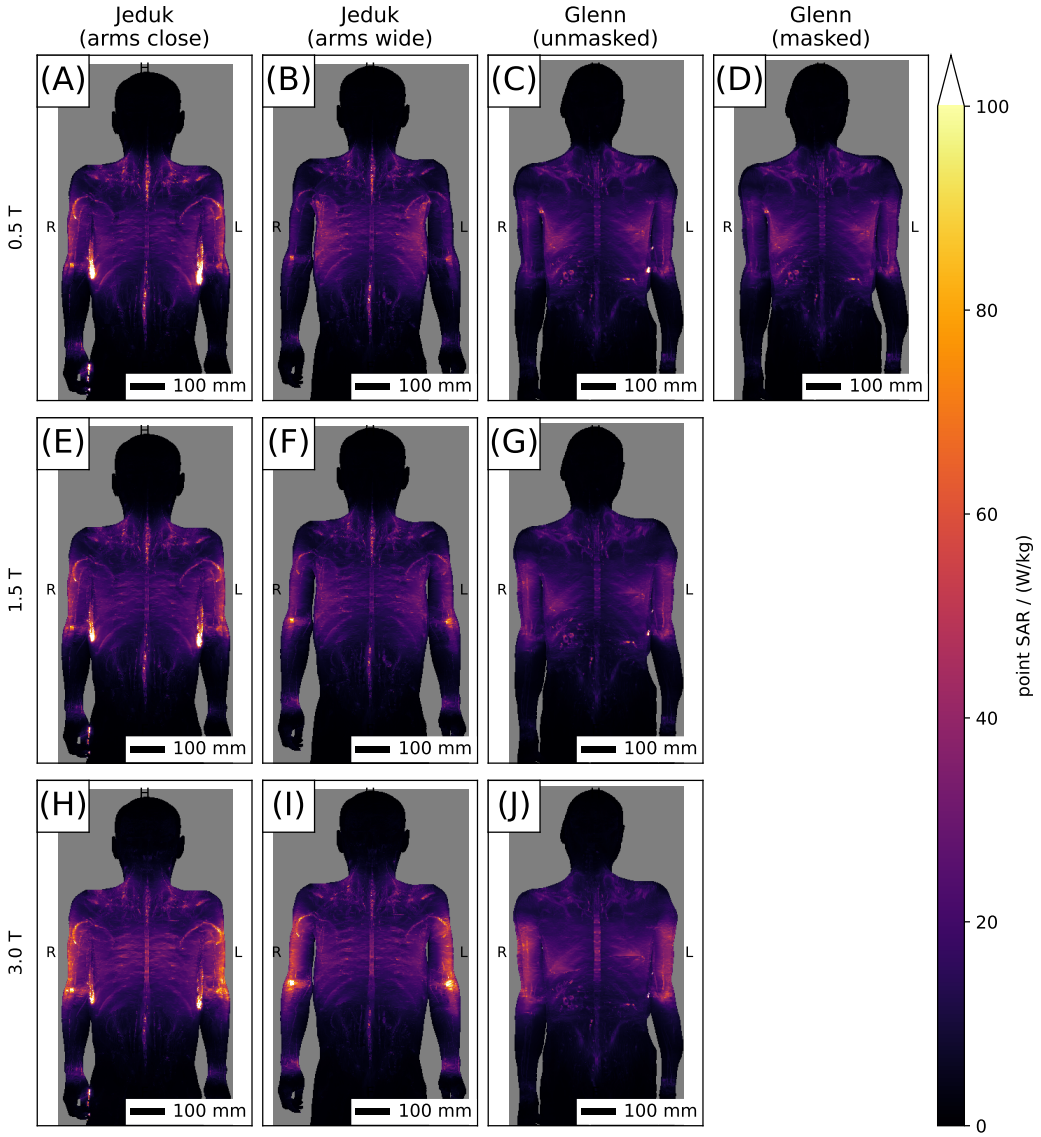

Fig. A.1: Maximum intensity projections of point SAR in models Jeduk with two arm configurations and Glenn. A body loop exists for model Jeduk with closed arms. For model Glenn, the hotspot of the body loop is dominant for 0.5 T in panel (**C**) and fades for higher field strengths. This figure by Petzold et al. [91] is licenced under CC BY 4.0.

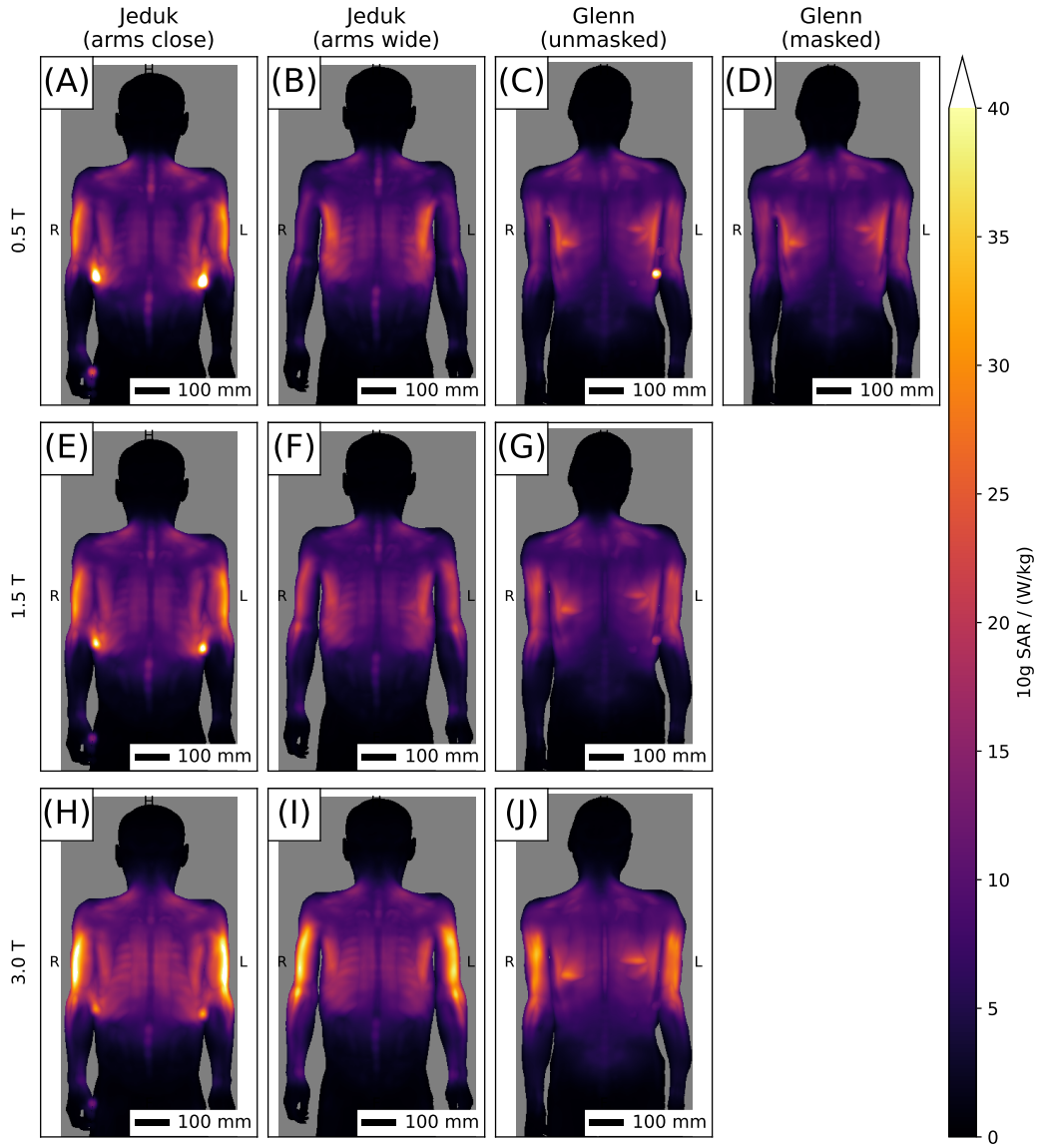

Fig. A.2: Maximum intensity projections of 10 g averaged SAR in models Jeduk with two arm configurations and Glenn. A body loop exists for model Jeduk with closed arms. For model Glenn, the hotspot of the body loop is dominant for 0.5 T in panel (**C**) and fades for higher field strengths. This figure by Petzold et al. [91] is licenced under CC BY 4.0.

A.4 Performance of the native safety limits for all 11 anchor models

The analysis in Section 4.6 was carried out for all 11 human voxel models as well. Fig. A.3 shows, that this selection of models is very heterogeneous with models Eddie (only 0.5 T) and Fats showing the highest $\mathrm{ps}\widehat{\mathrm{SAR}}$ with large margin for 8 and 16 channels. It can therefore be concluded that the other models are not sufficient to predict the local SAR in Fats sufficiently while the local SAR restrictions by Fats are overly conservative. The resulting SCM safety factor of 6 for 16 channels results in significantly lowered $\mathrm{mean}(B_1^+)$ compared to the analysis with 7 models, where a safety factor of 2 was obtained and the overshoots are more uniformly distributed, see Fig. 4.15.

This effect is even more pronounced for a lower number of anchor simulations, see Fig. A.4. A high safety factor above 20 would be required for 16 channels and an anchor model count below 3. The maximum $\mathrm{ps}\widehat{\mathrm{SAR}}$ is limited by the global SAR limit of the target simulation for the low channel counts for SCM, which can be seen, for example, in Fig. A.4o where the first 4 anchor models do not change Fats' $\mathrm{ps}\widehat{\mathrm{SAR}}$.

The $\mathrm{mean}(B_1^+)$ of the optimised pTx RF-shims based on the 11 models is lower than for the 7 model analysis, see Fig. A.5. This is mainly caused by models Fats and Eddie that require higher safety factors for SCM and PASCM and low single channel amplitude limits for PCM. The phase-agnostic safety limits suffer less from the additional models, especially for high channel counts, with the result that PCM outperforms the other modes for 1.5 T and 3 T and 16 channels while PASCM and SCM are comparable.

This shows the importance of the proper selection of a suitable group of human voxel models for the anchor-target analysis, especially for higher pTx channel counts where model differences are of higher relevance.

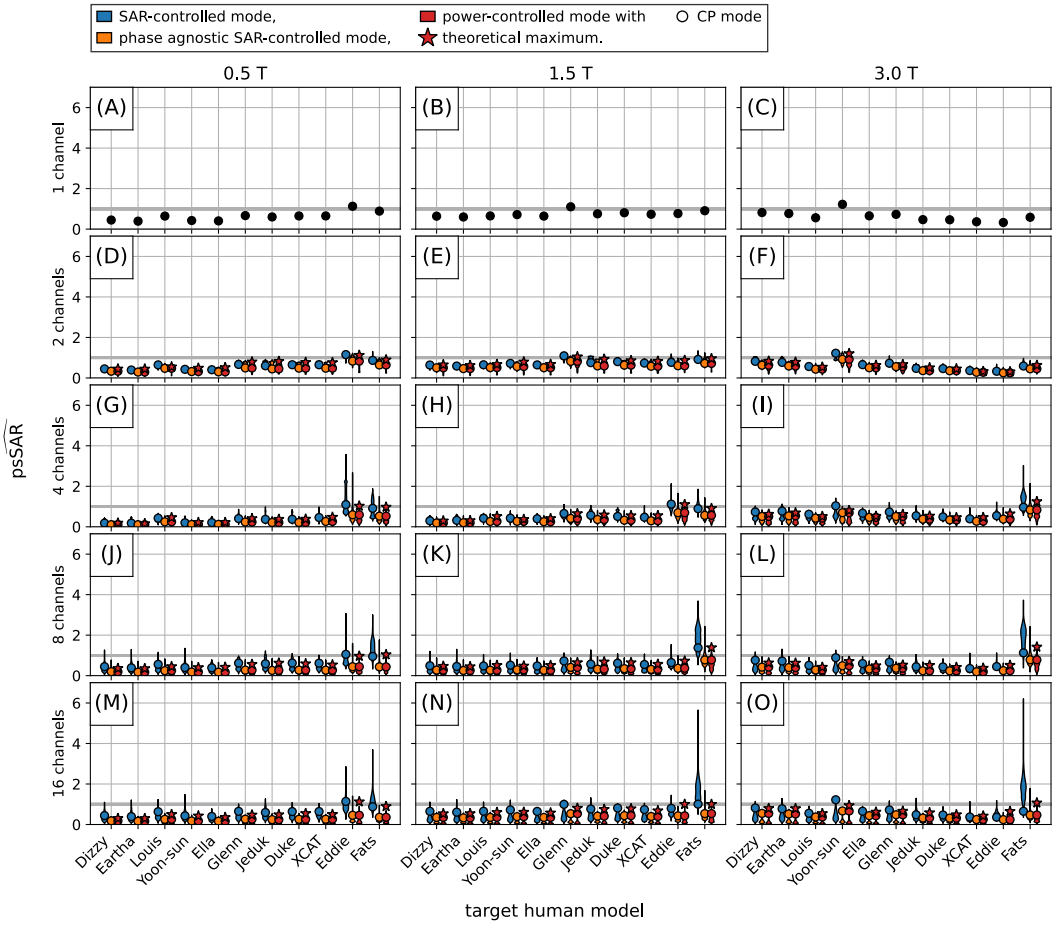

Fig. A.3: $\widehat{\mathrm{psSAR}}$ as function of the target model in an anchor-target analysis with 10^6 random shim vectors scaled to hit the limit of the 10 remaining anchor models.

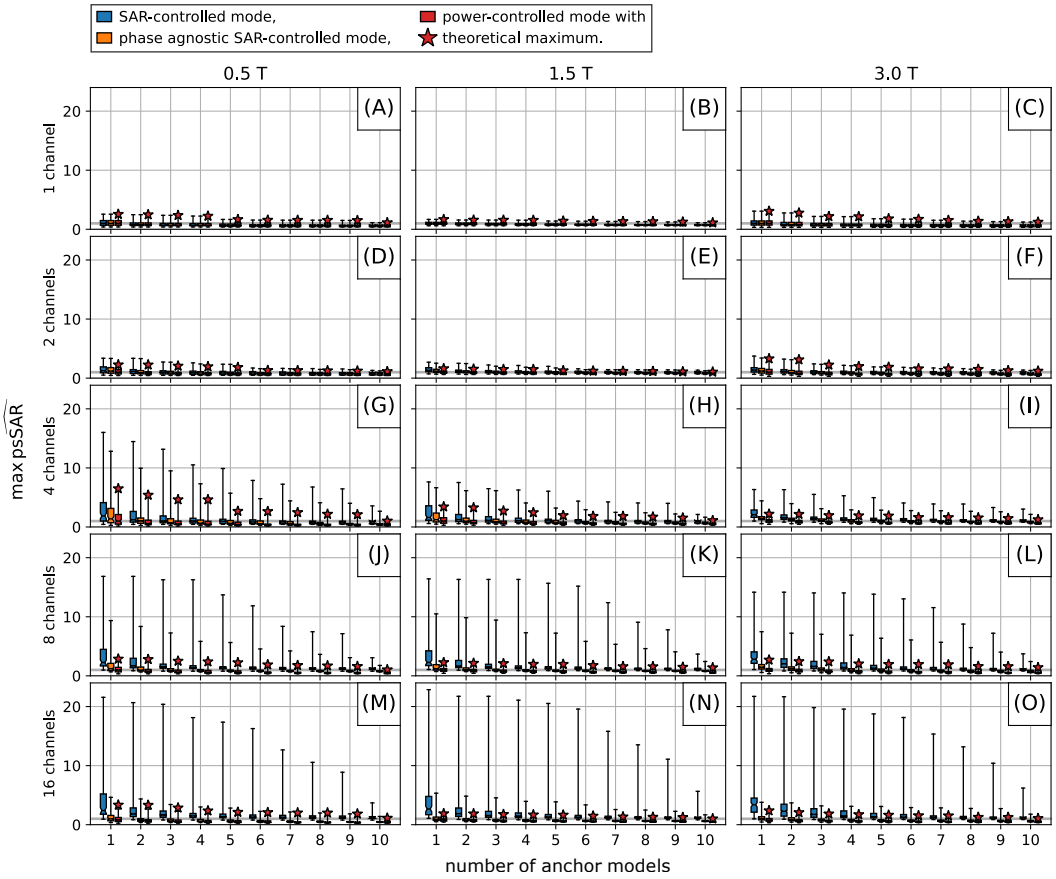

Fig. A.4: Maximum $\widehat{\mathrm{psSAR}}$ as function of anchor model count for all possible combinations of up to 10 anchor-models and target model.

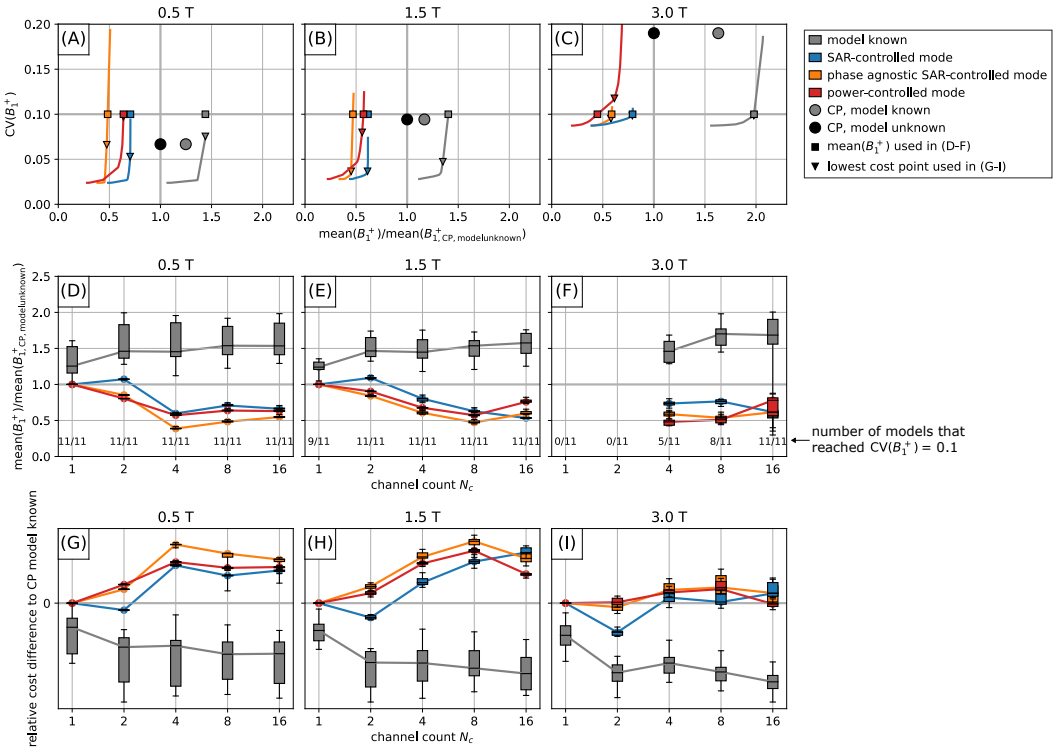

Fig. A.5: $\mathrm{mean}(B_1^+)$ performance for SCM, PASCM and PCM (the limits of all 11 models under test with an additional safety factor are considered each) or with model known (SCM, limits of current model only, no safety factor). $\mathrm{mean}(B_1^+)$ is plotted relative to the $\mathrm{mean}(B_1^+)$ of the CP mode with unknown model condition (combined limits of all 11 models with additional safety factor). (A-C) Trade-off between $\mathrm{mean}(B_1^+)$ and $\mathrm{CV}(B_1^+)$ for model Duke and 8 channels. (D-F) $\mathrm{mean}(B_1^+)$ that reaches $\mathrm{CV}(B_1^+) = 0.1$ divided by the $\mathrm{mean}(B_1^+)$ of the CP mode. Higher values are better. (G-I) Difference of cost $C = -\mathrm{mean}(B_1^+)/\mu\mathrm{T} + 3\times\mathrm{CV}(B_1^+)$ between CP mode and the best shim vector of pTx optimised shim vectors. G-I use different y-scales and are hence not directly comparable.

Bibliography

[1] E. Tiesinga, P. J. Mohr, D. B. Newell, and B. N. Taylor, *The 2018 CODATA Recommended Values of the Fundamental Physical Constants (Web Version 8.1).* Database developed by J. Baker, M. Douma, and S. Kotochigova. National Institute of Standards and Technology, Gaithersburg, MD 20899: https://physics.nist.gov/constants, 2019.

[2] P. C. Lauterbur, 'Image Formation by Induced Local Interactions: Examples Employing Nuclear Magnetic Resonance', *Nature*, vol. 242, no. 5394, pp. 190–191, 5394 1973, ISSN: 1476-4687. DOI: 10.1038/242190a0.

[3] P. D. United Nations Department of Economic and Social Affairs. 'World Population Prospects'. (2023), [Online]. Available: https://population.un.org/wpp/Download/Standard/MostUsed/ (visited on 2022-04-24).

[4] K. Schaap, Y. Christopher-de Vries, P. Slottje, and H. Kromhout, 'Inventory of MRI applications and workers exposed to MRI-related electromagnetic fields in the Netherlands', *European journal of radiology*, vol. 82, 2013. DOI: 10.1016/j.ejrad.2013.07.023.

[5] *Magnetic resonance imaging (MRI) units*, OECD. DOI: 10.1787/1a72e7d1-en.

[6] K. Bazaka and M. V. Jacob, 'Implantable Devices: Issues and Challenges', *Electronics*, vol. 2, no. 1, pp. 1–34, 1 2013, ISSN: 2079-9292. DOI: 10.3390/electronics2010001.

[7] De Zanche, Nicola, van den Berg, Cornelis, Brunner, David, *et al.*, 'ISMRM Best Practices for Safety Testing of Experimental RF Hardware', 2022. DOI: 10.7939/R3-7VPE-X737.

[8] P. Nordbeck, I. Weiss, P. Ehses, *et al.*, 'Measuring RF-induced currents inside implants: Impact of device configuration on MRI safety of cardiac pacemaker leads', *Magnetic Resonance in Medicine*, vol. 61, no. 3, pp. 570–578, 2009, ISSN: 07403194, 15222594. DOI: 10.1002/mrm.21881.

[9] L. Winter, F. Seifert, L. Zilberti, M. Murbach, and B. Ittermann, 'MRI-Related Heating of Implants and Devices: A Review', *Journal of Magnetic Resonance Imaging*, jmri.27194, 2020, ISSN: 1053-1807, 1522-2586. DOI: 10.1002/jmri.27194.

[10] B. Silemek, F. Seifert, J. Petzold, W. Hoffmann, H. Pfeiffer, O. Speck, G. Rose, B. Ittermann, and L. Winter, 'Rapid safety assessment and mitigation of radiofrequency induced implant heating using small root mean square sensors and the sensor matrix Q_s', *Magnetic Resonance in Medicine*, vol. 87, no. 1, pp. 509–527, 2022, ISSN: 0740-3194, 1522-2594. DOI: 10.1002/mrm.28968.

[11] *ISO/TS 10974:2018(E): Assessment of the Safety of Magnetic Resonance Imaging for Patients with an Active Implantable Medical Device*. International Organization for Standardization, 2018.

[12] F. G. Shellock. 'The List'. (2022), [Online]. Available: http://www.mrisafety.com/TMDL_list.php (visited on 2022-08-10).

[13] J. A. Clingan, A. Patel, and D. P. Maher, 'Survey of Spinal Cord Stimulation Hardware Currently Available for the Treatment of Chronic Pain in the United States', *Frontiers in Pain Research*, vol. 1, 2020, ISSN: 2673-561X.

[14] B. Scientific. 'ImageReady™ MRI Full Body Guidelines for Precision™ Montage™ MRI Spinal Cord Stimulator System'. (2021), [Online]. Available: https://www.bostonscientific.com/content/dam/Manuals/us/current-rev-en/91035972-02_RevA_ImageReady_MRI_Full_Body_Guidelines_for_Precision_Montage_MRI_Spinal_Cord_Stimulator_System_MRI_en-US_S.pdf (visited on 2022-11-09).

[15] Medtronic. 'MRI guidelines for Medtronic neurostimulation systems for chronic pain'. (2022), [Online]. Available: https://www.medtronic.com/us-en/healthcare-professionals/products/neurological/spinal-cord-stimulation-systems/intellis-platform.html (visited on 2022-11-09).

[16] Nevro. '1.5 Tesla and 3 Tesla Magnetic Resonance Imaging (MRI) Guidelines'. (2022), [Online]. Available: https://s28.q4cdn.com/260621474/files/doc_downloads/physician_manual/2022/10/10001162-Rev-A-Senza-HFX-iQ-System-1.5T-3T-MRI-Guidelines-(US)_Final.pdf (visited on 2022-11-09).

[17] A. Yong, A. K. Kanodia, M. Wendy, *et al.*, 'Developing patient-centred MRI safety culture: A quality improvement report', *BJR open*, vol. 1, no. 1, p. 20 180 011, 2019, ISSN: 2513-9878. DOI: 10.1259/bjro.20180011. pmid: 33178908.

[18] S. Turner and S. M. Singh, 'Skin burn after magnetic resonance imaging in a patient with an implantable cardioverter-defibrillator', *HeartRhythm Case Reports*, vol. 8, no. 7, pp. 539–540, 2022, ISSN: 2214-0271. DOI: 10.1016/j.hrcr.2022.05.023.

[19] M. Brignole, A. Auricchio, G. Baron-Esquivias, *et al.*, '2013 ESC Guidelines on cardiac pacing and cardiac resynchronization therapy: The Task Force on cardiac pacing and resynchronization therapy of the European Society of Cardiology (ESC). Developed in collaboration with the European Heart Rhythm Association (EHRA)', *European Heart Journal*, vol. 34, no. 29, pp. 2281–2329, 2013, ISSN: 1522-9645. DOI: 10.1093/eurheartj/eht150. pmid: 23801822.

[20] A. W. M. van der Graaf, P. Bhagirath, and M. J. W. Götte, 'MRI and cardiac implantable electronic devices; current status and required safety conditions', *Netherlands Heart Journal: Monthly Journal of the Netherlands Society of Cardiology and the Netherlands Heart Foundation*, vol. 22, no. 6, pp. 269–276, 2014, ISSN: 1568-5888. DOI: 10.1007/s12471-014-0544-x. pmid: 24733688.

[21] P. Nordbeck, G. Ertl, and O. Ritter, 'Magnetic resonance imaging safety in pacemaker and implantable cardioverter defibrillator patients: How far have we come?', *European Heart Journal*, vol. 36, no. 24, pp. 1505–1511, 2015, ISSN: 0195-668X. DOI: 10.1093/eurheartj/ehv086.

[22] D. M. Soto, 'Current guidelines for MRI safety in patients with cardiovascular implantable electronic devices', *Nursing2022*, vol. 50, no. 2, pp. 24–29, 2020, ISSN: 0360-4039. DOI: 10.1097/01.NURSE.0000651612.85237.fc.

[23] S. Shah, C. O'Brien, D. McHugh, H. Elbert, S. Butler, and M. Y. Lopez, 'MR Physicists: Delivering Patient Care', presented at the ISMRM 2022 in London (ISMRM Secret Session on 2022-05-10 in the Resonarium), 2022.

[24] C. Bucciarelli-Ducci and P. Vardas, 'Reconsidering safety and reducing barriers to MRI in patients with cardiac implantable electronic devices', *European Heart Journal*, vol. 43, no. 26, pp. 2479–2481, 2022, ISSN: 0195-668X. DOI: 10.1093/eurheartj/ehab469.

[25] R. Luechinger, V. A. Zeijlemaker, E. M. Pedersen, P. Mortensen, E. Falk, F. Duru, R. Candinas, and P. Boesiger, 'In vivo heating of pacemaker leads during magnetic resonance imaging', *European Heart Journal*, vol. 26, no. 4, 376–383, discussion 325–327, 2005, ISSN: 0195-668X. DOI: 10.1093/eurheartj/ehi009. pmid: 15618060.

[26] B. Silemek, V. Acikel, C. Oto, A. Alipour, Z. G. Aykut, O. Algin, and E. Atalar, 'A temperature sensor implant for active implantable medical devices for in vivo subacute heating tests under MRI', *Magnetic Resonance in Medicine*, vol. 79, no. 5, pp. 2824–2832, 2018, ISSN: 1522-2594. DOI: 10.1002/mrm.26914.

[27] B. Silemek, F. Seifert, J. Petzold, R. Brühl, B. Ittermann, and L. Winter, 'Wirelessly interfacing sensor-equipped implants and MR scanners for improved safety and imaging', *Magnetic Resonance in Medicine*, vol. n/a, no. n/a, 2023, ISSN: 1522-2594. DOI: 10.1002/mrm.29818.

[28] U. Katscher, P. Börnert, C. Leussler, and J. S. van den Brink, 'Transmit SENSE', *Magnetic Resonance in Medicine*, vol. 49, no. 1, pp. 144–150, 2003, ISSN: 07403194. DOI: 10.1002/mrm.10353.

[29] Y. Zhu, 'Parallel excitation with an array of transmit coils', *Magnetic Resonance in Medicine*, vol. 51, no. 4, pp. 775–784, 2004, ISSN: 0740-3194, 1522-2594. DOI: 10.1002/mrm.20011.

[30] J. Vaughan, G. Adriany, C. Snyder, J. Tian, T. Thiel, L. Bolinger, H. Liu, L. DelaBarre, and K. Ugurbil, 'Efficient high-frequency body coil for high-field MRI', *Magnetic Resonance in Medicine*, vol. 52, no. 4, pp. 851–859, 2004, ISSN: 1522-2594. DOI: 10.1002/mrm.20177.

[31] P. Ullmann, S. Junge, M. Wick, F. Seifert, W. Ruhm, and J. Hennig, 'Experimental analysis of parallel excitation using dedicated coil setups and simultaneous RF transmission on multiple channels', *Magnetic Resonance in Medicine*, vol. 54, no. 4, pp. 994–1001, 2005, ISSN: 1522-2594. DOI: 10.1002/mrm.20646.

[32] U. Katscher and P. Börnert, 'Parallel RF transmission in MRI', *NMR in Biomedicine*, vol. 19, no. 3, pp. 393–400, 2006, ISSN: 1099-1492. DOI: 10.1002/nbm.1049.

[33] Y. Eryaman, E. A. Turk, C. Oto, O. Algin, and E. Atalar, 'Reduction of the radio-frequency heating of metallic devices using a dual-drive birdcage coil', *Magnetic Resonance in Medicine*, vol. 69, no. 3, pp. 845–852, 2013, ISSN: 1522-2594. DOI: 10.1002/mrm.24316.

[34] F. Godinez, R. Tomi-Tricot, B. Quesson, M. Barthel, G. Lykowsky, G. Scott, R. Razavi, J. Hajnal, and S. Malik, 'An 8 channel parallel transmit system with current sensor feedback for MRI-guided interventional applications', *Physics in Medicine & Biology*, vol. 66, no. 21, 21NT05, 2021, ISSN: 0031-9155. DOI: 10.1088/1361-6560/ac2fbe.

[35] J. Petzold, S. Schmitter, B. Silemek, L. Winter, O. Speck, B. Ittermann, and F. Seifert, 'Towards an integrated radiofrequency safety concept for implant carriers in MRI based on sensor-equipped implants and parallel transmission', *NMR in Biomedicine*, vol. 36, no. 7, e4900, 2023, ISSN: 0952-3480, 1099-1492. DOI: 10.1002/nbm.4900.

[36] N. Gudino, M. Sonmez, Z. Yao, *et al.*, 'Parallel transmit excitation at 1.5 T based on the minimization of a driving function for device heating', *Medical Physics*, vol. 42, no. 1, pp. 359–371, 2015, ISSN: 2473-4209. DOI: 10.1118/1.4903894.

[37] Y. Eryaman, B. Guerin, C. Akgun, *et al.*, 'Parallel transmit pulse design for patients with deep brain stimulation implants', *Magnetic Resonance in Medicine*, vol. 73, no. 5, pp. 1896–1903, 2015, ISSN: 1522-2594. DOI: 10.1002/mrm.25324.

[38] J. Córcoles, E. Zastrow, and N. Kuster, 'Convex optimization of MRI exposure for mitigation of RF-heating from active medical implants', *Physics in Medicine and Biology*, vol. 60, no. 18, pp. 7293–7308, 2015, ISSN: 0031-9155. DOI: 10.1088/0031–9155/60/18/7293.

[39] M. Etezadi-Amoli, P. Stang, A. Kerr, J. Pauly, and G. Scott, 'Controlling radiofrequency-induced currents in guidewires using parallel transmit: Controlling RF Current Using Parallel Transmit', *Magnetic Resonance in Medicine*, vol. 74, no. 6, pp. 1790–1802, 2015, ISSN: 07403194. DOI: 10.1002/mrm.25543.

[40] C. E. McElcheran, B. Yang, K. J. Anderson, L. Golestanirad, and S. J. Graham, 'Parallel radiofrequency transmission at 3 tesla to improve safety in bilateral implanted wires in a heterogeneous model: pTx at 3T to Improve Safety in Bilateral Implanted Wires', *Magnetic Resonance in Medicine*, vol. 78, no. 6, pp. 2406–2415, 2017, ISSN: 07403194. DOI: 10.1002/mrm.26622.

[41] C. E. McElcheran, L. Golestanirad, M. I. Iacono, P.-S. Wei, B. Yang, K. J. T. Anderson, G. Bonmassar, and S. J. Graham, 'Numerical Simulations of Realistic Lead Trajectories and an Experimental Verification Support the Efficacy of Parallel Radiofrequency Transmission to Reduce Heating of Deep Brain Stimulation Implants during MRI', *Scientific Reports*, vol. 9, no. 1, p. 2124, 2019, ISSN: 2045-2322. DOI: 10.1038/s41598-018-38099-w.

[42] Y. Eryaman, N. Kobayashi, S. Moen, *et al.*, 'A simple geometric analysis method for measuring and mitigating RF induced currents on Deep Brain Stimulation leads by multichannel transmission/reception', *NeuroImage*, vol. 184, pp. 658–668, 2019, ISSN: 10538119. DOI: 10.1016/j.neuroimage.2018.09.072.

[43] B. Guerin, L. M. Angelone, D. Dougherty, and L. L. Wald, 'Parallel transmission to reduce absorbed power around deep brain stimulation devices in MRI: Impact of number and arrangement of transmit channels', *Magnetic Resonance in Medicine*, vol. 83, no. 1, pp. 299–311, 2020, ISSN: 0740-3194, 1522-2594. DOI: 10.1002/mrm.27905.

[44] M. J. Graves, '3 T: The good, the bad and the ugly', *The British Journal of Radiology*, vol. 95, no. 1130, p. 20 210 708, 2022, ISSN: 0007-1285. DOI: 10.1259/bjr.20210708. pmid: 34705565.

[45] *IEC 60601-2-33: Medical Electrical Equipment – Part 2-33: Particular Requirements for the Basic Safety and Essential Performance of Magnetic Resonance Equipment for Medical Diagnosis*. International Electrotechnical Commission, 2022, ISBN: 978-2-8322-3955-1.

[46] Z. Wang, J. C. Lin, W. Mao, W. Liu, M. B. Smith, and C. M. Collins, 'SAR and temperature: Simulations and comparison to regulatory limits for MRI', *Journal of Magnetic Resonance Imaging*, vol. 26, no. 2, pp. 437–441, 2007, ISSN: 1522-2586. DOI: 10.1002/jmri.20977.

[47] M. Murbach, E. Neufeld, W. Kainz, K. P. Pruessmann, and N. Kuster, 'Whole-body and local RF absorption in human models as a function of anatomy and position within 1.5T MR body coil', *Magnetic Resonance in Medicine*, vol. 71, no. 2, pp. 839–845, 2014, ISSN: 1522-2594. DOI: 10.1002/mrm.24690.

[48] M. Murbach, E. Neufeld, E. Cabot, E. Zastrow, J. Córcoles, W. Kainz, and N. Kuster, 'Virtual population-based assessment of the impact of 3 Tesla radiofrequency shimming and thermoregulation on safety and B_1^+ uniformity: Safety and Thermoregulation in 3T RF Shimming', *Magnetic Resonance in Medicine*, vol. 76, no. 3, pp. 986–997, 2016, ISSN: 07403194. DOI: 10.1002/mrm.25986.

[49] M. E. Ladd, P. Bachert, M. Meyerspeer, E. Moser, A. M. Nagel, D. G. Norris, S. Schmitter, O. Speck, S. Straub, and M. Zaiss, 'Pros and cons of ultra-high-field MRI/MRS for human application', *Progress in Nuclear Magnetic Resonance Spectroscopy*, vol. 109, pp. 1–50, 2018, ISSN: 0079-6565. DOI: 10.1016/j.pnmrs.2018.06.001.

[50] C. M. Deniz, 'Parallel Transmission for Ultrahigh Field MRI', *Topics in Magnetic Resonance Imaging*, vol. 28, no. 3, pp. 159–171, 2019, ISSN: 1536-1004. DOI: 10.1097/RMR.0000000000000204.

[51] A. D. Elster. 'Specific Absorption Rate', Questions and Answers in MRI. (2021), [Online]. Available: http://mriquestions.com/what-is-sar.html (visited on 2022-11-30).

[52] E. M. Haacke, L. S. Petropoulos, E. W. Nilges, and D. H. Wu, 'Extraction of conductivity and permittivity using magnetic resonance imaging', *Physics in Medicine and Biology*, vol. 36, no. 6, pp. 723–734, 1991, ISSN: 0031-9155. DOI: 10.1088/0031-9155/36/6/002.

[53] H. Wen, 'Noninvasive quantitative mapping of conductivity and dielectric distributions using RF wave propagation effects in high-field MRI', presented at the Medical Imaging 2003, M. J. Yaffe and L. E. Antonuk, Eds., San Diego, CA, 2003, p. 471. DOI: 10.1117/12.480000.

[54] U. Katscher, T. Voigt, C. Findeklee, P. Vernickel, K. Nehrke, and O. DÖssel, 'Determination of Electric Conductivity and Local SAR Via B1 Mapping', *IEEE Transactions on Medical Imaging*, vol. 28, no. 9, pp. 1365–1374, 2009, ISSN: 1558-254X. DOI: 10.1109/TMI.2009.2015757.

[55] U. Katscher, D.-H. Kim, and J. K. Seo, 'Recent Progress and Future Challenges in MR Electric Properties Tomography', *Computational and Mathematical Methods in Medicine*, vol. 2013, e546562, 2013, ISSN: 1748-670X. DOI: 10.1155/2013/546562.

[56] R. Leijsen, W. Brink, C. van den Berg, A. Webb, and R. Remis, 'Electrical Properties Tomography: A Methodological Review', *Diagnostics*, vol. 11, no. 2, p. 176, 2 2021, ISSN: 2075-4418. DOI: 10.3390/diagnostics11020176.

[57] H. Homann, P. Börnert, H. Eggers, K. Nehrke, O. Dössel, and I. Graesslin, 'Toward individualized SAR models and in vivo validation', *Magnetic Resonance in Medicine*, vol. 66, no. 6, pp. 1767–1776, 2011, ISSN: 1522-2594. DOI: 10.1002/mrm.22948.

[58] Ö. Ipek, A. J. Raaijmakers, J. J. Lagendijk, P. R. Luijten, and C. A. T. van den Berg, 'Intersubject local SAR variation for 7T prostate MR imaging with an eight-channel single-side adapted dipole antenna array', *Magnetic Resonance in Medicine*, vol. 71, no. 4, pp. 1559–1567, 2014, ISSN: 1522-2594. DOI: 10.1002/mrm.24794.

[59] E. F. Meliadò, C. A. T. van den Berg, P. R. Luijten, and A. J. E. Raaijmakers, 'Intersubject specific absorption rate variability analysis through construction of 23 realistic body models for prostate imaging at 7T', *Magnetic Resonance in Medicine*, vol. 81, no. 3, pp. 2106–2119, 2019, ISSN: 1522-2594. DOI: 10.1002/mrm.27518.

[60] W. T. Dixon, 'Simple proton spectroscopic imaging.', *Radiology*, vol. 153, no. 1, pp. 189–194, 1984, ISSN: 0033-8419, 1527-1315. DOI: 10.1148/radiology.153.1.6089263.

[61] J. Ma, 'Dixon techniques for water and fat imaging', *Journal of Magnetic Resonance Imaging*, vol. 28, no. 3, pp. 543–558, 2008, ISSN: 10531807, 15222586. DOI: 10.1002/jmri.21492.

[62] P. A. Hasgall, F. Di Gennaro, E. Neufeld, B. Lloyd, M. C. Gosselin, D. Payne, A. Klingenböck, and N. Kuster, 'IT'IS Database for thermal and electromagnetic parameters of biological tissues', *IT'IS Foundation*, 2018. DOI: 10.13099/VIP21000-04-0.

[63] E. Cabot, T. Lloyd, A. Christ, W. Kainz, M. Douglas, G. Stenzel, S. Wedan, and N. Kuster, 'Evaluation of the RF heating of a generic deep brain stimulator exposed in 1.5 T magnetic resonance scanners', *Bioelectromagnetics*, vol. 34, no. 2, pp. 104–113, 2013, ISSN: 1521-186X. DOI: 10.1002/bem.21745.

[64] B. Guerin, P. Serano, M. I. Iacono, T. M. Herrington, A. S. Widge, D. D. Dougherty, G. Bonmassar, L. M. Angelone, and L. L. Wald, 'Realistic modeling of deep brain stimulation implants for electromagnetic MRI safety studies', *Physics in Medicine & Biology*, vol. 63, no. 9, p. 095 015, 2018, ISSN: 0031-9155. DOI: 10.1088/1361-6560/aabd50.

[65] Y. Huang, J. P. Dmochowski, Y. Su, A. Datta, C. Rorden, and L. C. Parra, 'Automated MRI segmentation for individualized modeling of current flow in the human head', *Journal of Neural Engineering*, vol. 10, no. 6, p. 066 004, 2013, ISSN: 1741-2552. DOI: 10.1088/1741-2560/10/6/066004.

[66] J. D. Nielsen, K. H. Madsen, O. Puonti, H. R. Siebner, C. Bauer, C. G. Madsen, G. B. Saturnino, and A. Thielscher, 'Automatic skull segmentation from MR images for realistic volume conductor models of the head: Assessment of the state-of-the-art', *NeuroImage*, vol. 174, pp. 587–598, 2018, ISSN: 1053-8119. DOI: 10.1016/j.neuroimage.2018.03.001.

[67] W. M. Brink, S. Yousefi, P. Bhatnagar, R. F. Remis, M. Staring, and A. G. Webb, 'Personalized local SAR prediction for parallel transmit neuroimaging at 7T from a single T1-weighted dataset', *Magnetic Resonance in Medicine*, vol. 88, no. 1, pp. 464–475, 2022, ISSN: 1522-2594. DOI: 10.1002/mrm.29215.

[68] E. Meliadò, A. Raaijmakers, A. Sbrizzi, B. Steensma, M. Maspero, M. Savenije, P. Luijten, and C. van den Berg, 'A deep learning method for image-based subject-specific local SAR assessment', *Magnetic Resonance in Medicine*, vol. 83, no. 2, pp. 695–711, 2020, ISSN: 1522-2594. DOI: 10.1002/mrm.27948.

[69] S. Gokyar, F. J. L. Robb, W. Kainz, A. Chaudhari, and S. A. Winkler, 'MRSaiFE: An AI-Based Approach Towards the Real-Time Prediction of Specific Absorption Rate', *IEEE Access*, vol. 9, pp. 140 824–140 834, 2021, ISSN: 2169-3536. DOI: 10.1109/ACCESS.2021.3118290.

[70] S. Gokyar, C. Zhao, S. J. Ma, and D. J. J. Wang, 'Deep learning-based local SAR prediction using B1 maps and structural MRI of the head for parallel transmission at 7 T', *Magnetic Resonance in Medicine*, vol. n/a, no. n/a, ISSN: 1522-2594. DOI: 10.1002/mrm.29797.

[71] N. Schoen, F. Seifert, J. Petzold, G. J. Metzger, O. Speck, B. Ittermann, and S. Schmitter, 'The Impact of Respiratory Motion on Electromagnetic Fields and Specific Absorption Rate in Cardiac Imaging at 7T', *Magnetic Resonance in Medicine*, vol. 88, no. 6, pp. 2645–2661, 2022, ISSN: 0740-3194, 1522-2594. DOI: 10.1002/mrm.29402.

[72] J. Córcoles, E. Zastrow, and N. Kuster, 'On the estimation of the worst-case implant-induced RF-heating in multi-channel MRI', *Physics in Medicine and Biology*, vol. 62, no. 12, pp. 4711–4727, 2017, ISSN: 0031-9155. DOI: 10.1088/1361-6560/aa641b.

[73] T. M. Fiedler, M. E. Ladd, and A. K. Bitz, 'SAR Simulations & Safety', *NeuroImage*, Neuroimaging with Ultra-high Field MRI: Present and Future, vol. 168, pp. 33–58, 2018, ISSN: 1053-8119. DOI: 10.1016/j.neuroimage.2017.03.035.

[74] J. D. Clément, R. Gruetter, and Ö. Ipek, 'A human cerebral and cerebellar 8-channel transceive RF dipole coil array at 7T', *Magnetic Resonance in Medicine*, vol. 81, no. 2, pp. 1447–1458, 2019, ISSN: 1522-2594. DOI: 10.1002/mrm.27476.

[75] A. Destruel, K. O'Brien, J. Jin, F. Liu, M. Barth, and S. Crozier, 'Adaptive SAR mass-averaging framework to improve predictions of local RF heating near a hip implant for parallel transmit at 7 T', *Magnetic Resonance in Medicine*, vol. 81, no. 1, pp. 615–627, 2019, ISSN: 1522-2594. DOI: 10.1002/mrm.27379.

[76] J. Petzold, B. Ittermann, and F. Seifert, 'Robustness of pTx safety concepts to varying subjects and subject positions', in *Proc. Intl. Soc. Mag. Reson. Med. 29*, 2021, p. 2488.

[77] S. J. Malik, J. W. Hand, D. W. Carmichael, and J. V. Hajnal, 'Evaluation of specific absorption rate and heating in children exposed to a 7T MRI head coil', *Magnetic Resonance in Medicine*, vol. 88, no. 3, pp. 1434–1449, 2022, ISSN: 0740-3194, 1522-2594. DOI: 10.1002/mrm.29283.

[78] J. Petzold, B. Ittermann, and F. Seifert, 'On the complexity of pTx systems in SAR assessment', in *Proc. Intl. Soc. Mag. Reson. Med. 30*, 2022, p. 2555.

[79] E. Kopanoglu, C. M. Deniz, M. A. Erturk, and R. G. Wise, 'Specific absorption rate implications of within-scan patient head motion for ultra-high field MRI', *Magnetic Resonance in Medicine*, vol. 84, no. 5, pp. 2724–2738, 2020, ISSN: 1522-2594. DOI: 10.1002/mrm.28276.

[80] G. Eichfelder and M. Gebhardt, 'Local specific absorption rate control for parallel transmission by virtual observation points', *Magnetic Resonance in Medicine*, vol. 66, no. 5, pp. 1468–1476, 2011, ISSN: 07403194. DOI: 10.1002/mrm.22927.

[81] X. G. Xu, 'An exponential growth of computational phantom research in radiation protection, imaging, and radiotherapy: A review of the fifty-year history', *Physics in Medicine and Biology*, vol. 59, no. 18, R233–R302, 2014, ISSN: 0031-9155. DOI: 10.1088/0031-9155/59/18/R233.

[82] Z. Peng, N. Gao, B. Wu, Z. Chen, and X. G. Xu, 'A Review of Computational Phantoms for Quality Assurance in Radiology and Radiotherapy in the Deep-Learning Era', *Journal of Radiation Protection and Research*, vol. 47, no. 3, pp. 111–133, 2022, ISSN: 2508-1888, 2466-2461. DOI: 10.14407/jrpr.2021.00402.

[83] S. N. Makarov, G. M. Noetscher, J. Yanamadala, M. W. Piazza, S. Louie, A. Prokop, A. Nazarian, and A. Nummenmaa, 'Virtual Human Models for Electromagnetic Studies and Their Applications', *IEEE Reviews in Biomedical Engineering*, vol. 10, pp. 95–121, 2017, ISSN: 1937-3333, 1941-1189. DOI: 10.1109/RBME.2017.2722420.

[84] M. J. Ackerman, 'The Visible Human Project: A resource for education', *Academic Medicine*, vol. 74, no. 6, pp. 667–70, 1999, ISSN: 1040-2446.

[85] X. G. Xu, T. C. Chao, and A. Bozkurt, 'VIP-Man: An image-based whole-body adult male model constructed from color photographs of the Visible Human Project for multi-particle Monte Carlo calculations', *Health Physics*, vol. 78, no. 5, pp. 476–486, 2000, ISSN: 0017-9078. DOI: 10.1097/00004032-200005000-00003. pmid: 10772019.

[86] E. Gjonaj, M. Bartsch, M. Clemens, S. Schupp, and T. Weiland, 'High-resolution human anatomy models for advanced electromagnetic field computations', *IEEE Transactions on Magnetics*, vol. 38, no. 2, pp. 357–360, 2002, ISSN: 1941-0069. DOI: 10.1109/20.996096.

[87] W. P. Segars, G. Sturgeon, S. Mendonca, J. Grimes, and B. M. W. Tsui, '4D XCAT phantom for multimodality imaging research: 4D XCAT phantom for multimodality imaging research', *Medical Physics*, vol. 37, no. 9, pp. 4902–4915, 2010, ISSN: 00942405. DOI: 10.1118/1.3480985.

[88] B. J. Klauenberg and D. Miklavcic, *Radio Frequency Radiation Dosimetry and Its Relationship to the Biological Effects of Electromagnetic Fields*. Springer Science & Business Media, 2012, 577 pp., ISBN: 978-94-011-4191-8. Google Books: cjDpCAAAQBAJ.

[89] I. Foundation, 'Eddie cV3.1', in collab. with Z. IT'IS Foundation, 2022. DOI: 10.13099/VIP11018-03-1.

[90] L. Winter, B. Silemek, J. Petzold, H. Pfeiffer, W. Hoffmann, F. Seifert, and B. Ittermann, 'Parallel transmission medical implant safety testbed: Real-time mitigation of RF induced tip heating using time-domain E-field sensors', *Magnetic Resonance in Medicine*, mrm.28379, 2020, ISSN: 0740-3194, 1522-2594. DOI: 10.1002/mrm.28379.

[91] J. Petzold, S. Schmitter, B. Silemek, L. Winter, O. Speck, B. Ittermann, and F. Seifert, 'Investigation of alternative RF power limit control methods for 0.5T, 1.5T, and 3T parallel transmission cardiac imaging: A simulation study', *Magnetic Resonance in Medicine*, 2023. DOI: 10.1002/MRM.29932.

[92] J. Petzold, S. Schmitter, B. Ittermann, and F. Seifert, 'Simulation based comparison of CP mode and 2-spokes pTx excitation to achieve low SAR and high B1+ field strengths and homogeneity in the presence of an elongated 1D implant', in *Proc. Intl. Soc. Mag. Reson. Med. Workshop on MR Safety*, 2019, p. 21.

[93] J. Petzold, S. Schmitter, B. Ittermann, and F. Seifert, 'On the benefit of pTx for implant safety - a multiparameter simulation study', in *Proc. Intl. Soc. Mag. Reson. Med. 28*, 2020, p. 116.

[94] J. Petzold, B. Silemek, L. Winter, B. Ittermann, and F. Seifert, 'Experimental and numerical calibration procedure for RF safety evaluation of implant-embedded sensors', in *Proc. Intl. Soc. Mag. Reson. Med. 31*, 2023, p. 752.

[95] E. L. Hahn, 'Spin Echoes', *Physical Review*, vol. 80, no. 4, pp. 580–594, 1950. DOI: 10.1103/PhysRev.80.580.

[96] D. I. Hoult and R. E. Richards, 'The signal-to-noise ratio of the nuclear magnetic resonance experiment', *Journal of Magnetic Resonance (1969)*, vol. 24, no. 1, pp. 71–85, 1976, ISSN: 0022-2364. DOI: 10.1016/0022-2364(76)90233-X.

[97] V. Bargmann, L. Michel, and V. L. Telegdi, 'Precession of the Polarization of Particles Moving in a Homogeneous Electromagnetic Field', *Physical Review Letters*, vol. 2, no. 10, pp. 435–436, 1959. DOI: 10.1103/PhysRevLett.2.435.

[98] J. C. Maxwell, 'VIII. A dynamical theory of the electromagnetic field', *Philosophical Transactions of the Royal Society of London*, vol. 155, pp. 459–512, 1865. DOI: 10.1098/rstl.1865.0008.

[99] M. F. Dempsey, B. Condon, and D. M. Hadley, 'MRI safety review', *Seminars in Ultrasound, CT and MRI*, vol. 23, no. 5, pp. 392–401, 2002, ISSN: 0887-2171. DOI: 10.1016/S0887-2171(02)90010-7.

[100] C. Gabriel, S. Gabriel, and E. Corthout, 'The dielectric properties of biological tissues: I. Literature survey', *Physics in Medicine and Biology*, vol. 41, no. 11, pp. 2231–2249, 1996, ISSN: 0031-9155, 1361-6560. DOI: 10.1088/0031-9155/41/11/001.

[101] S. Gabriel, R. W. Lau, and C. Gabriel, 'The dielectric properties of biological tissues: II. Measurements in the frequency range 10 Hz to 20 GHz', *Physics in Medicine and Biology*, vol. 41, no. 11, pp. 2251–2269, 1996, ISSN: 0031-9155, 1361-6560. DOI: 10.1088/0031-9155/41/11/002.

[102] C. Malmberg and A. Maryott, 'Dielectric constant of water from 0 to 100 C', *Journal of Research of the National Bureau of Standards*, vol. 56, no. 1, p. 1, 1956, ISSN: 0091-0635. DOI: 10.6028/jres.056.001.

[103] A. J. Fagan, A. K. Bitz, I. M. Björkman-Burtscher, C. M. Collins, V. Kimbrell, A. J. Raaijmakers, and I. S. Committee, '7T MR Safety', *Journal of Magnetic Resonance Imaging*, vol. 53, no. 2, pp. 333–346, 2021, ISSN: 1522-2586. DOI: 10.1002/jmri.27319.

[104] J. P. Hornak, *The Basics of MRI*. Henrietta, NY: Interactive Learning Software, 2020.

[105] P. B. Roemer, W. A. Edelstein, C. E. Hayes, S. P. Souza, and O. M. Mueller, 'The NMR phased array', *Magnetic Resonance in Medicine*, vol. 16, no. 2, pp. 192–225, 1990, ISSN: 0740-3194. DOI: 10.1002/mrm.1910160203. pmid: 2266841.

[106] D. I. Hoult, 'Sensitivity and Power Deposition in a High-Field Imaging Experiment', *Journal of Magnetic Resonance Imaging*, vol. 12, no. 1, pp. 46–67, 2000, ISSN: 1522-2586. DOI: 10.1002/1522-2586(200007)12:1<46::AID-JMRI6>3.0.CO;2-D.

[107] T. S. Ibrahim, R. Lee, B. A. Baertlein, A. Kangarlu, and P.-M. L. Robitaille, 'Application of finite difference time domain method for the design of birdcage RF head coils using multi-port excitations', *Magnetic Resonance Imaging*, vol. 18, no. 6, pp. 733–742, 2000, ISSN: 0730-725X. DOI: 10.1016/S0730-725X(00)00143-0.

[108] G. Adriany, P.-F. Van de Moortele, F. Wiesinger, *et al.*, 'Transmit and receive transmission line arrays for 7 Tesla parallel imaging', *Magnetic Resonance in Medicine*, vol. 53, no. 2, pp. 434–445, 2005, ISSN: 1522-2594. DOI: 10.1002/mrm.20321.

[109] W. A. Willinek, J. Gieseke, G. M. Kukuk, M. Nelles, R. König, N. Morakkabati-Spitz, F. Träber, D. Thomas, C. K. Kuhl, and H. H. Schild, 'Dual-Source Parallel Radiofrequency Excitation Body MR Imaging Compared with Standard MR Imaging at 3.0 T: Initial Clinical Experience', *Radiology*, vol. 256, no. 3, pp. 966–975, 2010, ISSN: 0033-8419. DOI: 10.1148/radiol.10092127.

[110] A. S. Childs, S. J. Malik, D. P. O'Regan, and J. V. Hajnal, 'Impact of number of channels on RF shimming at 3T', *Magnetic Resonance Materials in Physics, Biology and Medicine*, vol. 26, no. 4, pp. 401–410, 2013, ISSN: 1352-8661. DOI: 10.1007/s10334-012-0360-5.

[111] S. Saekho, C.-y. Yip, D. C. Noll, F. E. Boada, and V. A. Stenger, 'Fast-kz three-dimensional tailored radiofrequency pulse for reduced B1 inhomogeneity', *Magnetic Resonance in Medicine*, vol. 55, no. 4, pp. 719–724, 2006, ISSN: 1522-2594. DOI: 10.1002/mrm.20840.

[112] A. C. Zelinski, L. L. Wald, K. Setsompop, V. Alagappan, B. A. Gagoski, V. K. Goyal, and E. Adalsteinsson, 'Fast slice-selective radio-frequency excitation pulses for mitigating B inhomogeneity in the human brain at 7 Tesla', *Magnetic Resonance in Medicine*, vol. 59, no. 6, pp. 1355–1364, 2008, ISSN: 1522-2594. DOI: 10.1002/mrm.21585.

[113] M. A. Cloos, N. Boulant, M. Luong, G. Ferrand, E. Giacomini, D. Le Bihan, and A. Amadon, 'kT-points: Short three-dimensional tailored RF pulses for flip-angle homogenization over an extended volume', *Magnetic Resonance in Medicine*, vol. 67, no. 1, pp. 72–80, 2012, ISSN: 1522-2594. DOI: 10.1002/mrm.22978.

[114] F. Padormo, A. Beqiri, J. V. Hajnal, and S. J. Malik, 'Parallel transmission for ultrahigh-field imaging', *NMR in Biomedicine*, vol. 29, no. 9, pp. 1145–1161, 2016, ISSN: 1099-1492. DOI: 10.1002/nbm.3313.

[115] I. Foundation, 'MRIxViP 3.0T', in collab. with Z. IT'IS Foundation, 2019. DOI: 10.13099/MRIXVIP3.0T-02-0.

[116] I. Foundation, 'MRIxViP 1.5T', in collab. with Z. IT'IS Foundation, 2019. DOI: 10.13099/MRIXVIP1.5T-02-0.

[117] E. Peschke, P. Ulloa, O. Jansen, and J.-B. Hoevener, 'Metallic Implants in MRI – Hazards and Imaging Artifacts', *RöFo - Fortschritte auf dem Gebiet der Röntgenstrahlen und der bildgebenden Verfahren*, vol. 193, no. 11, pp. 1285–1293, 2021, ISSN: 1438-9029, 1438-9010. DOI: 10.1055/a-1460-8566.

[118] L. Mittendorff, A. Young, and J. Sim, 'A narrative review of current and emerging MRI safety issues: What every MRI technologist (radiographer) needs to know', *Journal of Medical Radiation Sciences*, vol. 69, no. 2, pp. 250–260, 2022, ISSN: 2051-3909. DOI: 10.1002/jmrs.546.

[119] J. Spiegel, G. Fuss, M. Backens, W. Reith, T. Magnus, G. Becker, J.-R. Moringlane, and U. Dillmann, 'Transient dystonia following magnetic resonance imaging in a patient with deep brain stimulation electrodes for the treatment of Parkinson disease', *Journal of Neurosurgery*, vol. 99, no. 4, pp. 772–774, 2003, ISSN: 0022-3085. DOI: 10.3171/jns.2003.99.4.0772.

[120] J. M. Henderson, J. Tkach, M. Phillips, K. Baker, F. G. Shellock, and A. R. Rezai, 'Permanent Neurological Deficit Related to Magnetic Resonance Imaging in a Patient with Implanted Deep Brain Stimulation Electrodes for Parkinson's Disease: Case Report', *Neurosurgery*, vol. 57, no. 5, E1063–E1063, 2005, ISSN: 0148-396X, 1524-4040. DOI: 10.1227/01.NEU.0000180810.16964.3E.

[121] L. M. de Vries, W. A. Dijk, C. A. M. Hooijschuur, M. J. G. Leening, B. H. C. Stricker, and N. M. van Hemel, 'Utilisation of cardiac pacemakers over a 20-year period: Results from a nationwide pacemaker registry', *Netherlands Heart Journal*, vol. 25, no. 1, pp. 47–55, 2017, ISSN: 1568-5888. DOI: 10.1007/s12471-016-0880-0. pmid: 27561286.

[122] J. Nyenhuis, S.-M. Park, R. Kamondetdacha, A. Amjad, F. Shellock, and A. Rezai, 'MRI and implanted medical devices: Basic interactions with an emphasis on heating', *IEEE Transactions on Device and Materials Reliability*, vol. 5, no. 3, pp. 467–480, 2005, ISSN: 1558-2574. DOI: 10.1109/TDMR.2005.859033.

[123] R. Luechinger, F. Duru, V. A. Zeijlemaker, M. B. Scheidegger, P. Boesiger, and R. Candinas, 'Pacemaker Reed Switch Behavior in 0.5, 1.5, and 3.0 Tesla Magnetic Resonance Imaging Units: Are Reed Switches Always Closed in Strong Magnetic Fields?', *Pacing and Clinical Electrophysiology*, vol. 25, no. 10, pp. 1419–1423, 2002, ISSN: 1540-8159. DOI: 10.1046/j.1460-9592.2002.01419.x.

[124] *IEC/IEEE 62704-1: Determining the Peak Spatial-Average Specific Absorption Rate (SAR) in the Human Body from Wireless Communications Devices, 30 MHz to 6 GHz – Part 1: General Requirements for Using the Finite-Difference Time-Domain (FDTD) Method for SAR Calculations*. International Electrotechnical Commission, 2017, ISBN: 978-2-8322-4769-3.

[125] F04 Committee, 'Practice for Marking Medical Devices and Other Items for Safety in the Magnetic Resonance Environment', ASTM International. DOI: 10.1520/F2503-20.

[126] *IEC 60601-2-33: Medical Electrical Equipment – Part 2-33: Particular Requirements for the Basic Safety and Essential Performance of Magnetic Resonance Equipment for Medical Diagnosis*. International Electrotechnical Commission, 2015, ISBN: 978-2-8322-2743-5.

[127] G. C. van Rhoon, T. Samaras, P. S. Yarmolenko, M. W. Dewhirst, E. Neufeld, and N. Kuster, 'CEM43°C thermal dose thresholds: A potential guide for magnetic resonance radiofrequency exposure levels?', *European radiology*, vol. 23, no. 8, pp. 2215–2227, 2013, ISSN: 0938-7994. DOI: 10.1007/s00330-013-2825-y. pmid: 23553588.

[128] M. Murbach, E. Zastrow, E. Neufeld, E. Cabot, W. Kainz, and N. Kuster, 'Heating and Safety Concerns of the Radio-Frequency Field in MRI', *Current Radiology Reports*, vol. 3, no. 12, p. 45, 2015, ISSN: 2167-4825. DOI: 10.1007/s40134-015-0128-6.

[129] R. L. McIntosh and V. Anderson, 'SAR versus VAR, and the size and shape that provide the most appropriate RF exposure metric in the range of 0.5-6 GHz', *Bioelectromagnetics*, vol. 32, no. 4, pp. 312–321, 2011, ISSN: 01978462. DOI: 10.1002/bem.20642.

[130] S.-M. Park, R. Kamondetdacha, and J. A. Nyenhuis, 'Calculation of MRI-induced heating of an implanted medical lead wire with an electric field transfer function', *Journal of Magnetic Resonance Imaging*, vol. 26, no. 5, pp. 1278–1285, 2007, ISSN: 1522-2586. DOI: 10.1002/jmri.21159.

[131] F. Bardati, A. Borrani, A. Gerardino, and G. Lovisolo, 'SAR optimization in a phased array radiofrequency hyperthermia system', *IEEE Transactions on Biomedical Engineering*, vol. 42, no. 12, pp. 1201–1207, 1995, ISSN: 00189294. DOI: 10.1109/10.476127.

[132] I. Graesslin, H. Homann, S. Biederer, P. Börnert, K. Nehrke, P. Vernickel, G. Mens, P. Harvey, and U. Katscher, 'A specific absorption rate prediction concept for parallel transmission MR', *Magnetic Resonance in Medicine*, vol. 68, no. 5, pp. 1664–1674, 2012, ISSN: 1522-2594. DOI: 10.1002/mrm.24138.

[133] S. Orzada, T. M. Fiedler, H. H. Quick, and M. E. Ladd, 'Local SAR compression algorithm with improved compression, speed, and flexibility', *Magnetic Resonance in Medicine*, vol. 86, no. 1, pp. 561–568, 2021, ISSN: 0740-3194. DOI: 10.1002/mrm.28739.

[134] B. Guérin, M. Gebhardt, S. Cauley, E. Adalsteinsson, and L. L. Wald, 'Local specific absorption rate (SAR), global SAR, transmitter power, and excitation accuracy trade-offs in low flip-angle parallel transmit pulse design', *Magnetic Resonance in Medicine*, vol. 71, no. 4, pp. 1446–1457, 2014, ISSN: 1522-2594. DOI: 10.1002/mrm.24800.

[135] V. Gras, A. Vignaud, A. Amadon, D. Le Bihan, and N. Boulant, 'Universal pulses: A new concept for calibration-free parallel transmission', *Magnetic Resonance in Medicine*, vol. 77, no. 2, pp. 635–643, 2017, ISSN: 1522-2594. DOI: 10.1002/mrm.26148.

[136] I. Graesslin, P. Vernickel, P. Börnert, K. Nehrke, G. Mens, P. Harvey, and U. Katscher, 'Comprehensive RF safety concept for parallel transmission MR', *Magnetic Resonance in Medicine*, vol. 74, no. 2, pp. 589–598, 2015, ISSN: 1522-2594. DOI: 10.1002/mrm.25425.

[137] F. Seifert, A. Cassara, G. Weidemann, and B. Ittermann, 'Reliable and robust RF safety assessment of transmit array coils at ultrahigh fields', in *Proc. Intl. Soc. Mag. Reson. Med. 22*, 2014, p. 4891.

[138] O. Hölder, 'Ueber einen Mittelwerthssatz', *Nachrichten von der Königl. Gesellschaft der Wissenschaften und der Georg-Augusts-Universität zu Göttingen*, no. 2, pp. 38–47, 1889.

[139] J. A. Nelder and R. Mead, 'A Simplex Method for Function Minimization', *The Computer Journal*, vol. 7, no. 4, pp. 308–313, 1965, ISSN: 0010-4620, 1460-2067. DOI: 10.1093/comjnl/7.4.308.

[140] K. Yee, 'Numerical solution of initial boundary value problems involving maxwell's equations in isotropic media', *IEEE Transactions on Antennas and Propagation*, vol. 14, no. 3, pp. 302–307, 1966, ISSN: 1558-2221. DOI: 10.1109/TAP.1966.1138693.

[141] A. Z. Elsherbeni and V. Demir, *The Finite-Difference Time-Domain: Method for Electromagnetics with MATLAB Simulations* (ACES Series on Computaional Electromagnetics and Engineering), 2nd Edition. Edison, NJ: SciTech Publishing, an imprint of the IET, 2016, 530 pp., ISBN: 978-1-61353-175-4.

[142] J. B. Schneider. 'Understanding the Finite-Difference Time-Domain Method'. (2010), [Online]. Available: https://eecs.wsu.edu/~schneidj/ufdtd/ (visited on 2022-08-08).

[143] C. E. Hayes, W. A. Edelstein, J. F. Schenck, O. M. Mueller, and M. Eash, 'An efficient, highly homogeneous radiofrequency coil for whole-body NMR imaging at 1.5 T', *Journal of Magnetic Resonance (1969)*, vol. 63, no. 3, pp. 622–628, 1985, ISSN: 0022-2364. DOI: 10.1016/0022-2364(85)90257-4.

[144] G. H. Glover, C. E. Hayes, N. J. Pelc, W. A. Edelstein, O. M. Mueller, H. R. Hart, C. J. Hardy, M. O'Donnell, and W. D. Barber, 'Comparison of linear and circular polarization for magnetic resonance imaging', *Journal of Magnetic Resonance (1969)*, vol. 64, no. 2, pp. 255–270, 1985, ISSN: 0022-2364. DOI: 10.1016/0022-2364(85)90349-X.

[145] C. E. Hayes, 'The development of the birdcage resonator: A historical perspective', *NMR in Biomedicine*, vol. 22, no. 9, pp. 908–918, 2009, ISSN: 1099-1492. DOI: 10.1002/nbm.1431.

[146] M.-C. Gosselin, E. Neufeld, H. Moser, *et al.*, 'Development of a new generation of high-resolution anatomical models for medical device evaluation: The Virtual Population 3.0', *Physics in Medicine and Biology*, vol. 59, no. 18, pp. 5287–5303, 2014, ISSN: 0031-9155, 1361-6560. DOI: 10.1088/0031-9155/59/18/5287.

[147] M. Kozlov and R. Turner, 'Fast MRI coil analysis based on 3-D electromagnetic and RF circuit co-simulation', *Journal of Magnetic Resonance*, vol. 200, no. 1, pp. 147–152, 2009, ISSN: 0022-2364. DOI: 10.1016/j.jmr.2009.06.005.

[148] U. Zanovello, F. Seifert, O. Bottauscio, L. Winter, L. Zilberti, and B. Ittermann, 'CoSimPy: An open-source python library for MRI radiofrequency Coil EM/Circuit Cosimulation', *Computer Methods and Programs in Biomedicine*, vol. 216, p. 106 684, 2022, ISSN: 0169-2607. DOI: 10.1016/j.cmpb.2022.106684.

[149] N. S. Mandel, J. L. Ramdial, and E. N. Marcus, 'A second-degree burn after MRI', *Cleveland Clinic Journal of Medicine*, vol. 84, no. 5, pp. 348–349, 2017, ISSN: 0891-1150, 1939-2869. DOI: 10.3949/ccjm.84a.15164.

[150] L. Tagell, A. Alcheikh, R. Jurevics, and A. P. Nair, 'Thigh burn – A magnetic resonance imaging (MRI) related adverse event', *Radiology Case Reports*, vol. 15, no. 12, pp. 2569–2571, 2020, ISSN: 1930-0433. DOI: 10.1016/j.radcr.2020.09.046.

[151] X. Yang, J. Zheng, Y. Wang, S. A. Long, W. Kainz, and J. Chen, 'Body-loop related MRI radiofrequency-induced heating hazards: Observations, characterizations, and recommendations', *Magnetic Resonance in Medicine*, vol. 87, no. 1, pp. 337–348, 2022, ISSN: 1522-2594. DOI: 10.1002/mrm.28954.

[152] J. Lee, M. Gebhardt, L. L. Wald, and E. Adalsteinsson, 'Local SAR in parallel transmission pulse design', *Magnetic Resonance in Medicine*, vol. 67, no. 6, pp. 1566–1578, 2012, ISSN: 1522-2594. DOI: 10.1002/mrm.23140.

[153] S. Orzada, S. Akash, T. M. Fiedler, F. J. Kratzer, and M. E. Ladd, 'An investigation into the dependence of virtual observation point-based specific absorption rate calculation complexity on number of channels', *Magnetic Resonance in Medicine*, vol. 89, no. 1, pp. 469–476, 2023, ISSN: 1522-2594. DOI: 10.1002/mrm.29434.

[154] M. Murbach, E. Neufeld, M. Capstick, W. Kainz, D. O. Brunner, T. Samaras, K. P. Pruessmann, and N. Kuster, 'Thermal Tissue Damage Model Analyzed for Different Whole-Body SAR and Scan Durations for Standard MR Body Coils: Thermal Dose and Tissue Damage in MR RF Heating', *Magnetic Resonance in Medicine*, vol. 71, no. 1, pp. 421–431, 2014, ISSN: 07403194. DOI: 10.1002/mrm.24671.

[155] H. H. Pennes, 'Analysis of Tissue and Arterial Blood Temperatures in the Resting Human Forearm', *Journal of Applied Physiology*, vol. 1, no. 2, pp. 93–122, 1948, ISSN: 8750-7587. DOI: 10.1152/jappl.1948.1.2.93.

[156] E. H. Wissler, 'Pennes' 1948 paper revisited', *Journal of Applied Physiology*, vol. 85, no. 1, pp. 35–41, 1998, ISSN: 8750-7587. DOI: 10.1152/jappl.1998.85.1.35.

[157] A. Z. Dakroury, M. B. S. Osman, and A. W. A. El-Sharkawy, 'Thermal properties of aqueous solutions of polyvinylpyrrolidone in the temperature range 20–80°C', *International Journal of Thermophysics*, vol. 11, no. 3, pp. 515–523, 1990, ISSN: 1572-9567. DOI: 10.1007/BF00500843.

[158] S. Wolf, D. Diehl, M. Gebhardt, J. Mallow, and O. Speck, 'SAR simulations for high-field MRI: How much detail, effort, and accuracy is needed?', *Magnetic Resonance in Medicine*, vol. 69, no. 4, pp. 1157–1168, 2013, ISSN: 1522-2594. DOI: 10.1002/mrm.24329.

[159] E. Kopanoglu, 'Actual patient position versus safety models: Specific Absorption Rate implications of initial head position for Ultrahigh Field Magnetic Resonance Imaging', *NMR in Biomedicine*, vol. 36, no. 5, e4876, 2023, ISSN: 0952-3480, 1099-1492. DOI: 10.1002/nbm.4876.

[160] M. de Greef, O. Ipek, A. J. E. Raaijmakers, J. Crezee, and C. A. T. van den Berg, 'Specific absorption rate intersubject variability in 7T parallel transmit MRI of the head', *Magnetic Resonance in Medicine*, vol. 69, no. 5, pp. 1476–1485, 2013, ISSN: 1522-2594. DOI: 10.1002/mrm.24378.

[161] M. Le Garrec, V. Gras, M.-F. Hang, G. Ferrand, M. Luong, and N. Boulant, 'Probabilistic analysis of the specific absorption rate intersubject variability safety factor in parallel transmission MRI', *Magnetic Resonance in Medicine*, vol. 78, no. 3, pp. 1217–1223, 2017, ISSN: 1522-2594. DOI: 10.1002/mrm.26468.

[162] S. J. Malik, J. W. Hand, R. Satnarine, A. N. Price, and J. V. Hajnal, 'Specific absorption rate and temperature in neonate models resulting from exposure to a 7T head coil', *Magnetic Resonance in Medicine*, vol. 86, no. 3, pp. 1299–1313, 2021, ISSN: 1522-2594. DOI: 10.1002/mrm.28784.

[163] O. Kraff and H. H. Quick, 'Radiofrequency Coils for 7 Tesla MRI', *Topics in Magnetic Resonance Imaging*, vol. 28, no. 3, pp. 145–158, 2019, ISSN: 0899-3459. DOI: 10.1097/RMR.0000000000000206.

[164] S. N. Williams, P. McElhinney, and S. Gunamony, 'Ultra-high field MRI: Parallel-transmit arrays and RF pulse design', *Physics in Medicine & Biology*, vol. 68, no. 2, 02TR02, 2023, ISSN: 0031-9155. DOI: 10.1088/1361-6560/aca4b7.

[165] T. M. Fiedler, S. Orzada, M. Flöser, S. H. G. Rietsch, H. H. Quick, M. E. Ladd, and A. K. Bitz, 'Performance analysis of integrated RF microstrip transmit antenna arrays with high channel count for body imaging at 7 T', *NMR in Biomedicine*, vol. 34, no. 7, e4515, 2021, ISSN: 1099-1492. DOI: 10.1002/nbm.4515.

[166] D. Hudson and A. P. Jones, 'A 3-year review of MRI safety incidents within a UK independent sector provider of diagnostic services', *BJR Open*, vol. 1, no. 1, p. 20180006, 2019, ISSN: 2513-9878. DOI: 10.1259/bjro.20180006. pmid: 33178906.

[167] S. A. Sapareto and W. C. Dewey, 'Thermal dose determination in cancer therapy', *International Journal of Radiation Oncology*Biology*Physics*, vol. 10, no. 6, pp. 787–800, 1984, ISSN: 03603016. DOI: 10.1016/0360-3016(84)90379-1.

[168] P. S. Yarmolenko, E. J. Moon, C. Landon, A. Manzoor, D. W. Hochman, B. L. Viglianti, and M. W. Dewhirst, 'Thresholds for thermal damage to normal tissues: An update', *International Journal of Hyperthermia*, vol. 27, no. 4, pp. 320–343, 2011, ISSN: 0265-6736, 1464-5157. DOI: 10.3109/02656736.2010.534527.

[169] N. Boulant, X. Wu, G. Adriany, S. Schmitter, K. Uğurbil, and P.-F. V. de Moortele, 'Direct control of the temperature rise in parallel transmission by means of temperature virtual observation points: Simulations at 10.5 tesla', *Magnetic Resonance in Medicine*, vol. 75, no. 1, pp. 249–256, 2016, ISSN: 1522-2594. DOI: 10.1002/mrm.25637.

[170] Abbott. 'MRI Procedure Information, Abbott Medical MR Conditional SCS and DRG Systems, Clinician's Manual'. (2022), [Online]. Available: https://manuals.sjm.com/Search-Form?re=North-America&cc=US&ln=EN&ct=professional&qry=3771&ipp=10 (visited on 2022-11-09).

[171] J. A. Martinez, P. Serano, and D. B. Ennis, 'Patient Orientation Affects Lead-Tip Heating of Cardiac Active Implantable Medical Devices during MRI', *Radiology: Cardiothoracic Imaging*, vol. 1, no. 3, e190006, 2019, ISSN: 2638-6135. DOI: 10.1148/ryct.2019190006. pmid: 32076667.

[172] P. Verrills, C. Sinclair, and A. Barnard, 'A review of spinal cord stimulation systems for chronic pain', *Journal of Pain Research*, vol. 9, pp. 481–492, 2016, ISSN: null. DOI: 10.2147/JPR.S108884. pmid: 27445503.

[173] A. C. Özen, B. Silemek, T. Lottner, E. Atalar, and M. Bock, 'MR safety watchdog for active catheters: Wireless impedance control with real-time feedback', *Magnetic Resonance in Medicine*, vol. 84, no. 2, pp. 1048–1060, 2020, ISSN: 1522-2594. DOI: 10.1002/mrm.28153.

[174] J. N. Teixeira, F. Godinez, S. Malik, and J. V. Hajnal, 'Planning Current Nulling for Worst Case SAR reduction in a Cardiac Guidewire Scenario at 1.5T', in *Proc. Intl. Soc. Mag. Reson. Med. 27*, 2019, p. 4179.

[175] A. E. Campbell-Washburn, R. Ramasawmy, M. C. Restivo, *et al.*, 'Opportunities in Interventional and Diagnostic Imaging by Using High-Performance Low-Field-Strength MRI', *Radiology*, vol. 293, no. 2, pp. 384–393, 2019, ISSN: 0033-8419. DOI: 10.1148/radiol.2019190452.

[176] J. P. Marques, F. F. Simonis, and A. G. Webb, 'Low-field MRI: An MR physics perspective', *Journal of Magnetic Resonance Imaging*, vol. 49, no. 6, pp. 1528–1542, 2019, ISSN: 1522-2586. DOI: 10.1002/jmri.26637.

[177] K. H. Taber and L. A. Hayman, 'Temperature monitoring during MR imaging: Comparison of fluoroptic and standard thermistors', *Journal of Magnetic Resonance Imaging*, vol. 2, no. 1, pp. 99–101, 1992, ISSN: 1522-2586. DOI: 10.1002/jmri.1880020119.

[178] H. G. Mond, J. R. Helland, and A. Fischer, 'The Evolution of the Cardiac Implantable Electronic Device Connector', *Pacing and Clinical Electrophysiology*, vol. 36, no. 11, pp. 1434–1446, 2013, ISSN: 1540-8159. DOI: 10.1111/pace.12211.

[179] S. Nisam and S. Reddy, 'The story of ... a lead', *EP Europace*, vol. 17, no. 5, pp. 677–688, 2015, ISSN: 1099-5129. DOI: 10.1093/europace/euu391.

[180] F. Seifert, H. Pfeiffer, R. Mekle, P. Waxmann, and B. Ittermann, '7T 8-channel pTx head coil with high B1+ efficiency optimized for MRS', in *Proc. Intl. Soc. Mag. Reson. Med. 24*, 2016, p. 3545.

List of Figures

List of Tables